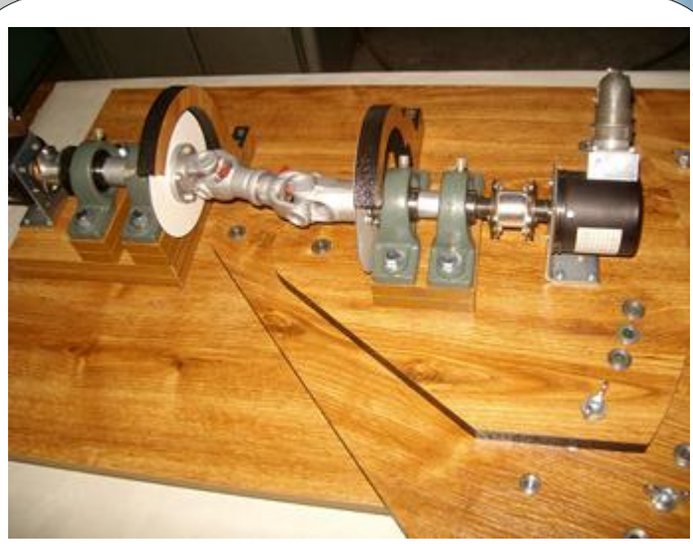
International journal
for science, technics and
innovations for the industry

MACHINES TECHNOLOGIES MATERIALS

YEAR X Issue 7 / 2016 ISSN 1313-0226



Published by
Scientific technical
Union of Mechanical Engineering

MACHINES. TECHNOLOGIES. MATERIALS

INTERNATIONAL SCIENTIFIC JOURNAL

PUBLISHER

SCIENTIFIC TECHNICAL UNION OF MECHANICAL ENGINEERING

108, Rakovski Str., 1000 Sofia, Bulgaria
tel. (+359 2) 987 72 90,
tel./fax (+359 2) 986 22 40,
office@stumejournals.com
www.stumejournals.com

ISSN 1313-0226, YEAR X, ISSUE 7 / 2016

EDITOR-IN-CHIEF

Prof. D.Sc. DHC Georgi Popov,
President of Bulgarian Scientific and Technical Union of Mechanical Engineering

EDITORIAL BOARD

MEMBERS	SCIENTIFIC COMPETENCE
Prof. Dimitar Damyanov	Automatisation of production
Prof. Dimitar Karaivanov	Mechanics of machines
Prof. Dimitar Stavrev	Technologies and materials
Prof. Dimitar Yonchev	National and industrial security
Prof. Galina Nikolcheva	Machines tools and technologies
Prof. Hristo Shehtov	Automatisation of production
Prof. Idilija Bachkova	Automatisation of production
Prof. Ivan Kralov	Mechanics of machines
Prof. Ivan Parshorov	Technologies and materials
Prof. Ivan Yanchev	Machines and technologies
Prof. Ivo Malakov	Automatisation of production
Prof. Kiril Angelov	Industrial Management
Prof. Lilo Kunchev	Transport Equipment and Technology
Prof. Lubomir Dimitrov	Machines and technologies
Prof. Miho Mihov	Agricultural machinery
Prof. Miroslav Denchev	Ergonomics and design
Prof. Mladen Velev	Economics and Marketing
Prof. Nikolay Diulgerov	Technologies and materials
Prof. Ognyan Andreev	Production management
Prof. Petar Kolev	Transport Equipment and Technology
Prof. Roman Zahariev	Robotics
Prof. Sasho Guergov	Robotic systems and technology
Prof. Tsanka Dikova	Technologies and materials
Prof. Vitan Galabov	Mechanics of machines

MACHINES. TECHNOLOGIES. MATERIALS

INTERNATIONAL SCIENTIFIC JOURNAL

ISSN 1313-0226, YEAR X, ISSUE 7 / 2016

EDITORIAL BOARD FOREIGN MEMBERS

Prof. Adel Mahmoud	IQ	Prof. Marian Tolnay	SK
Prof. Ahmet Ertas	TR	Prof. Mark Easton	AU
Prof. Andonaq Londo	AL	Prof. Mart Tamre	EE
Prof. Andrei Firsov	RU	Prof. Maryam Ehteshamzade	IR
Prof. Andrzej Golabczak	PL	Prof. Michael Evan Goodsite	DK
Prof. Anita Jansone	LV	Prof. Movlazade Vagif Zahid	AZ
Prof. Aude Billard	CH	Prof. Natasa Naprstkova	CZ
Prof. Bojan Dolšak	SI	Prof. Oana Dodun	RO
Prof. Christian Marxt	LI	Prof. Oleg Sharkov	RU
Prof. Dale Carnegie	NZ	Prof. Páll Jensson	IS
Prof. Ernest Nazarian	AM	Prof. Patrick Anderson	NL
Prof. Esam Husein	KW	Prof. Paul Heuschling	LU
Prof. Ewa Gunnarsson	SW	Prof. Pavel Kovac	RS
Prof. Filipe Samuel Silva	PT	Prof. Per Skjerpe	NO
Prof. Francisco Martinez Perez	CU	Prof. Péter Korondi	HU
Prof. Franz Haas	AT	Prof. Peter Kostal	SK
Prof. Genadii Bagliuk	UA	Prof. Juan Alberto Montano	MX
Prof. Georg Frey	DE	Prof. Renato Goulart	BR
Prof. Gregory Gurevich	IL	Prof. Roumen Petrov	BE
Prof. Haydar Odinaev	TJ	Prof. Rubén Darío Vásquez Salazar	CO
Prof. Hi□oyuki Moriyama	JP	Prof. Safet Isić	BA
Prof. Iryna Charniak	BY	Prof. Sean Leen	IE
Prof. Ivan Svarc	CZ	Prof. ShI Xiaowei	CN
Prof. Ivica Veza	HR	Prof. Shoirdzan Karimov	□Z
Prof. Jae-Young Kim	KR	Prof. Sreten Savićević	ME
Prof. Jerzy Jedzejewski	PL	Prof. Stefan Dimov	UK
Prof. Jean-Emmanuel Broquin	FR	Prof. Svetlana Gubenko	UA
Prof. Jordi Romeu Garbi	ES	Prof. Sveto Cvetkovski	MK
Prof. Jukka Tuhkuri	FI	Prof. Tamaz Megre□idze	GE
Prof. Kazimieras Juzėnas	LT	Prof. Tashtanbay Sartov	KG
Prof. Krasimir Marchev	USA	Prof. Teimuraz Kochadze	GE
Prof. Krzysztof Rokosz	PL	Prof. Thorsten Schmidt	DE
Prof. Leon Kukielka	PL	Prof. Tonci Mikac	HR
Prof. Mahmoud El Gammal	EG	Prof. Vasile Cartofeanu	MD
Prof. Manolakos Dimitrios	GR	Prof. Yasar Pancar	TR
Prof. Marat Ibatov	KZ	Prof. Yurij Kuznetsov	UA
Prof. Marco Bocciolone	IT	Prof. Wei Hua Ho	ZA

C O N T E N T S

ESTIMATION OF LOAD CAPACITY OF ADHESIVE JOINTS FOR TRANSPORT ENGINEERING
Prof., Dr.Sc.(Eng.) Koryagin S.I., Assoc. Prof., Dr.Sc.(Eng.) Sharkov O.V., Assoc. Prof., Dr.(Eng.) Buylov S.V., Prof., Dr.Sc.(Eng.) Velikanov N.L., graduate Kulakov A.S. 3

DATABASE DESIGN AT SYNTHESIS OF ELECTROMECHANICAL MODULES
Assoc. Prof. Dahterova D., M. Eng. Nikolova I. 7

METHODOLOGY OF CARRYING RESEARCHES OF KINEMATIC PAIR OF PIVIOTING FRICTION
Ph.D. Eng. Wozniak M., Ph.D. Eng.Kubiak P., M.Sc. Eng. Jozwiak P., Eng. Madziara S., Eng. Najbert S., Prof. M.Sc. Ozuna G., Ph.D. Eng. Chunbao L. 11

OPTIMIZATION OF GEOMETRIC PARAMETERS OF HARD METAL MICRO DRILS TO INCREASE TOOL LIFE AND PERFORMANCE OF DRILLING PACKAGE OF PRINTED CIRCUIT BOARDS
Doctor of science, Prof., Turmanidze R., Senior laboratory Bachanadze V., Undergraduate student Popkhadze G. 14

EXAMINATION OF ACOUSTIC PROPERTIES OF A GEAR PUMP AFTER TOOTH ROOT UNDERCUTTING USING THE INDUCTION OF DECISION TREES
PhD. , M.Sc. Deptuła A. 19

ON A PHYSICO-MATHEMATICAL MODEL FOR CONTROLLED FORMATION OF PERIODIC NANOSTRUCTURES AT SOLID SURFACES IRRADIATED BY FEMTOSECOND LASER PULSES
Prof. Dr.Sc.Math. Guseynov Sh.E., B.Sc.Phys. Žaimis U. 23

ALTERNATIVE FUELS FOR DIESEL ENGINES AND THEIR IMPACT ON ENGINE EMISSIONS. A LITERATURE REVIEW
Zbarcea O. PhD student, Prof. Scarpete D. 27

DEVELOPMENT OF GEOMETRY OF CARVIDE MULTIFACE PLATES FOR SUPERFINISH PROCESSING
Rechenko D., Popov A., Titov Yu., Gritsenko B. 33

SYNCHRONIZATION T-CHAOTIC SYSTEM
Assist.Prof. Sahab A.R. PhD., M.Sc. Abazari M. 37

DEVELOPMENT, MANUFACTURING AND INTRODUCTION OF NEW CONSTRUCTIVE SOLUTION OF TRANSMISSION MECHANISM
Conf. dr. eng., Prof. Abdullayev A., Conf. dr. eng., Prof. Najafov A., dr.eng, Ahmedov B., dr.eng Gasimov R., dr.eng. Mirzoyev H. 42

INCREASING THE RESISTANCE OF PRECISION INSTRUMENT-MAKING ELEMENTS FROM OPTICAL GLASS TO EXTERNAL THERMO-INFLUENCES BY PRELIMINARY ELECTRON-BEAM PROCESSING OF SURFACES
Associate Professor Ph.D. Yatsenko I., Professor dr. eng.Antonyuk V., senior researcher dr. eng. Kyrychenko O., Professor dr. eng. Vashchenko V., senior lecturer Tsybulin V. 44

ON EXPERIENCE OF MODELING OF HYDRODYNAMIC PROBLEM USING COMBINED NEURAL NETWORK AND DYNAMIC MODEL
C.Sc. Doc. Yasinskiy I. 48

ENERGY TECHNOLOGY ACTIVATION COMPONENTS FUNCTIONAL MATERIALS BASED ON POLYMERIC MATRIX
Sarokin V., Doc. cand. eng. Auchynnikau Y., Doc. cand. eng. Avdeychik S., Prof. dr. eng. Struk V. 51

ESTIMATION OF LOAD CAPACITY OF ADHESIVE JOINTS FOR TRANSPORT ENGINEERING

ОЦЕНКА НАГРУЗОЧНОЙ СПОСОБНОСТИ КЛЕЕВЫХ СОЕДИНЕНИЙ ДЛЯ ТРАНСПОРТНОГО МАШИНОСТРОЕНИЯ

Prof., Dr.Sc.(Eng.) Koryagin S.I., Assoc. Prof., Dr.Sc.(Eng.) Sharkov O.V., Assoc. Prof., Dr.(Eng.) Buylov S.V.,
Prof., Dr.Sc.(Eng.) Velikanov N.L., graduate Kulakov A.S.
Immanuel Kant Baltic Federal University – Russia, Kaliningrad

skoryagin@kantiana.ru, osharkov@kantiana.ru,

Abstract: *Adhesive joints are widely applied in transport engineering. Crack resistance is an important parameter determining the load capacity and durability of adhesive joints. The calculation-experimental method, which allows to raise the accuracy and reliability of an estimation of the crack resistance of the adhesive compositions is proposed. The proposed method can be implemented using a test station that ensures the loading of double cantilever glued beams by equal and oppositely directed moments. The mathematical model for determining the value of crack advancing energy, includes only one independent parameter (the bending moment) was obtained. It is established that change of geometrical parameters of the proposed experimental models slightly effects (less than 3.5 %) on value of crack advancing energy.*

Keywords: ADHESIVE JOINT, LOAD CAPACITY, TRANSPORT ENGINEERING, ADHESIVE JOINT, CRACK RESISTANCE, CRACK ADVANCING ENERGY, ADHESIVE COMPOSITION

1. Введение

В настоящее время клеевые соединения находят широкое применение в транспортном машиностроении для снижения массо-габаритных характеристик, увеличения нагрузочной способности, герметизации, восстановления работоспособности, а также гашение шума и вибрации [1–14].

Проведенные рядом компаний исследования подтверждают, что применение клеевых соединений позволяет в 2.0…2.5 раза снизить трудоемкость сборки и уменьшить материалоемкость конструкций до 10% по сравнению с клепкой и сваркой [11].

Например склеивание секций металлических кузовов еще не нашло широкого применения, тогда как пластмассовые кузова машин многих марок соединяют склеиванием. В связи этим разработка новых клеевых композиций с улучшенными эксплуатационными свойствами представляет определенный практический интерес [12]. Как правило, основным показателем, характеризующим, пригодность клеевого соединения при эксплуатации является его нагрузочная способность.

Нагрузочная способность конструкционных клеевых соединений определяется не столько собственной прочностью клеевых композиций, сколько возникающей в них концентрацией напряжений, за счет образования в процессе склеивания технологических дефектов: пустот; инородных включений; областей с отсутствием или слабой адгезионной связью.

При этом в клеевой слое (шве) наблюдается неоднородное напряженное состояние, образующееся в следствии различия прочностных характеристик клеевых композиций и соединяемых материалов. Окружающая среда дополнительно оказывает неравномерное разупрочняющее действие на клеевой слой.

Одной из важнейших характеристик, определяющих нагрузочную способность клеевых соединений, является их трещиностойкость.

Несмотря на многочисленные теоретические и экспериментальные результаты исследований критериев оценки трещиностийкости клеевых соединений, это вопрос остается не полностью исследованным [3, 15–27].

Так многие полученные результаты являются несравнимыми, а некоторые недостоверными из-за некорректного планирования экспериментов, так как могут включать в себя величины, которые не обязательно являются независимыми. В результате этого величина, характеризующая работу, затрачиваемую на деформирование собственно склеиваемых деталей, может являться преобладающей.

Для оценки трещиностойкости клеевых соединений можно использовать несколько критериев: коэффициент интенсивности напряжений; коэффициент раскрытия трещины или удельную энергию продвижения трещины [28–31].

Оценка трещиностойкости с использованием коэффициентов интенсивности напряжений и раскрытия трещины требует теоретического и экспериментального анализа сложного напряженного состояния тонкого слоя клея, что представляет собой достаточно сложную задачу.

Поэтому при, оценке трещиностойкости клеевых соединений обычно используют энергетический критерий – удельную энергию продвижения трещины (силу продвижения трещины).

Для повышения точности и достоверности определения удельной энергии продвижения трещины авторами разработана расчетно-экспериментальная методика.

К настоящему времени разработано значительное число методических рекомендаций и стандартов по оценке нагрузочной способности клеевых соединений при различных видах приложения нагружающих усилий, которые, с определенными допущениями, могут быть применены и для оценки их трещиностойкости [28-35].

В качестве базовой выбрана известная методика испытания клеевого соединения на трещиностойкость, заключающаяся в том, что к двухконсольному образцу прикладывают изгибающую нагрузку в виде усилий, действующих перпендикулярно консольным балкам. При этом регистрируют изменение нагрузки и соответствующее ей изменение длины образующейся в клеевом слое соединения трещины. Затем определяют удельную энергию продвижения трещины и по ней судят о нагрузочной способности [28].

При такой поставке эксперимента наблюдается существенное влияние длины растущей трещины на стабильность результатов испытаний, которое приводит к недостаточной точности полученных данных.

2. Математическая модель

Получим математическую модель, описывающую параметры трещиностойкости клеевого соединения.

Известна зависимость для определения удельной энергии продвижения трещины [30, 31]

$$G = \frac{M^2}{2b}\frac{dC}{da}, \qquad (1)$$

где M – изгибающий момент; C – податливость заделки консольных балок; b – ширина консольных балок (клеевого соединения); a – длина трещины.

В предложенной расчетной схеме (рис. 1) при нагружении изгибающими моментами экспериментальный образец накапливает потенциальную энергию, которую можно определить по зависимости

$$U = \frac{1}{2} M^2 \left[\frac{a}{2E_1 J_1} + \frac{\alpha_1}{2} + \frac{k^2 a}{2E_2 J_2} + \frac{\alpha_2}{2} + \frac{(l-k)^2 (l-a)}{2(EJ)_0} \right], \quad (2)$$

где k – коэффициент, зависящий от характеристик материала и размеров консольных балок; l – длина консольных балок; E_1, E_2 – модули упругости материала консольных балок; J_1, J_2 – моменты инерции поперечных сечений консольных балок; α_1, α_2 – коэффициенты податливости заделки консольных балок; $(EJ)_0$ – изгибная жесткость единицы длины экспериментального образца.

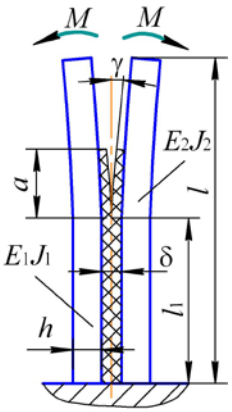


Рис. 1. Расчетная схема оценки трещиностойкости

Решая совместно зависимости (1) и (2) получим выражение для определения величины энергии продвижения трещины в виде

$$G_I = \frac{M^2}{2b} \left[\frac{1}{E_1 J_1} + \frac{k^2}{E_2 J_2} - \frac{(1-k)^2}{(EJ)_0} \right]. \quad (3)$$

Выражение (3) получено в предположении постоянства коэффициентов податливости $\alpha_1 = \alpha_2 = const$.

Для определения условий, при которых это предположение выполняется, произведены расчеты напряженно-деформированного состояния экспериментальных образцов. Полученные результаты [36, 37] показали, что напряжения, возникающие в материале балок и в клеевой композиции на расстоянии четырех толщин консоли $4h$, уменьшаются до ничтожно малых величин.

Следовательно, длина участка, в пределах которого напряженное состояния, соответствующее изгибу отдельных балок, переходит к напряженному состоянию изгиба неразрушенной части образца не превышает четырех высот консольной балки $l_1 = 4h$.

Таким образом, если в процессе испытания часть образца длиной более четырех высот балки не разрушена, то характер распределения напряжений не изменится, что обеспечит постоянство коэффициентов податливости.

Существенное достоинство выражения (3) его простота, так как оно позволяет оценивать трещиностойкость с использованием только одного независимого параметра – изгибающего момента (M), который определяется экспериментально.

3. Экспериментальная методика

Сущность предлагаемой методики заключается в следующем. Экспериментальный образец (рис. 2) выполняют в виде двух консольно закрепленных балок 1 и 2, соединенных клеевой композицией 3.

Силы F, создающие изгибающий момент на каждой балке, прикладывают с помощью специальных нагружающих устройств 4 и 5, состоящих из блоков и гибких нитей. Концы каждой из нитей соединены с обеими консольными балками, вследствие чего нагрузка к балкам передается в виде равных и противоположно направленных моментов M (рис. 1). Нагружение экспериментальных образцов вызывает разрушение клеевого соединения, сопровождающееся образованием и ростом трещины в его плоскости.

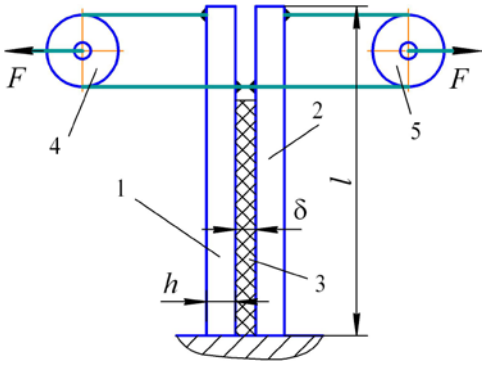


Рис. 2. Схема испытательной установки

Повышение точности в этом случае достигается за счет создания идентичных условий трещинообразования при наружении.

4. Экспериментальные результаты

Расчетно-экспериментальная оценка характеристик трещиностойкости клеевого соединения по предлагаемой методике проводили с использованием специально разработанной экспериментальной установки (рис. 2).

В исследованиях использовали клеевые композиции нескольких типов: ВАК-А; Спрут Плюс и Спрут-5М, прочностные характеристики которых приведены в табл.1.

Таблица 1: *Основные технологические характеристики клеевых композиций*

Физико–химические свойства	Клеевая композиция		
	ВАК-А	Спрут–Плюс	Спрут–5М
Условная вязкость по ВЗ-246 [сек]	70…80	30…60	20…35
Температура эксплуатации [ºС]	-40…+80	-60…+100	-10…+60
Прочность на воздухе [28] при:	-	-	-
равномерном отрыве [МПа]	10.8	8.5	8.4
сдвиге [МПа]	10.1	9.3	7.0
Прочность в воде [28] при:	-	-	-
равномерном отрыве [МПа]	7.7	5.1	4.6
сдвиге [МПа]	7.2	5.6	4.1
Прочность в нефтепродуктах [28] при:	-	-	-
равномерном отрыве [МПа]	8.6	7.8	6.3
сдвиге [МПа]	8.2	8.6	5.2

При поведении испытаний использовали балки прямоугольного сечения $b \times h$ изготовленные из стали Ст.3. Нагружение экспериментального образца выполняли при постоянной скорости перемещения нагружающих устройств.

Изгибающие моменты M и величины углов раскрытия трещины γ измеряли с помощью тензодатчиков типа 2ПКБ-10-100×В. Для регистрации сигнала тензодатчиков применяли регистрирующую аппаратуру – двухкоординатный графопостроитель Н306.

При определении характеристик трещиностойкости клеевых соединений обычно учитывают два переходных состояния.

Первое состояние (характеризуется величиной G_{Ic}) соответствует случаю, когда трещина делает резкий скачок. В предлагаемой методике оно наблюдается при величине максимального изгибного момента.

Второе состояние (характеризуется величиной G_{Ia}) соответствует случаю остановки развития трещины. Данная величина определялась по величине изгибного момента при остановке развития трещины.

Величины G_{Ic} и G_{Ia} рассчитывали по формуле (3) для соединений на основе клеевых композиций ВАК-А, Спрут Плюс и Спрут-5М.

Как показывает анализ средних значений G_{Ic} и G_{Ia} (табл. 2) наибольшая величина трещиностойкости наблюдалась для клеевой композиции ВАК-А. Поэтому дальнейшие расчеты по определению характера зависимости $G_{Ic}, G_{Ia} = f(b, h, \delta)$ проводили только для клеевой композиции ВАК-А.

Таблица 2: *Зависимость энергии продвижения трещины от типа клеевой композиции*

Параметры	Клеевая композиция		
	ВАК-А	Спрут–Плюс	Спрут–5М
Энергия продвижения трещины G_{Ic} [Дж/м^2]	573	465	274
Относительная величина энергии продвижения трещины G_{Ic} [%]	100	81.1	47.8
Энергия продвижения трещины G_{Ia} [Дж/м^2]	512	414	238
Относительная величина энергии продвижения трещины G_{Ia} [%]	100	80.1	46.5

Как видно из рис. 3 при диапазоне изменении ширины балки b в 2 раза (с 10 до 20 мм), а её высоты h в 3 раза (с 4 до 12 мм), наибольшее изменение величины G_{Ic} соответственно составляет всего 0,37 % и 0,65 %.

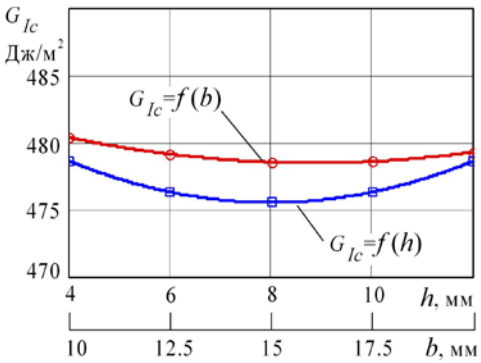


Рис. 3. Зависимость энергии продвижения трещины от размеров консольной балки в момент образования трещины

Как видно из рис. 4 при диапазоне изменении ширины балки b в 2 раза (с 10 до 20 мм), а её высоты h в 3 раза (с 4 до 12 мм), наибольшее изменение величины G_{Ia} соответственно составляет всего 0,84 и 1,24 %.

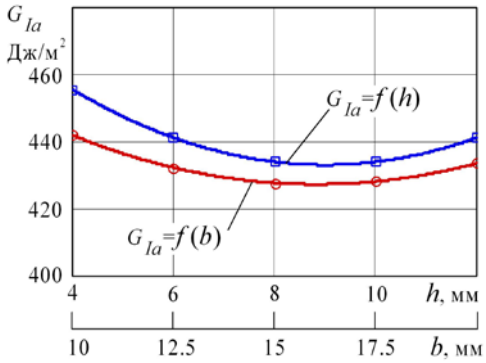


Рис. 4. Зависимость энергии продвижения трещины от размеров консольной балки в момент остановки трещины

Как видно из рис. 5 изменение толщины слоя клеевой композиции δ в 5 раз (с 0.5 до 2.5 мм) приводит к наибольшему изменению G_{Ic} и G_{Ia} соответственно на 3.37 % и 1.98 %.

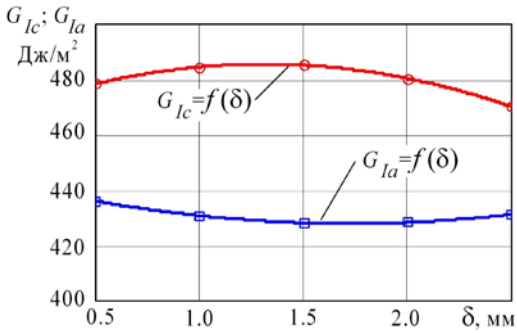


Рис. 5. Зависимость энергии продвижения трещины от толщины клеевой композиции

5. Conclusion

1. Предложена схема испытаний двойного консольного образца при которой его нагружение производится равными по величине и противоположно направленными моментами, что гарантирует идентичные условия образования трещин во всем объеме клеевой композиции.

2. Установлено, что при изменении геометрических параметров консольных балок и толщины клеевой композиции происходит незначительный разброс величины энергии продвижения трещины. Так при изменении в 2 раза размеров поперечного сечения $b \times h$ консольных балок разброс величины энергии продвижения трещины не превышает 0,37…1.24 %. При изменении в 5 раз толщины клеевой композиции δ разброс величины энергии продвижения трещины меняется в пределах 1.98…3.37 %.

3. Установлено, что покрытие на основе клеевой композиции ВАК-А имеет наибольшую трещиностойкость. Величины трещиностойкости клеевых композиций Спрут Плюс и Спрут 5М меньше на 19.9 % и 53.3 % соответственно, чем композиций на основе ВАК-А.

6. Литература

[1] Shields J. Adhesives Handbook. London-Wellington: Elsevier, 2013. 374 p.

[2] Gerdeen J.C., Lord H.W., Rorrer R.A.L. Engineering Design with Polymers and Composites. V.1. Boca Raton: CRC Press, 2005. 368 p.

[3] Croccolo D. Adhesives: Mechanical properties, technologies and economic importance. New York: Nova Science Publishers Inc, 2014. 153 p.

[4] Lees W.A. Adhesives in engineering design. Berlin: Springer Science & Business Media, 2013. 147 p.

[5] Weitzenböck J.R. Adhesives in Marine Engineering. Oxford–New Delhi: Woodhead Publishing Limited, 2012. 218 p.

[6] Scattina A., Roncato D., Belingardi G., Martino G. Investigation of creep phenomenon on composite material for bolt connections. Composite Structures, 2015. V.134. p. 378–383.

[7] Матлин М.М., Каблов В.Ф., Кейбал Н.А. Современные клеи и клеевые соединения в транспортных средствах. Волгоград: Изд-тво ВолгГТУ, 2011. 111 с.

[8] Бобович Б.Б. Неметаллические конструкционные материалы. Москва: МГИУ, 2009. 383 с.

[9] Коноплин А.Ю., Баурова Н.И. Особенности применения клеесварных технологий при ремонтных работах. Путь и путевое хозяйство, 2015. №6. с. 30–32.

[10] Кудрина А.В. Клеевые и герметизирующие материалы, применяемые в авиационной промышленности и в машиностроении. Энциклопедия инженера-химика, 2014. №6. с. 28–30.

[11] Игнатов А.В. Новые тенденции развития сборки клеевых соединений в машиностроении. Известия высших учебных заведений. Машиностроение, 2011, № 10. с. 62–68.

[12] Буйлов С.В., Корягин С.И., Пименов И.В., Маклахова И.С. Полимерные адгезивные материалы для производства и ремонта автомобилей. Вестник машиностроения, 2001. №1. с. 25-28.

[13] Осипов Н.Л., Пирожков В.А., Чабунин И.С. К вопросу о прочности полимерных композитов, применяемых в автомобилестроении. Известия Московского государственного университета МАМИ, 2014. Т.1. №2(20). с. 45–47.

[14] Терехин А.В., Русин М.Ю., Неповинных В.И., Думанский А.М. Работоспособность эластомерных клеевых соединений конструкций летательных аппаратов в условиях продолжительного теплосилового воздействия. Механика композиционных материалов и конструкций, 2015. Т.21. №4. с. 599-609.

[15] Грабильников А.С., Ларина Н.Д. Методы определения трещиностойкости клеевых соединений. Нестандартные методы исследования структуры и свойств полимерных материалов. Москва: МАТИ, 1990. Вып. 6. 24 с.

[16] Финогенов Г.Н. Метод испытания клеевых соединений металлов на трещиностойкость. Клеи. Герметики. Технологии, 2007, №5. с. 24–26.

[17] Мурашов В.В. Диагностика прочности клеевых соединений. Клеи Герметики Технологии, 2008. №8. с. 20-27.

[18] Молодницкий В.И. Методика ускоренных испытаний клеевых соединений. Технология машиностроения, 2006. №8. с. 68-70.

[19] Финогенов Г.Н., Петрова А.П. Ресурсная прочность клеевых соединений. Клеи. Герметики. Технологии, 2005. №11. с. 29-30.

[20] Malysheva G.V. Predicting the endurance of adhesive joints Polymer Science. Series D, 2014. V.7. №2. p.145-147.

[21] Derewonko A., Godzimirski J., Kosiuczenko K., Niezgoda T., Kiczko A. Strength assessment of adhesive-bonded joints. Computational Materials Science, 2008. V.43. №1. p. 157-164.

[22] Goyal V.K., Johnson E.R., Goyal V.K. Predictive strength-fracture model for composite bonded joints. Composite Structures, 2008. V. 82. № 3. p. 434-446.

[23] Ávila A.F., Bueno P.O. An experimental and numerical study on adhesive joints for composites. Composite Structures, 2004. V. 64. № 3-4. C. 531-537.

[24] Gift M.D.M., Selvakumar J., Alexis, S.J. Fracture studies of an adhesive joint involving composition alteration. Journal of Chemical and Pharmaceutical Sciences, 2015. V. 2015-April, p. 269–273.

[25] Chai H., Fox J. On delamination growth from channel cracks in thin-film coatings. International Journal of Solids and Structures, 2012. V.49. Issue 22. p. 3142–3147.

[26] Meneghetti G., Quaresimin M., Ricotta M. Damage mechanisms in composite bonded joints under fatigue loading. Composites Part B: Engineering, 2012. V.43, Issue 2. p. 210–220.

[27] Tsai M.Y., Morton J. An investigation into the stresses in double-lap adhesive joints with laminated composite adherends. International Journal of Solids and Structures, 2010. V.47. №24. p. 3317-3325.

[28] Корягин С.И. Несущая способность композиционных материалов. Калининград: Янтарный сказ, 1996. 301 с.

[29] Полилов А.Н. Экспериментальная механика композитов. Москва: Изд-тво МГТУ им. Н.Э. Баумана, 2015. 376 с.

[30] Черепанов Г.П. Механика разрушения композиционных материалов. М.: Наука, 1983. 296 с.

[31] Партон В.В., Морозов Е.М. Механика упруго-пластического разрушения. М.: Наука, 1974. 416 с.

[32] ISO 4587:2003. Adhesives. Determination of tensile lap-shear strength of high strength adhesive bonds. Geneva: ISO, 2003. 3 p.

[33] ASTM D 5041:2012. Standard Test Method for Fracture Strength in Strength in Cleavage of Adhesives in Bonded Joints, USA. ASTM, 2012. 5 p.

[34] BS 5350-C7:1990. Methods of test for adhesives. Adhesively bonded joints: mechanical tests. Determination of creep and resistance to sustained application of force, London: BSI, 1990. 3 p.

[35] DIN EN 15337:2011. Testing of adhesives for metals and adhesively bonded metal joints; compression shear test, Berlin: DIN. 2 p.

[36] Буйлов С.В., Корягин С.И., Ляшенко Б.А. Исследование трещиностойкости клеевых соединений. Проблемы прочности, 1987. №3. с. 52-56.

[37] Буйлов С.В., Корягин С.И. Метод определения трещиностойкости клеевых соединений. Заводская лаборатория, 1988. Т.54. №4. с.81-83

DATABASE DESIGN AT SYNTHESIS OF ELECTROMECHANICAL MODULES

Assoc. Prof. Dahterova D., M. Eng. Nikolova I.

Technical University of Sofia, Faculty of Engineering and Education – Sliven, Sliven, Bulgaria

dimitrinka_sl@yahoo.com

Abstract: *In accordance with the global concepts for machine design based on the modular principle, the main modules, which are the same for the different types of working machines, are the electromechanical modules, also called geared-motor modules. Because of the multivariance of the task for their design, a database containing the technical parameters and characteristics of the main constructive units needs to be build.*

Key words: ELECTROMECHANICAL MODULES, DATABASE, GEARED-MOTOR, ELECTRIC MOTOR, GEAR REDUCER

1. Introduction

The electromechanical modules (EMM) represent the constructive unification of the electrical and the mechanical part of the drives of the different types of working machines. In the majority of cases, the combination is between an electrical motor and a gear reducer, known also in the literature and the practice under the name geared-motor, respectively geared-motor module. In some case, the connection between the electric motor and the gear reducer is realized by means of a clutch. Depending on the selection of electric motor, gear reducer and clutch, at the same values for the input data, the realization of multiple variants of EMM is possible [Genova, etc. 2011]. Their unification in a single database facilitates the process for selecting the suitable for a concrete application EMM, as well as gives an opportunity for creating a software for optimal selection.

2. Formulating the problem

In terms of the structure, the database (DB) must contain information about the main constructive units of the EMM – electric motors, gear reducers and clutches. At certain point, this can turn out to be large amount of data, for the unification of which in a single DB, the most simple and functional structure that is easy to update and maintain needs to be built. Furthermore, the interface of the database needs to be user-friendly and to ensure fast and easy access to the information. This can be achieved by designing a relational DB, which is the most commonly used type [Hernandez 2003]. This is due to the fact that in comparison with the other models – hierarchical, network and object-orientated, at the relational DB structuring and updating the information, as well as building the relations between the separate tables is performed very easy. The nature of a relational DB is the correct building of the relations between the different tables that compose it [Garcia-Molina et al., 2009].

Fig. 1 shows an exemplary block-scheme of the general view of the database structure. The rectangles indicate the main tables that built the database – electric motors, clutches, gear reducers and the possible combinations between them. These tables contain technical parameters of the components:

- table electric motors – type of motor (for AC or DC current, asynchronous, synchronous, etc.), nominal power, nominal and synchronous speed of the motor shaft, nominal and maximal torque, nominal current, efficiency, IE efficiency class, weight, manufacturer;
- table gear reducers – type of gear reducer (cylindrical, bevel, worm, etc.), number of stages, mounting (horizontal or vertical), ration, efficiency;
- table electromechanical modules – the possible combinations between electric motors and gear reducers and their respective technical and geometrical parameters.

The blue rhomb indicates between which tables a relationship needs to be built. The block-scheme given on fig. 1 is exemplar. The information, which is contained in the tables, could be supplemented or removed, as well as the tables themselves.

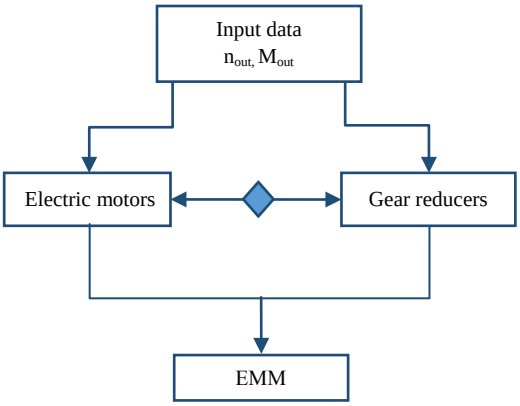


Fig. 1 Block-scheme of exemplary structure of the DB

3. Designing the database

In order to build a database, the so-called database management systems (DBMS) are used. These are the programs (software) by which a DB is designed and which ensures fast access to them and gives the opportunity for their updating and maintenance. One of the most commonly used DBMS are Oracle, MS Access, Paradox, FoxPro, Sybase, dBase, etc.

We have developed two versions of the database, using the software MS Access 2013. These versions differ from each other concerning their structure.

Version 1:

This version is the simplest one. It consists of only one table (shown in Table 1). The table contains information about all possible combinations of the structural units, obtained based on the input data. In order to simplify as much as possible the DB, the geometrical parameters of the obtained variants of EMM and some of the technical data about the electric motors and the gear reducers were exported in a separate file, for every concrete variant. The access to these files is done by clicking on the according hyperlink in the Gear_Mot_ID field.

For the convenience of the user, a search form has been created. Upon entering values for the input data and clicking on the functional button “Search”, the search results are outputted. This is done by the means of a so-called query, in which search criteria based on the entered values for the input data are assigned. Fig. 2 shows the general view of this query.

Version 2:

This version of the DB also consists of a table with the technical parameters of the possible combinations of EMM – identical in its

structure with the table in the first version, but in this case, there are also two more tables.

One of the tables contains data about electric motors of concrete companies and the other one contains data about the different types of gear reducers. In all three tables, there is one field, which indicates the identification number of every single record (row). This identifier is the so-called primary key and is unique for every record. The relations between the tables are built with the help of these primary keys. Another auxiliary table is built, which connects the three main tables, because it is not possible to create more than one relation from a single primary key.

This version of the DB also have a search form, which is identical with the form from the other version. The difference here is in the query, at which not only the search criteria are defined, but also the relations between the tables. Thereby, upon entering values for the input data in the search form and clicking on the functional button "Search", the results show preliminary defined fields from all tables. Fig. 3 shows the general view of the query for version 2 of the DB.

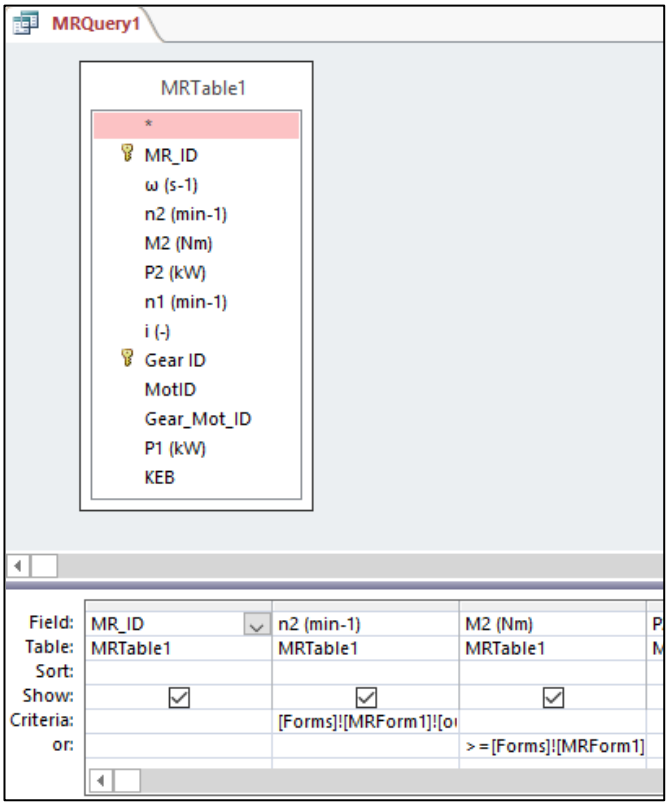


Fig. 2 Query - version 1

4. Numerical example

EMM design at the following input data: n_{out} = 65 min^{-1}; M_{out} = 95 Nm.

Depending on the type of the electric motor and the gear reducer, different variants of EMM are obtained. The database – electric motors contains asynchronous squirrel cage motors with different number of pole pair, i.e. different values for the speed of the input shaft n_{in}, namely: 2-pole electric motor (n_{in} = 3000 min^{-1}), 4-pole electric motor (n_{in} = 1500 min^{-1}), 6-pole electric motor (n_{in} = 1000 min^{-1}) and 8-pole electric motor (n_{in} = 750 min^{-1}).

The input power is calculated (P_{in} = 0,67 kW), based on the output power (P_{out} = 0,65 kW) and previously accepted indicative value for the efficiency. For the concrete case, an electric motor with nominal power $P_{nom.}$ = 0,75 kW has been selected that guarantees the realization of the input data. The ratios are calculated, based on which are defined the gear reducers by which these variants can be obtained – cylindrical, bevel, cylindrical-bevel, worm and worm-cylindrical. 51 different variants of EMM are obtained. Fig. 4 shows the results of the search in the search form of version 1 of the DB, and fig. 5 shows the results at version 3 of the DB.

5. Conclusion

Version 2 of the DB is more complex, but updating and maintaining such structure is easier. Also, the volume of the DB is smaller, because at his version there are no external files.

At version 1, for every EMM that is added in the DB, a new file with technical parameters of the electric motor and gear unit, that comprise it, needs to be created, which additionally compounds the DB. On the other hand, at version 1 the information is better illustrated in the search form, because the user can open only the file with technical data of this variant of EMM that satisfies its requirements.

Acknowledgments: this development is financed by the NATIONAL FUND for "Scientific research" under contract No. 152ПД 0060-06/ 2015.

6. Literature

Genova P., Dahterova D., Tsoneva M., Theory of machine design. Sofia, 2011.

Hernandez M. Database Design for Mere Mortals™: A Hands-On Guide to Relational Database Design, Second Edition. USA, 2003.

Hector Garcia-Molina H., Ullman J., Widom J. DATABASE SYSTEMS The Complete Book, Second Edition. USA, 2009.

Table 1: General view of the table in the first version of the DB

MR_ID	ω	n_{out}	M_{out}	P_{out}	P_{in}	n_{in}	i	Gear_Mot_ID
MRi i=1, 2, .. n	const calc	const	const	const calc	const calc	var	var calc	var hyperlink

Description: const-constant values; var-variable value; calc-calculated values; hyperlink-link to external file; MR_ID – identification number of all of the obtained variants; ω – input angular speed, it is calculated, [s^{-1}]; n_{out} – output speed, [min-1]; M_{out} – output torque, [Nm]; P_{out} – output power, it is calculated, [kW]; P_{in} – input power, it is calculated, [kW]; n_{in} – input speed, [min-1]; i – ratio, it is calculated, [-]; Gear_Mot_ID – hyperlink type of field

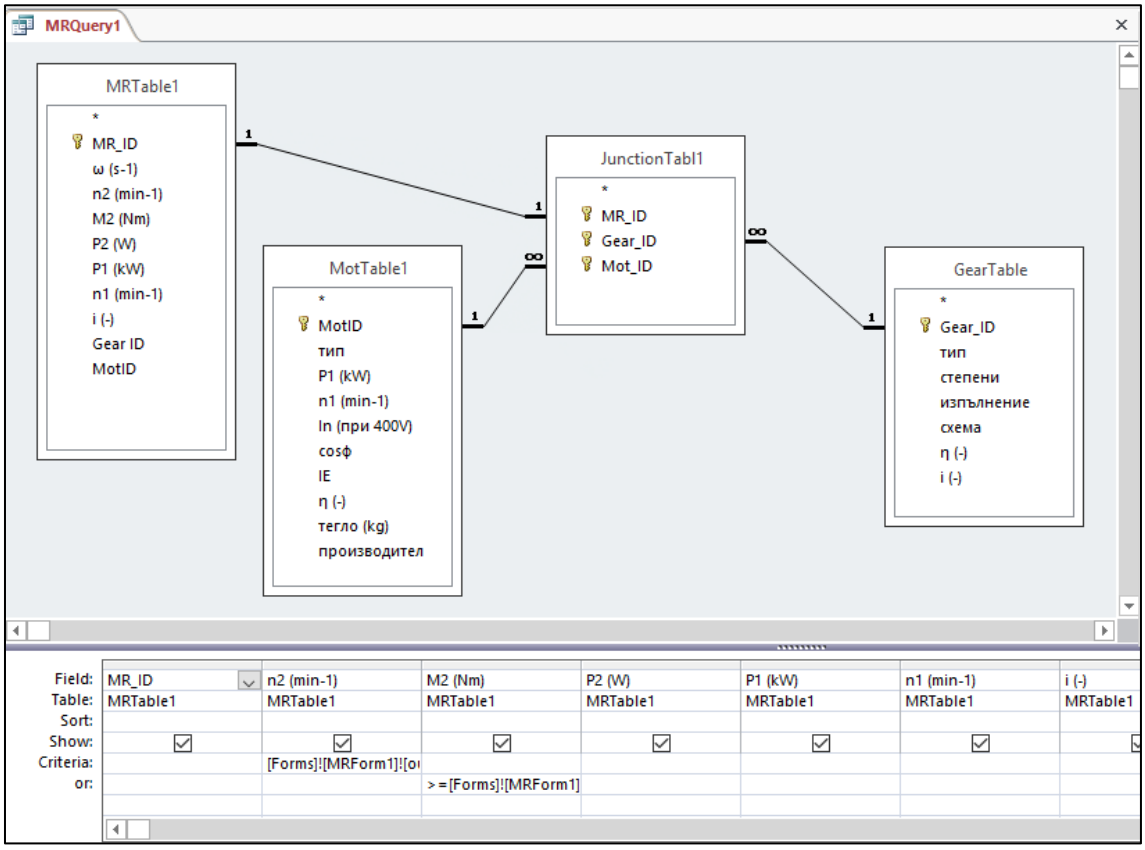


Fig. 3 Query – version 2

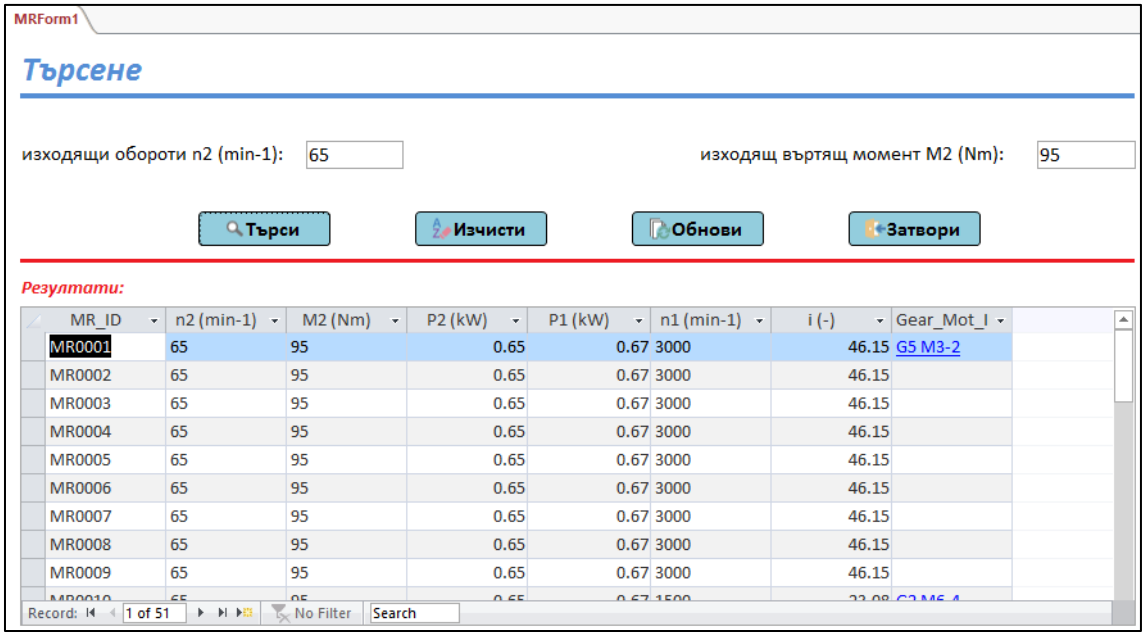


Fig. 4 Results from the search (version 1 of the DB)

MRForm

Търсене

изходящи обороти n2 (min-1): 65

изходящ въртящ момент M2 (Nm): 95

Търси | Изчисти | Обнови | Затвори

Резултати:

MR_ID	n2 (min-1)	M2 (Nm)	P2 (W)	P1 (kW)	n1 (min-1)	i (-)	Gear_ID	тип	степени	
MR0001	65	95	0.65	0.67	3000	46.15	G5	цилиндричен	тристъпален	x(
MR0002	65	95	0.65	0.67	3000	46.15	G6	цилиндричен	тристъпален	x(
MR0003	65	95	0.65	0.67	3000	46.15	G7	цилиндричен	тристъпален	x(
MR0004	65	95	0.65	0.67	3000	46.15	S1	червячен	едностъпален	x(
MR0005	65	95	0.65	0.67	3000	46.15	S2	червячен	едностъпален	x(
MR0006	65	95	0.65	0.67	3000	46.15	S3	червячен	едностъпален	x(
MR0007	65	95	0.65	0.67	3000	46.15	S4	червячен	двустъпален	x(
MR0008	65	95	0.65	0.67	3000	46.15	S5	червячно-цилиндричен	двустъпален	x(
MR0009	65	95	0.65	0.67	3000	46.15	S6	цилиндрично-червячен	двустъпален	x(
MR0010	65	95	0.65	0.67	1500	23.08	G2	цилиндричен	двустъпален	x(
MR0011	65	95	0.65	0.67	1500	23.08	G3	цилиндричен	двустъпален	x(
MR0012	65	95	0.65	0.67	1500	23.08	G4	цилиндричен	двустъпален	x(
MR0013	65	95	0.65	0.67	1500	23.08	G5	цилиндричен	тристъпален	x(
MR0014	65	95	0.65	0.67	1500	23.08	G6	цилиндричен	тристъпален	x(
MR0015	65	95	0.65	0.67	1500	23.08	G7	цилиндричен	тристъпален	x(
MR0016	65	95	0.65	0.67	1500	23.08	K2	конусно-цилиндричен	двустъпален	x(

Record: 1 of 51 | No Filter | Search

Fig. 5 Results from the search (version 2 of the DB)

METHODOLOGY OF CARRYING RESEARCHES OF KINEMATIC PAIR OF PIVIOTING FRICTION

Ph.D. Eng. Wozniak M.[1], Ph.D. Eng.Kubiak P. [1], M.Sc. Eng. Jozwiak P. [1], Eng. Madziara S. [1], Eng. Najbert S. [1], Prof. M.Sc. Ozuna G.[2], Ph.D. Eng. Chunbao L. [3]
Department of Vehicles and Fundamentals of Machine Design – Lodz University of Technology, Poland
Department of Industrial Engineering and Systems - University of Sonora, Mexico [2]
State Key Laboratory of Mechanical Transmission, Chongqing University, Chongqing, China [3]

marek.wozniak.1@p.lodz.pl, przemyslaw.kubiak@p.lodz.pl, jozwiak.piotr@gazeta.pl, 171243@edu.p.lodz.pl, 174616@edu.p.lodz.pl, , gozuna@industrial.uson.mx,

Abstract: *The paper presents the program and methodology of carrying out research on kinematic pair with pivoting friction. There was examined a node with pivoting friction in bearing concentrated connection flat surface-spherical bowl. During the research there were determined two types of characteristics – characteristic of friction moment as a function of load and experimentally designated characteristic of wear of the frictional kinematic pair. Both of the assigned characteristics are compared..*

Keywords: MOMENT OF FRICTION, PIVOTING FRICTION, FRICTION COEFFICIENT, WEAR

1. Introduction

The phenomenon that occurs between two bodies in contact in rest or in motion is called friction. As a result of this phenomenon there arises resistance to motion. There are various kinds of friction distinguished (figure 1).

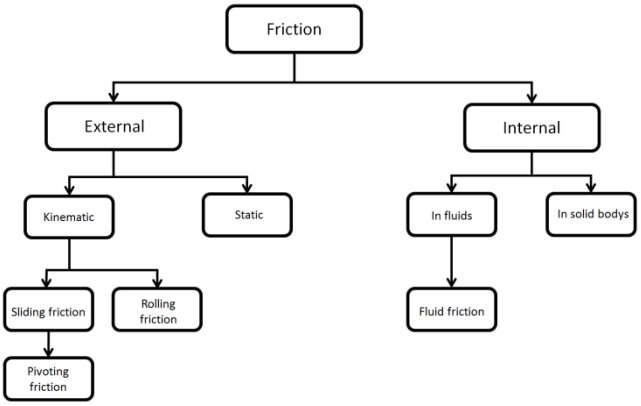


Fig. 1 *Types of friction [4].*

Machines constructors try to eliminate dry friction, replacing it with more advantageous fluid friction. Due to the fact that co-operating surfaces are not ideally smooth, on the top of the irregularities of the surface there could occur dry or boundary friction, whereas the cavities could be filled with lubricant. In such conditions the friction between the rough contact surfaces is so called mixed friction [2].

2. Pivoting friction

One particular case of sliding friction that occurs in slide bearings is pivoting friction, caused by continuous rotation or oscillation around the normal in point of contact between two cooperating surfaces. Pivoting friction occurs in the bearings: measuring timing devices, analogue scales, spindles, textile machinery etc. This paper attempts to analyze the conditions of pivoting friction for bearing model: flat surface - spherical bowl (figure 2). In this type of bearings obtaining fluid friction, even in case of total immersion of lubricating agent node (figure 3), is not possible due to the scattering of the gaps.

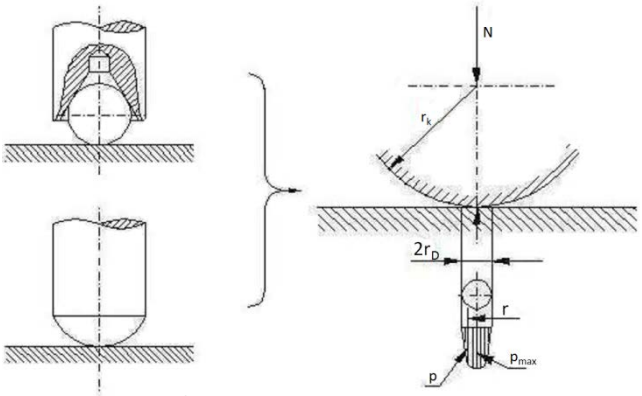


Fig. 2 *Model of the bearing type spherical cap on plate; p - Hertz pressure, p_{max} - Hertz pressure maximum [3].*

$$p_{max} = \frac{1}{\pi}\sqrt[3]{\frac{6 \cdot N \cdot \frac{1}{r_k^2}}{\left(\frac{1-\upsilon_1^2}{E_1}+\frac{1-\upsilon_2^2}{E_2}\right)^2}} \qquad (1)$$

where: υ - Poisson ratio, E - Young's modulus, N - axial force, r_o - contact radius, r_k - sphere radius.

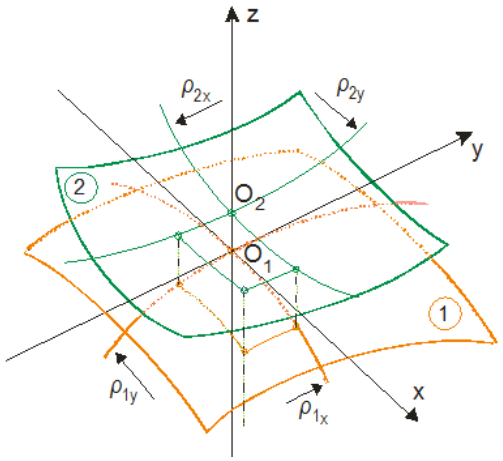


Fig. 3 *General model of the sidle bearing: r1, r2 – curvature radius of mating surfaces [5].*

3. Experimental research model

In the initial examination there was used a bearing ball made of steel 100Cr6 of diameter 8mm and a flat plate made of Ertalon. The test was performed only in conditions of dry friction, without the use of the lubricant.

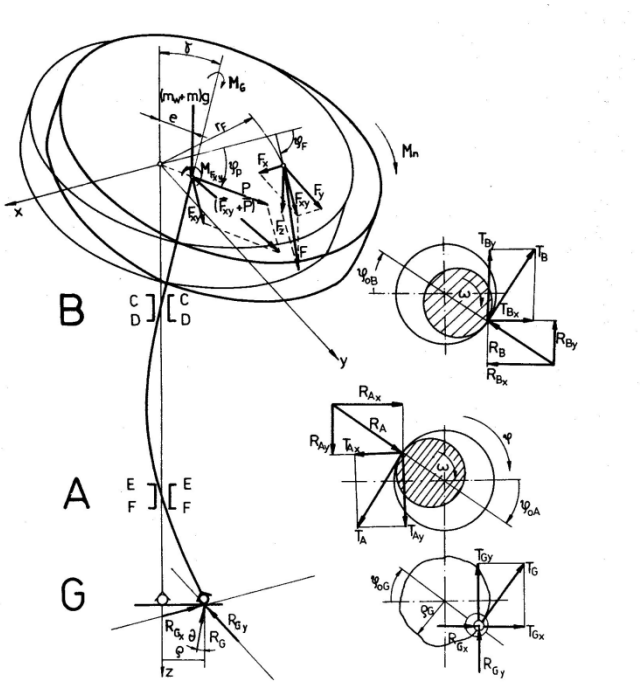


Fig. 4 *Scheme of general model of radial thrust bearing [1].*

4. Test bench

Figure 5 presents the test bench for determination of friction coefficient by the string twist angle measurement.

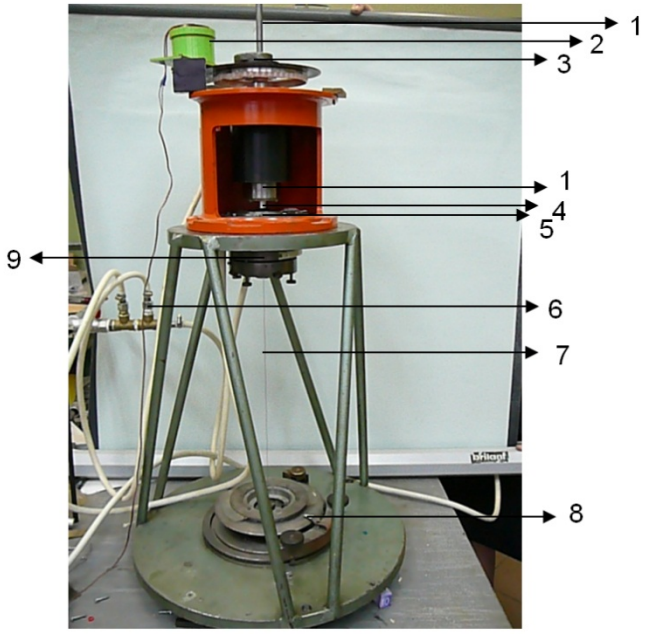


Fig. 5 *Test bench for the friction moment and friction coefficient for the frictional pair ball joint – spherical cap; 1 – shaft, 2 – electric motor, 3 – weights, 4 – sphere , 5 –sample, 6 –compressed air supply, 7 – string,8 – disc to read the angle of torsion, 9 – aerostatic table [6].*

The test bench is made of two cylindrical radial bearings and axial bearing. The drive from electric motor (2) is transferred by the belt transmission on the shaft (1) which is ended by the ball joint. The load is changed by adding weights (3) on the shaft (1). The tested ball joint (5) is placed on the aerostatic table (9) which is connected with the string (7). The second end of string is mounted to the table (8) which is used to twist string angle compensation. The angle of compensation is read from the scale plotted on the table (8).

5. Test bench researches

For the initial experiment there were selected bearing balls made of steel H-15 (100Cr6) of diameter 8 mm and a flat plate made of Ertalon (PA6-E). Experimental measurements were carried out by measuring the moment of friction as a function of load. In addition, the test results calculated due to the varying string angle verified friction torque values designated with signs of wear on the plate.

The test bench research was performed by the measurement of the torsional angle of the string as a function of load. The electric motor was started after mounting the plate from PA6-E and steel ball (100Cr6) to the test bench. The shaft rotated with constant speed – 36 rpm. Then the test bench was gradually loaded by 2 N in the range 7,09÷16,9N. After that the test bench worked in the inverse sequence. Weights were added for 500 cycles.

The smallest load due to the weight of shaft was 7,09 N and peak load was the sum of the weight of the shaft and weights. Each measurement was repeated in 10 measuring series in order to calculate the average value of the string twist angle. The moment of friction was determined according to the relationship:

$$M_t = 33{,}722 \cdot \mu \cdot p_{max} \cdot N \cdot r_k \cdot \left(\frac{1-\nu_k^2}{E_k} + \frac{1-\nu_p^2}{E_p} \right) \qquad (2)$$

Track wear plate measuring scanned using an optical microscope with a mounted camera. Assuming that the diameter of the wear scar is 2ro friction torque calculated from the relationship:

$$M_t = 2 \cdot \pi \cdot \mu \cdot p_{max} \cdot 7{,}1633 \cdot r_o^3 \qquad (3)$$

6. Measurement results

Below is a sample list of friction torque for the combination of friction couple: plate from ertalon (PA6-E) – steel ball (100Cr6).

Tab. 1 *Radius r_o of the wear traces on the plate in the function of load for the examined sample*

m_w [kg]	m [kg]	g[m·s^{-2}]	d_k [m]	ν_k	ν_p	$E_k \cdot 10^6$ [Pa]	$E_p \cdot 10^6$ [Pa]	$r_o \cdot 10^5$ [m]
0,723	0,0	9,81	0,008	0,308	0,298	210000	180000	5,71
	0,2							6,19
	0,4							6,61
	0,6							6,98
	0,8							7,32
	1,0							7,63

Tab.2 *Analytical values and values from traces of wear determined for the friction moment of the frictional pair ertalon-steel.*

Load [N]	p_{max} [Pa]	Friction μ [-]	Average moment of friction [Nmm]	Average friction μ [-]	Moment of friction from trace [Nmm]
7,09263	1,04 E+09	0,067029	0,00059	0,067846	0,00052487
9,05463	1,13 E+09	0,062566	0,000721	0,059811	0,00067849
11,01663	1,21 E+09	0,054026	0,000845	0,053975	0,00076099
12,09786	1,27 E+09	0,051049	0,000994	0,051049	0,00089470
14,94063	1,33 E+09	0,049443	0,001152	0,049041	0,00104548
16,96541	1,39 E+09	0,046451	0,001286	0,046451	0,00115785

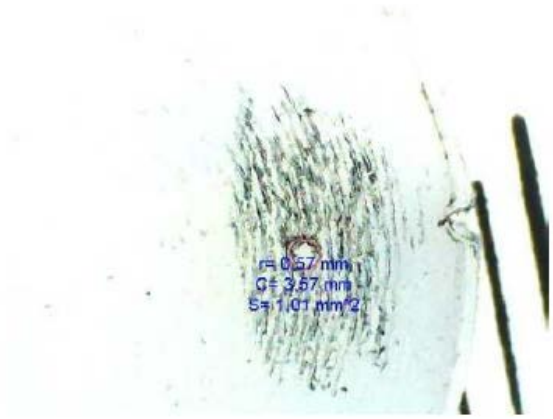
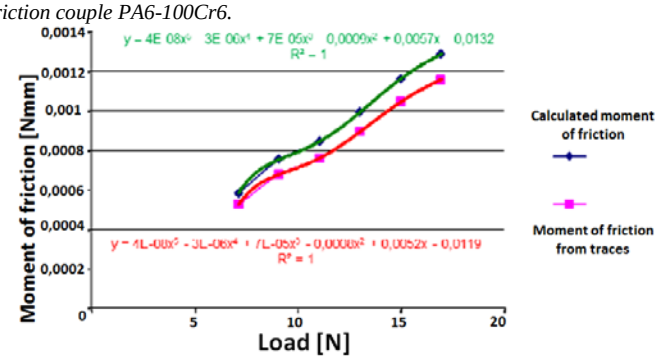


Fig. 6 *Example trace of wear on the flat surface, r_o=0,258 mm, S= 0,209 mm^2.*

Fig. 7 *Graph of moment of friction in function of load for the researches of friction couple PA6-100Cr6.*



6. *Summary*

1. The moment of friction increases proportionally to the load.
2. The characteristic of the friction momentum as a function of load determined analytically is the same as the characteristic determined by the wear.
3. Differences in momentum of friction for analytical calculations and the values determined from the exploitation do not exceed 0,00012 Nmm in the entire load range.
4. The values determined analytically were calculated for the springy connection. The values of friction momentum determined from the wear include the impact of the plastic deformation and the exploitation.

7. References

1. Burcan J.: *Analiza oporów ruchu i jej wykorzystanie w projektowaniu drobnych mechanizmów precyzyjnych*, Politechnika Łódzka, Zeszyty Naukowe Nr 546, rozprawa habilitacyjna, Łódź, 1989,
2. Dietrich M.: *Podstawy konstrukcji maszyn*, Tom 2, WNT, Warszawa 1999,
3. Wozniak M., Ozuna G., De La Fuente P., Jozwiak P., Pawelski Z.: *Comparision of friction coefficient for selected car suspension elements.* International Virtual Journal for Science, Technics and Innovations for the Industry MTM. Year VIII, Issue 4/2014, pp.23-25, ISSN 1313-0226,
4. Lawrowski Z.: *Tribologia – Tarcie, Zużywanie i Smarowanie*, Warszawa, PWN 1993,
5. Burcan J.: *Analiza oporów ruchu i jej wykorzystanie w projektowaniu drobnych mechanizmów precyzyjnych*. Zeszyty Naukowe nr. 546, Politechnika Łódzka, Łódź, 1989,
6. Wozniak M., Ozuna G., De La Fuente P., Jozwiak P., Pawelski Z.: *Comparision of researches of friction coefficient in concentrated contact for the stress: steel-steel and steel-magnesium alloys*. International Virtual Journal for Science, Technics and Innovations for the Industry MTM. Year VI, Issue 6/2013, pp.51-54, Bulgaria, 1-2.07.2013,

OPTIMIZATION OF GEOMETRIC PARAMETERS OF HARD METAL MICRO DRILS TO INCREASE TOOL LIFE AND PERFORMANCE OF DRILLING PACKAGE OF PRINTED CIRCUIT BOARDS

Doctor of science, Prof., Turmanidze R.[1], Senior laboratory Bachanadze V.[2], Undergraduate student Popkhadze G.[3]
Faculty of Transportation and Mechanical Engineering[1, 2, 3] – Georgian Technical University, Tbilisi, Georgia, inform@gtu.ge

Abstract: *In the presented work investigated the changes of power characteristics of deep drilling package of printed circuit board's hard metal micro drills depending on the drilling depth, cutting data and geometry of the drill. In particular studied the nature of changes in axial efforts and torque depending on the drilling depth drill with different inclinations of the spiral grooves using specially designed highly sensitive devices, enabling direct measurement method. Based on the analysis of the results of the study, changes in the geometry of existing standard drills. Proposed new construction of micro drills vary-angle spiral grooves in such a way that the angle is the maximum value at the top of the drill and uniformly decreases towards the end of the working parts. The drills are manufactured with different inclinations of the spiral grooves. Based on the experiments of them chosen more for its near standing power rates to the standard drill bit and its comparative test with a standard drill bit, bringing them up to the breakage, thanks to which the proven advantages of drills new design. Taking into account the results of the experiments proposed drill elongated structures to improve performance by increasing the processing drilling depth and accordingly the number of plates in the package of printed circuit boards.*
Keywords*: DRILL, GRADIENT OF SPIRAL GROOVE, VARIABLE ANGLE, DEVICE.*

1. Introduction

It is impossible to imagine modern equipment without electronic knots, starting from household and ending with space equipment. Printed circuit board's production, basic parts of electronic equipment associated with drilling process vast quantities of small diameter holes (about 1mm or less). Carry out drilling of micro carbide drill geometry, which has multiple experiments an experiences relevant production. In particular: the optimum cutting angle and spiral angle grooves respectively is 300, and the rear angle 180. They are refaced through each hole and 1000 are designed for 3-4 regrinding costs.

Production of printed circuit boards is mass production, where performance is carried out with the aim of increasing the drilling package, composed of several plates, it has a place of deep-hole drilling, where the drill depth exceeds the diameter of 8-10 times.

Downtimes of expensive technological equipment, especially in mass production are associated with significant economic losses. In the production of printed circuit boards easy connected not only with the replacement of the tool with the aim of reshaping, but unexpected, caused by fragile destruction even before the first reshaping. Probability of brittle fracture grows significantly during deep drilling package of printed circuit boards. When this zone is located in the near destruction of the end of the spiral grooves.

Providing the best mass production processes for manufacture of printed circuit boards, at least a slight increase in resistance, including fragile resistance micro drills and consequently increasing productivity processes, can provide significant economic benefits.

2. The Main Part

Research work with a view to enhancing the resistance of tungsten carbide micro drills and deep hole drilling process performance package of printed circuit boards were held in the laboratory precision micro instrumental Department "Industrial Technologies Engineering Mechanics", Georgian Technical University in close cooperation with specialists of the Institute of Manufacturing Technology and Quality Management (IFQ) Magdeburg University Otto-von-Guericke (Germany).

Studies were initiated the study of the nature of the change of power indicators-torque and axial reinforcement depending on the depth of cutting and drilling printed circuit board package from fiberglass.

To measure the axial effort was the appliance is made on the basis of known methods and existing analogs, measuring element, which is the system of strain gauges mounted on the elastic casing (see fig. 1).

As for measurement of a torque, in our case the existing indirect method at which measurement is carried out by means of measurement of power of process of cutting is unsuitable as we deal with very low indicators. That is why it is necessary to use this method, which will make it possible to measure directly the torque with high precision. To this end, we have designed and manufactured a special device (see fig. 2), in which table for drilling is equipped with rotating lever mechanism. As the measuring element, elastic element applies here too with the system of load cells, only the higher strain measure (0.2 g).

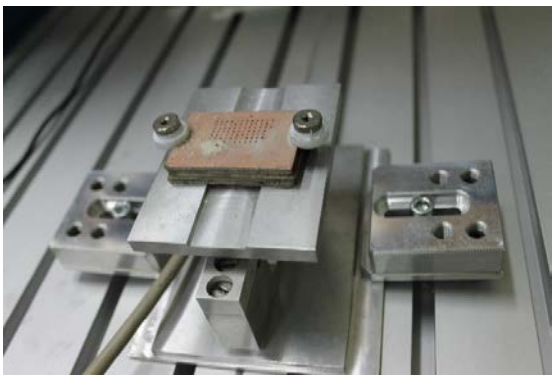


Fig. 1. Instrument for measuring axial efforts.

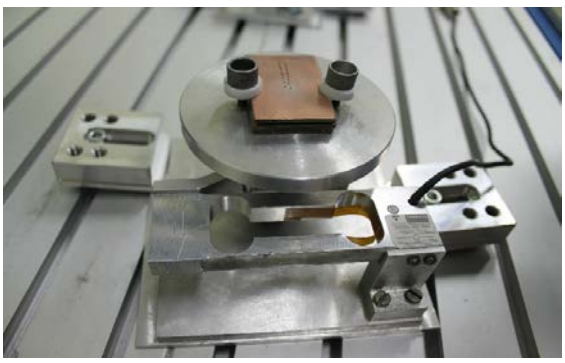


Fig. 2. The device for measurement of torque.

Experiments were conducted with drills from solid alloy VK60M diameter φ 0,9mm long spiral groove l=10mm. Rake angle and spiral angle grooves respectively $\omega=30^0$, rear angle was 18^0.

Drilling was carried out a package of printed circuit boards of fiberglass thickness 1.6mm composed of 5 plates with a total thickness of 8mm (see fig. 3).

Drilling of blanks is carried out on different modes of cutting depth up to 7 mm and 1 mm the depth of the recorded testimony

every depth controlled readings. Experimental results are shown in fig. 4 and 5.

From this results, clearly shows that the load power with increasing depth progressively increasing. If the axial thrust is growing, approximately 1.5 times the amount of torque is increased 3-4 times.

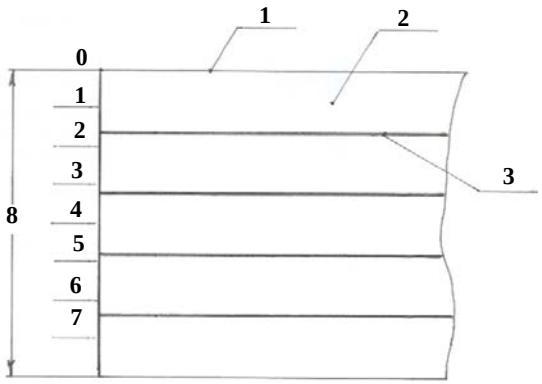


Fig. 3. Package diagram printed circuit boards of 5 plates. 1-copper foil, 2-fiber, 3-double layer of copper foil.

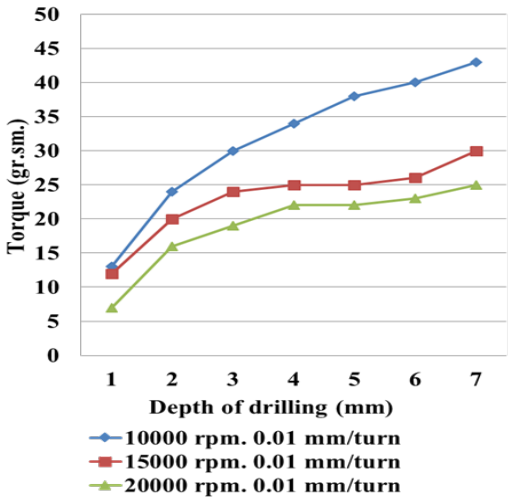


Fig. 4. The chart for standard drills $\omega = 30^0$.

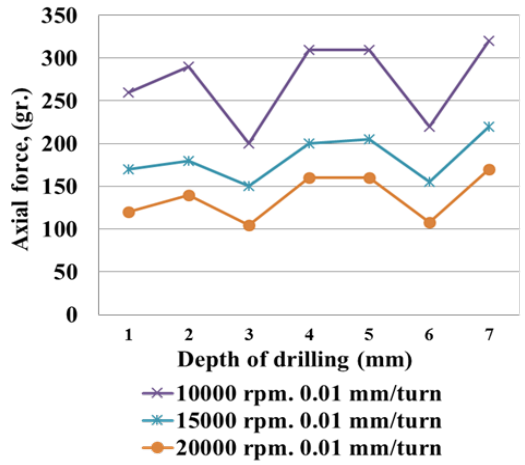


Fig. 5. The chart of axial efforts for standard drill $\omega = 30^0$.

Question, what caused this increase in power? Cutting conditions at the cutting edge of drills with increasing depth does not change. The only reason for this could be the increased contact area abrasive chips with the surface of the hole and emerged from it frictional forces.

You need to note that the sharp fall in axial efforts on areas of depth 2-3 and 5-6 (see fig. 5.) on these sites due to the lack of the work piece (fig. 3.) the copper layer.

The main factor increase the likelihood of brittle fracture of the cutting tool of these two power indicators may not increase the axial effort and more progressive increase in torque because the strength properties of carbide materials on the compression significantly exceed indicators of torsion.

Accelerating the process of chips from the cutting zone would contribute to the reduction of the force of friction and, consequently, improve the reliability of the drilling process. The problem of removal of chips when drilling deep hole in different cases decide in different ways. For example, when drilling drills dimensions solid this exercise method of leaching using a coolant, which is supplied, into the hole through, done in the body of the drill. In other cases, when the drill bit sizes do not give possibility of coolant above method to remove shavings used drilling method intermittent, where after a certain depth drilling is carried out periodically by the disqualification of drills from holes fast running.

The application of these techniques in our case nepriemlim. In the first case we have with micro drills. The use of coolant in the manufacture of printed circuit boards is not allowed. Design and method of intermittent drilling, because it led to the strong performance. When processing deep eyelet micro drills accelerating factor could be an increase in chip removal step spiral grooves, i.e. reducing the angle, but it would have led to a deterioration of the cutting conditions, so-as will decrease the cutting angle drills.

In the design of the drills carried out in a way that at the top of the save the desired cutting angle, and toward the end of the spiral grooves reduce its angle, IE a spiral groove cut into a vary-angle [1, 3, 4, 5, 6] and gradually increase its step, it would accelerate the process of chip and facilitate conditions for drilling.

Fig. 6 shows the scheme of drills with vary-angle spiral grooves where the angle of the grooves at the top of the drill ω_0, and at the end of the working part of ω_1. The width of the grooves in the normal section B_n on all length does not change, but the change in the front section and at the top is $B_{To} = \frac{B_n}{\cos\omega_0}$, and at the end of the working parts $B_{T1} = \frac{B_n}{\cos\omega_1}$.

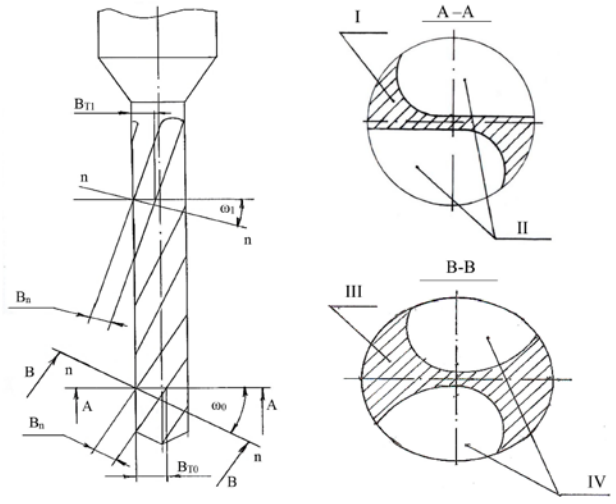


Fig. 6. Drill scheme with vari-angle spiral grooves, I – The useful mechanical section of the drill, II – Face section of the groove, III – Useful normal section of the drill, IV – Normal section of the groove.

Changing and useful mechanical drill section. Useful section at the top: $S_o = \frac{\pi d^2}{4} - \frac{2S_n}{\cos\omega_0}$, and at the end of the working

parts: $S_1 = \frac{\pi d^2}{4} - \frac{2S_n}{\cos\omega_1}$, where S_n - square grooves in the normal section, d - is the diameter of the drill.

If you take into account that $\omega_0 > \omega_1$, it turns out that toward the end of the working part of the useful cross-section drills intensifies. Then there are drills compared to standard must withstand stress.

Production of such drills associated with certain difficulties. At production of standard drills with a constant tilt angle of a spiral flute the special adaptation carries out the mutually agreement two movement – rotations of preparation of a drill and its movement in the axial direction at a size of a step of a spiral flute. Thus, this interrelation is defined by linear function. In case of a variable step, this interrelation is defined by difficult tangential function. Because of it was necessary to modernize the equipment and its mechanism of axial giving of an element with the Archimedean spiral to replace elements with a tangential spiral, made by our special calculations [2, 3, 4, 5].

Besides, because of a variable tilt angle of a spiral flute, at you - polishing of these flutes should change orientation of a grinding wheel relatively to an axis of preparation of a drill respectively to change of a tilt angle of a flute. It can be carried out in two ways: at a motionless axis of a grinding spindle to turn a preparation spindle axis round a point of intersection of these axes at a corner size $\omega = \omega_0 - \omega_1$ (see figs. 7), or motionless to leave an axis of a spindle of preparation and to turn an axis of a grinding spindle (see figs. 8) [7].

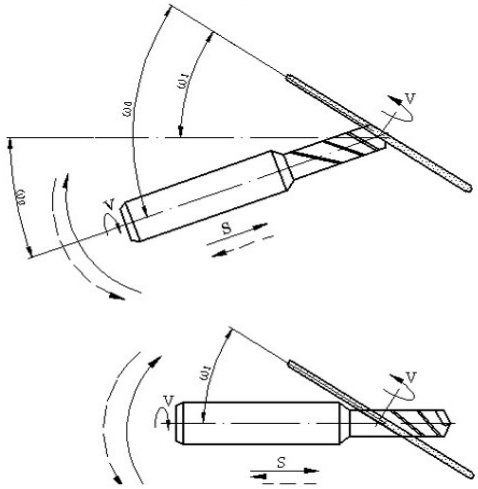


Fig. 7. Schemes of change of orientation of axes of a spindle of preparation of a drill and grinding spindle. Method of turn of an axis of a spindle of preparation.

Proceeding from constructive reasons the preference was given by us to the first option (figs. 7) and in the course of modernization of the equipment it was equipped with the additional mechanism of turn providing when cutting spiral flutes, turn of an axis of preparation of a drill relatively to an axis of a grinding spindle at a corner size $\omega = \omega_0 - \omega_1$ thus depending on are long the cutting part of a drill turn is carried out by the linear law: $\omega_x = \ell_x \cdot K_\omega$, where ω_x - the current size of an angle of rotation of an axis of preparation, ℓ_x - the current coordinate of length of the cutting part of a drill, K_ω - the size of change of a tilt angle of a spiral flute per unit length the cutting part of a drill.

We have designed constructed prototypes of drills with vary-angle $\omega = 30 - 17^0$, $\omega = 35 - 20^0$, $\omega = 40 - 22^0$ and $\omega = 43 - 23^0$.

All of these included circuit boards same experiments as the standard. Experimental results for drills $\omega = 30 - 17^0$ and $\omega = 35 - 20^0$ are shown on fig. 9 – 12.

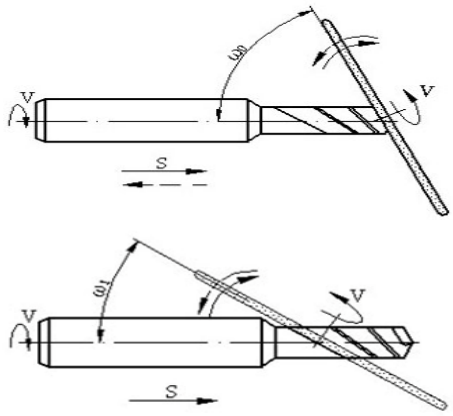


Fig. 8. Schemes of change of orientation of axes of a spindle of preparation of a drill and grinding spindle. Method of turn of a grinding spindle.

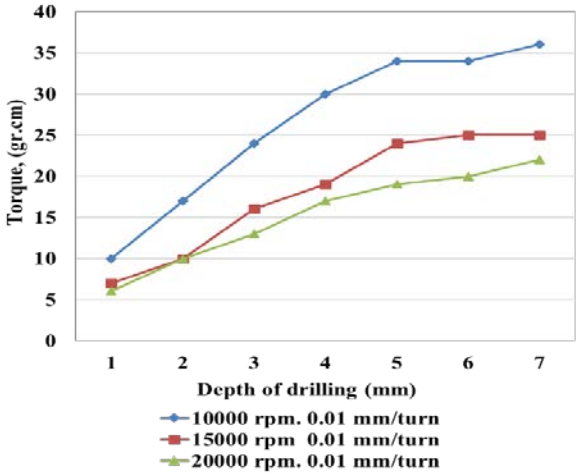


Fig. 9. The chart of change of a torque for drills $\omega = 30 - 17^0$.

Analysis of these graphs shows the following: for drills $\omega = 30 - 17^0$ performance of axial efforts almost indistinguishable from a standard drill bit $\omega = 30^0$, so, it was expected, because these same drill front angle and cutting conditions respectively at the cutting edge. With regard to indicators of torque, they drill $\omega = 30 - 17^0$ depending on the cutting was understated by 12-16%.

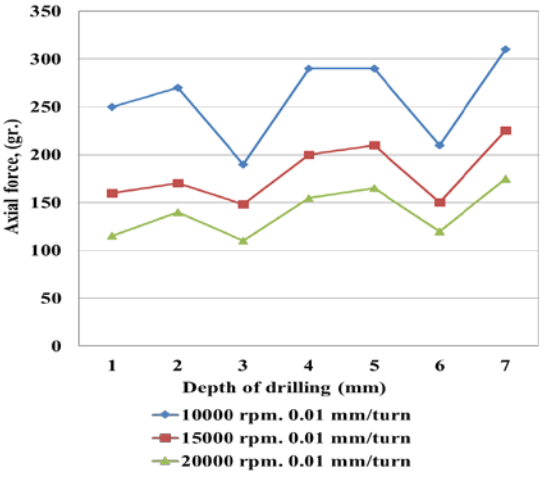


Fig. 10. The chart of changes of axial efforts for drills $\omega = 30 - 17^0$.

For drills $\omega = 35 - 20^0$ performance of axial efforts relatively understated, as rake angle increased by 5% and this facilitated the process of cutting, but indicators of torque with increasing depth drilling grows more intensively and exceed indicators of both previous designs. It is clear that the understatement of torque to drills $\omega = 30 - 17^0$ compared with standard drills $\omega = 30^0$, due to the gradual increase in step spiral grooves and accordingly reduced contact area formed by chips with processed apertures. Increasing the angle of inclination and therefore a decrease in pitch of spiral drills $\omega = 35 - 20^0$ again causes the reverse-torque figures intensively promoted.

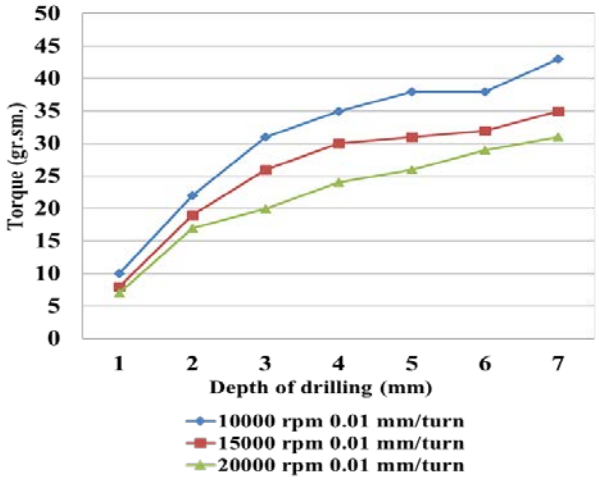


Fig. 11. The chart of torque for drills $\omega = 35 - 20^0$.

When drilling by drills of $\omega = 40 - 22^0$ and $\omega = 43 - 23^0$ these power indicators are rather underestimated (see figs. 13-16) that is explained by improvement of conditions of cutting because of considerable (5-8^0) increases in a forward corner at the cutting edge. However, reduction of a corner of a point at further operation causes increase in intensity of wear, and they without repoint reach only 600-800 openings.

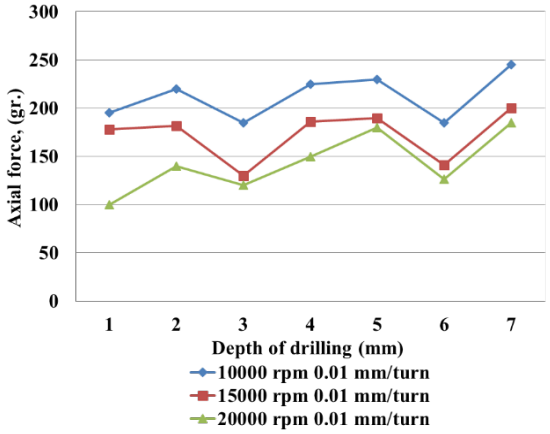


Fig. 12. The chart of changes of axial efforts for drills $\omega = 35 - 20^0$.

Obviously, to get a clearer picture further experiment need to keep standard drills $\omega = 30^0$ and drills with vari-angle spiral grooves $\omega = 30 - 17^0$. Experiments were continued until the breakdown drills. Through each hole 200 checked power indicators, with increasing cutting edge wear gradually increases. After 1000 holes check carried out through every 100 holes, as increasing the likelihood of breakage of drill. Throughout a series of experiments for both types of drills, $\omega = 30^0$ nearly identical indicators remain innovative wear and axial efforts. As for torque, its value on the standard drills always exceed the value of drills with variable angle of the spiral grooves $\omega = 30 - 17^0$.

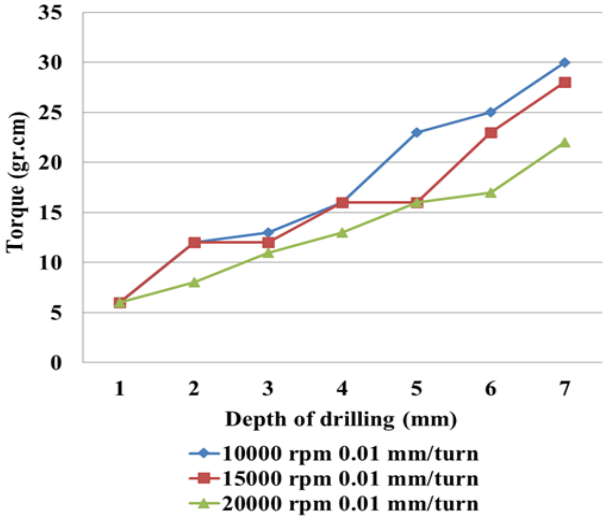


Fig. 13. The chart of change of a torque for a drill $\omega = 40 - 22^0$.

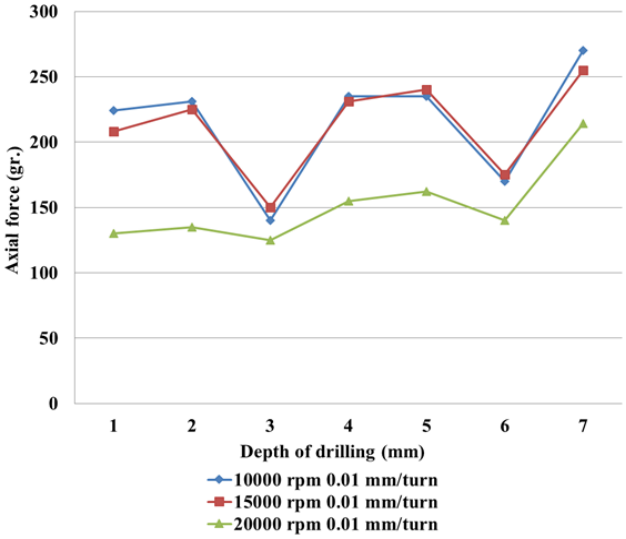


Fig. 14. The chart of change of axial effort for drills $\omega = 40 - 22^0$.

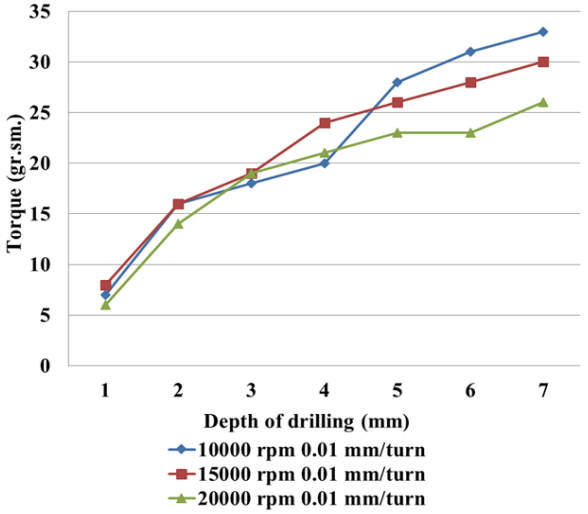


Fig. 15. The chart of change of a torque for drills $\omega = 43 - 23^0$.

Statistics showed that the breakage of the standard drills $\omega = 30^0$ going from 1200 to 1300 holes and drill with vari-

angle $\omega = 30 - 17^0$ from – 1400 to – 1500. Performance torque values before breakdown indicating the number of drilled holes N traversed the path L and size of wear on back surface drills f shown in Fig. 17 and 18.

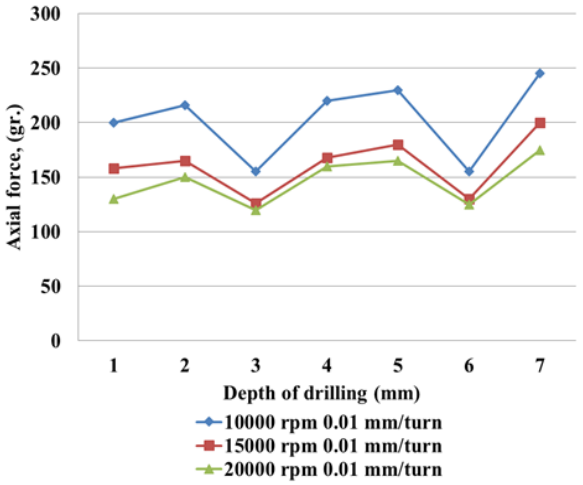


Fig. 16. The chart of change of axial effort for drills $\omega = 43 - 23^0$.

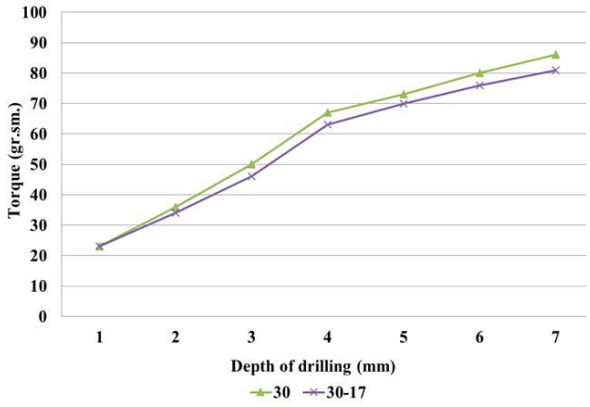


Fig. 17. The chart of torque graph for drills $\omega = 30^0$ and $\omega = 30 - 17^0$ before the breakdown drills $\omega = 30^0$.

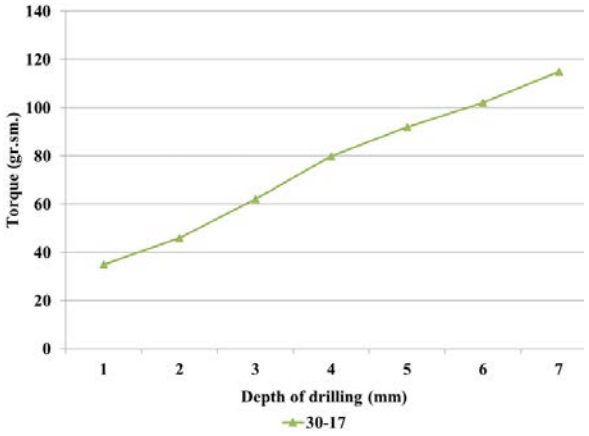


Fig. 18. The chart of change the torque diagram for drills $\omega = 30 - 17^0$ before its breakdown.

3. Conclusions

Solid Carbide micro drills with vary-angle spiral grooves in deep drilling package provides improved chip control process intensity of hole, promoting this underestimates the force of friction and consequently the torque on the axis of the drill.

Implementation of the spiral grooves with a gradual lowering of the ω-angle from the top of the drill toward the end of the working part provides useful cross-section reinforcement drills, increasing the reliability of the brittle.

On the basis of the foregoing, it becomes possible to manufacture drills with elongated working part at 2-2, 5mm and in the package circuit boards add another plate, which will make it possible to improve the performance of drilling process on 20%.

4. Literature

1. B.Karpushewski, R.Turmanidze, L.Dübner, O.Kushnarenko. Erhohung der standzeit und prozesssicherheit von mikrobohrern durch die entwicklung neuer werkzeuggeometrien. Collection of scientific works “Modern technologies in mechanical engineering”, publishing house of the Kharkov national technical university "KPI". Release 2. Kharkov, 2008 year. Pages 27-32.
2. D.Adamia, Z.Gviniashvili, V.Bachanadze. Peculiarities of formation of shavings grooves of spiral drill of hard alloy with variable inclination. Scientific technical journal “Transport and Machinebuilding” 2009 year. Edition No. 3(15). Publishing house “Transport and Machinebuilding”. Pages 133-140.
3. R.Turmanidze, O.Kushnarenko, D.Adamia, Z.Gviniashvili. Small-sized hard metal spiral drills with variable angle of inclination chip grooves. Collection of scientific works “Modern technologies in mechanical engineering”, publishing house of the Kharkov national technical university "KPI". Kharkov, Release 5, 2010 year, Pages 318-327.
4. R.Turmanidze, D.Adamia, Z.Gviniashvili. Peculiarities of Manufacture and Tests of Fine-Sized hard-metal Spiral Drills with Variable Setting Angle of Chip Grooves. Proceedings of the 17th international scientific and technical conference “Mechanical Engineering and Technical Sphere of the XXI century”, 13-18 September 2010 year, in Sevastopol. Donetsk National Technical University. Volume 3. Pages 181-184.
5. R.Turmanidze, O. Kushnarenko, D. Adamia, Z. Gviniashvili. Fine-sized hardmetal spiral drills with variable setting angle of chip grooves. 10th International scientific conference “New Ways in Manufacturing Technologies – NWMT 2010. 17-19 June 2010year. Prešov, Technical University of Košice, Faculty of Manufacturing Technologies, Košice, Slovak Republic. Pages 217-226.
6. R. Turmanidze, Z. Gviniashvili. Fine-sized hard metal spiral drills with variable setting angle of chip grooves. Selected, peer reviewed papers from the 6th International Congress of Precision Machining ICPM 2011. 13th–15th September 2011year. Liverpool John Moores University, Day 1. Liverpool. Pages 253-258.
7. D. Adamia, Z. Gviniashvili, L. Tediashvili, V. Bachanadze. Destination of swing-out mechanism on special device for chip groove fluting with variable angle of spiral. Scientific technical journal “Transport and Machinebuilding” #1(23), 2012 year. Publishing house “Transport and Machinebuilding”. Pages 196-205.

EXAMINATION OF ACOUSTIC PROPERTIES OF A GEAR PUMP AFTER TOOTH ROOT UNDERCUTTING USING THE INDUCTION OF DECISION TREES

PhD. , M.Sc. Deptuła A. [1]
Faculty of Production Engineering and Logistics – Opole University of Technology, Opole [1]

a.deptula@po.opole.pl

Abstract: *Among cavity pumps used in hydraulic drive systems as energy generators, gear pumps are the most widespread. Apart from their numerous advantages from the point of view of noisiness and the delivery fluctuation coefficient, they are inferior to others. Steps are undertaken to decrease the noisiness. According to the research results, own acoustic parameters of the pump depend on the technology and performance quality as well as on the geometrical features of the tooth profile. The paper is restricted to the analysis of acoustic properties of an innovative gear unit after tooth root undercutting. Acoustic properties have been described with taking into consideration induction of decision trees and decision rules.*

Keywords: ACOUSTIC PROPERTIES, GEAR PUMP, INDUCTION TREES, OPTIMIZATION

1. Introduction

Hydraulic machines are one of the most widespread machine classes, without which it would be hard to imagine the functioning of modern industry and of society today. These machines can be divided into pumps, water turbines, hydrokinetic drives, mixers, water-jet drives, propellers etc., but also hydraulic transport, hydraulic drive and hydraulic steering, etc. [1-4]. Overflow machines form a wide group of systems. The work of overflow machines is most frequently based on two states: transient state (in which values of the system functions change in time) and steady state (the functions values do not change in time or change periodically). If the pump is the heart of a hydraulic system then the valve is the brain. Valves are used to perform a large variety of governing and controlling functions.

The noise is most effectively reduced through a combination of the two ways (the active way being the most effective of the two). Detailed studies have shown that the noisiness of the displacement pump is due to the flow of the working medium (Fluid Born Noise) and to the vibrations of its structural components (e.g. the unbalance of the rotating parts, excessive clearance in the moving joints, improper workmanship and assembly). The main causes of noise generation, having the most significant bearing on the sound pressure emission level, are the pressure fluctuation on the delivery side and the trapping of the fluid in gear wheel tooth spaces. In order to avoid such adverse phenomena, relief grooves and dampers are used to at least partially reduce the fluctuations generated by the pump (the passive method) [4, 12, 13]. Such measures, however, entail additional costs. The authors' own research has shown that the pump's acoustic parameters depend on the manufacturing technology, the quality of workmanship and the tooth profile geometry. The present study is limited to the analysis of the acoustic properties of a novel gear pump with tooth root relief, in particular with the use of a induction trees.

2. Tested pump

The designed and built prototype pump has a three-plate structure shown schematically in Fig. 1. The front plate (1) is used for mounting the pump on the drive unit. The middle plate (2) contains gear wheels, slide bearing housings and suction and forcing holes for connecting to a hydraulic system. The whole construction is closed with a rear plate.

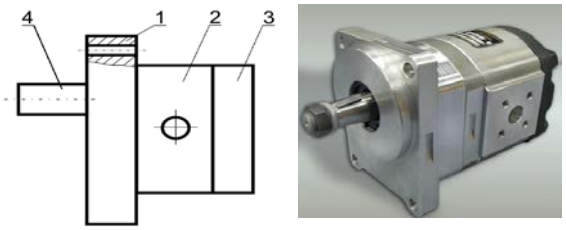


Fig. 1 *Three-plate design of gear micropump with external meshing. 1 – front (mounting) plate, 2 – middle (rest) plate, 3– rear plate, 4– driving shaft*

The tested prototype unit was designed in-house and manufactured by the Hydraulic Pumps Manufacturing Company Ltd. in Wrocław. The pump was designed having in mind the technological capacities of this company [10, 11]. The novelty of the prototype pump consists in the modification of the involute profile in its upper part through the so-called tooth root relief (undercut). The main meshing parameters for the pump with unit delivery q = 40 cm^3 are listed in the table below (Table 1).

Table 1: *Meshing parameters*

	Symbol	Unit	Value
Number of teeth	z	-	9
Modulus	m_0	[mm]	4.5
Pressure angle	α_0	[°]	20
Gear wheel width	b	[mm]	32.2

3. Measuring rig

The reverberation chamber (3) for acoustic testing meets standard ANSI S1.21-1972 and standard PN-85/N-01334 and can be used for the vibration and noise certification of machines and equipment. The chamber's sound insulating power against external noise in a frequency range of 20-20 kHz amounts to 50 dB. This insulating power ensures the elimination of disturbances originating from the drive system and from the hydraulic system supplying the tested pump. Figure 2 shows a schematic of the rig for the testing of acoustic parameters. For measurements the tested pump together with a microphone array was placed in a reverberation chamber.

The chamber is made from two similar irregular polyhedrons, one of which is placed in the other. The walls of the chamber are made of solid brick while its inner plasters are made of cement mortar.

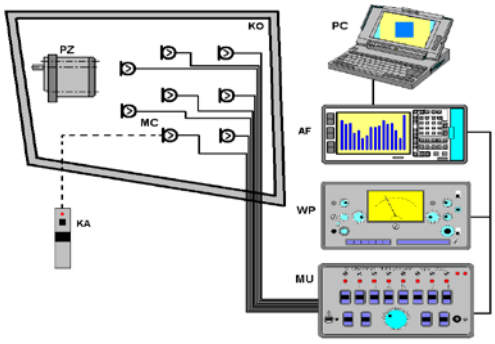


Fig. 2 *Block diagram of gear pump noisiness measuring rig: KA-calibrator, MC-eight free sound field microphones, MU-multiplexer, WP-instrumentation amplifier, AF-two-channel frequency analyzer, PC-computer, PZ-gear pump, KO-chamber*

Reverberation chamber

The chamber is made from two similar irregular polyhedrons, one of which is placed in the other. The walls of the chamber are made of solid brick while its inner plasters are made of cement mortar (Figures 3). Standing waves have been eliminated owing to the different dihedral angles and the concrete plasters. The uniformity of sound field distribution in the chamber is good, being within acceptable limits starting with the octave midband frequency of 125 Hz. Eight constant measuring points have been fixed in the chamber on the basis of sound field distribution studies. In conformance with the above standards, the microphones have been fixed at a height of 1.3 m from the floor.

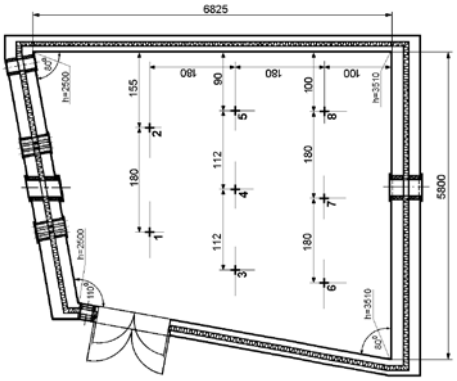


Fig. 3 *Reverberation chamber*

The equipment setup for measuring the noise of the gear pump placed in the diffusion sound chamber is shown in Fig. 4. Measuring microphones were positioned in eight points. The sound pressure level readings taken from them were averaged. For data reading the measuring microphones were selected by means of the multiplexer, and the sound pressure level with the spectrum was stored in the two-channel analyzer memory. The data were edited using a PC and the *B&K* type *5306* software.



Fig. 4 *A gear pump in the acoustic chamber*

4. Acoustic research

Acoustic measurements of an experimental version of the pump respectively for the value of discharge pressure p_t: 0, 2, 4, ..., 30 [MPa] and the frequency f: 25÷20k [Hz] have been obtained in the analysis. Table 2 shows exemplary acoustic measurements of a gear pump after tooth root undercutting for p_t = 12 MP. Figure 5 presents the value of the acoustic pressure level L_m, corrected acoustic pressure level L_A, acoustic power level L_p and corrected acoustic power level L_{pA} in the function of discharge pressure p_t at a constant rotational speed of a pump shaft n = 1500 rpm.

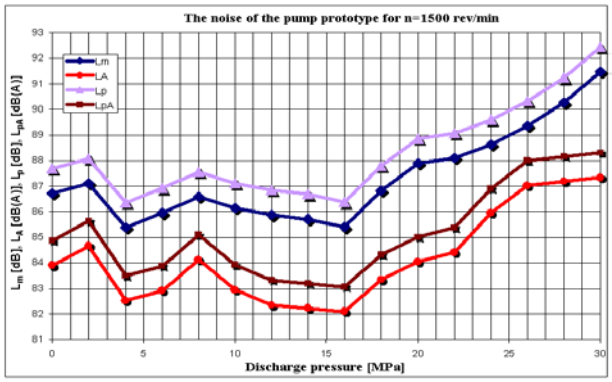


Fig. 5 *The noise of the gear pump after tooth root undercutting for nominal rpm.*

Figures 6 and 7 present a tertian and an octave spectrum of the gear pump after tooth root undercutting for nominal discharge pressure and nominal rotational speed.

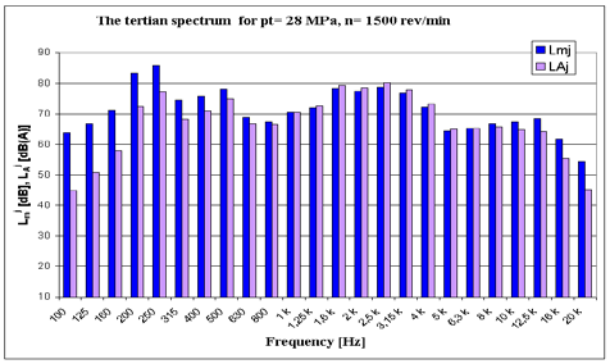


Fig. 6 *The tertian spectrum of an experimental unit for nominal pressure and rotational*

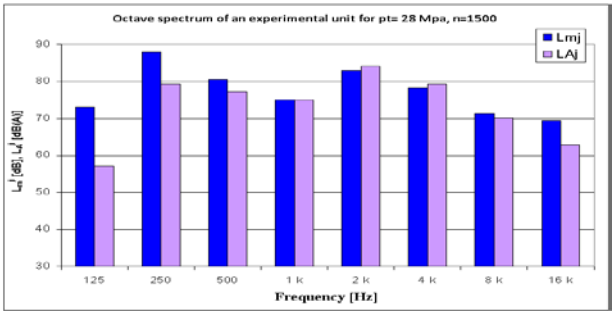


Fig. 7 *The octave spectrum of an experimental unit for nominal pressure and rotational speed*

The dominant level in the whole scope of discharge pressures is present in case of an octave of the centre frequency equal to 2k Hz. Table 2 compares data gathered for an experimental unit and the pump PZ4-32 TKs 186.

Table 2: *Meshing parameters.*

p_t [MPa]	Pump test $L_{A(1)}^{2000}$	PZ4-32 TKs 186 $L_{A(2)}^{2000}$	ΔL_A^{2000}
6	74,7 [dB]	79,5 [dB]	4,8 [dB]
12	74,8 [dB]	79,5 [dB]	4,7 [dB]
18	78,2 [dB]	83,6 [dB]	5,4 [dB]
24	81,0 [dB]	83,0 [dB]	2,0 [dB]
28	82,9 [dB]	83,6 [dB]	0,7 [dB]

Figure 8 compare a corrected level of the acoustic pressure L_A, and the corrected level of the acoustic power L_{pA} of an experimental unit and pump PZ4-32 TKs 186.

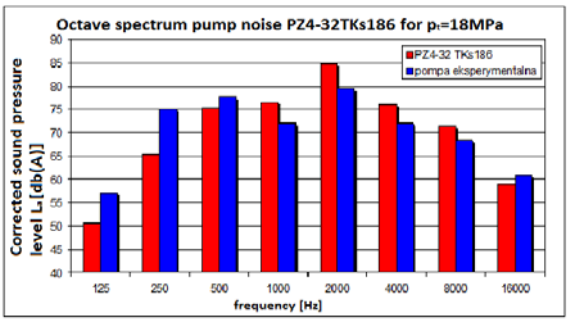


Fig. 8 *The octave spectrum of an experimental unit and pump PZ4-32 TKs 186*

5. Discrete methods of identification and classification of acoustic signal

The classification is an important stage in the analysis of acoustic properties. In this stage, properties characteristic for signals of particular microphones are compared with each other. On the basis of obtained results a decision concerning the classification of the signal properties to a given group is made [5] Among the most often applied methods of recognising acoustic signals are: HMM (Hidden Markov Models) , VQ (Vector Quantization), LVQ (Learning Vector Quantization), SOM (Self- Organising Maps), ANN (Artificial Neural Network), GMM (Gaussiab Mixture Models) [14, 16], SVM (Support Vector Machines). In addition, there are classifiers based on the induction of decision trees, ML-HMM (Maximum Likelihood Hidden Markov Model) [6, 7, 8]. In a general case, the classification includes two stages: creating of patterns for recognition and identification.

Tree induction as classifiers of acoustic signals

A decision tree is a structure which has ordinary properties of trees in the meaning assigned to the tree in the information technology, so it is a structure composed of nodes from which branches come to other nodes or leaves. It is convenient to define tree structures in a recursive way. Assuming that a given branch X on which attributes a_1, a_2 ,..., a_n and the set of notions C of the category C are determined:

1. The leaf containing any category label $d \in C$ is a decision tree.

2. If t: $X \rightarrow R_t$ is a test made on the values of attributes of examples with a set of possible results R_t= { r_1, r_2, ... r_m } are decision trees, then the node containing the test t , from which m branches come out, given that for i== 1, 2, ..., m branch i corresponds to the result r_i and leads to the tree T_i, is a decision tree.

For any node of n decision tree, by t_n we mean a test connected with it, and for each of its possible results $r \in R_t$ by $n_{[r]}$ node or child leaf, to which the n branch related to the r result leads from the node. The notation described above is presented in Figure 9.

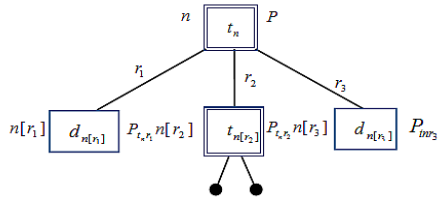


Fig. 9 *A sample query "query-by-example" to the decision-making system*

Information included in the set of training examples is equal to:

$$I(E) = -\sum_{i=1}^{|E|} \frac{|E_i|}{|E|} \cdot \log_2 \left(\frac{|E_i|}{|E|} \right)$$

where:

E - the set of training examples

$|E_i|$ - the number of examples which describe i object

$|E|$ - the number of examples in the training set E

The expected value of information after the division of the set of examples E into subsets $E^{(m)}, m = 1, ..., |V_a|$, for which the attribute a has the value V_m, determined as [15]:

$$I(E,a) = \sum_{m=1,K,|V_a|, E^{(m)} \neq \emptyset} \frac{|E^{(m)}|}{|E|} \cdot I\left(E^{(m)}\right)$$

where:

$|E^{(m)}|$ - the number of examples after the division of the set E in relation to the value m of a given attribute,

$|E|$ - the number of examples in the training set E.

Figure 10 presents preliminary signals processing without a filter for 8 microphones in the whole range of values of discharge pressure that is 2-30 MPa.

a) b)

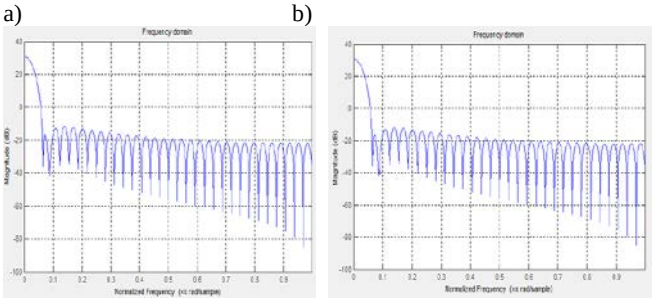


Fig. 10 *Initial processing of the signals for the four microphones: a)1. b)3*

A method of analysing a frequency spectrum has been chosen as a parametrisation method. The method using this rule is called the Burg method, the implementation of which is included among others in the range "Signal Processing Toolbox" of the Matlab programme [9]. The figure 11 shows the spectrogram for 2 microphones.

a) b)

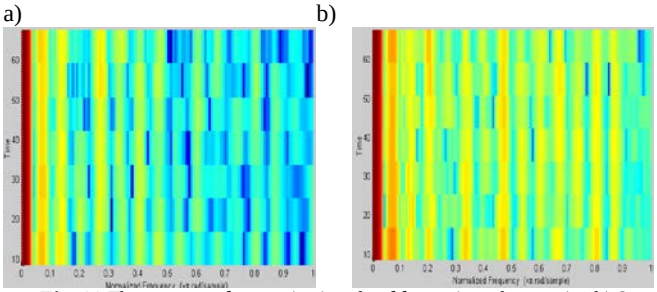


Fig. 11 *The spectra of acoustic signals of four microphones a) 1 b) 8*

The classification by means of induction trees has been made separately for acoustic pressure L_m, frequency *kHz* and discharge pressure *MPa*, as output attributes (wy): L_m(wy), *kHz* (wy), *MPa* (wy). Input attributes (we) are the values of acoustic measurements registered from 8 microphones: microphones**1**(we), microphones**2**(we), microphones**3**(we), microphones**4**(we), microphones**4**(we), microphones**5**(we), microphones**6**(we), microphones**7**(we), microphones**8**(we). As a result of the analysis, induction trees have been generated for each parameter L_{mj}, p_t [Mpa], f [Hz].

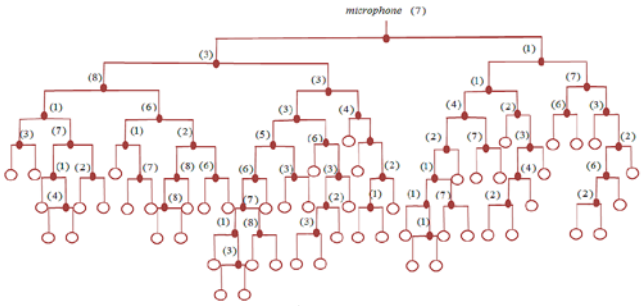


Fig. 12 *The induction tree for the acoustic pressure L_m – without trimming*

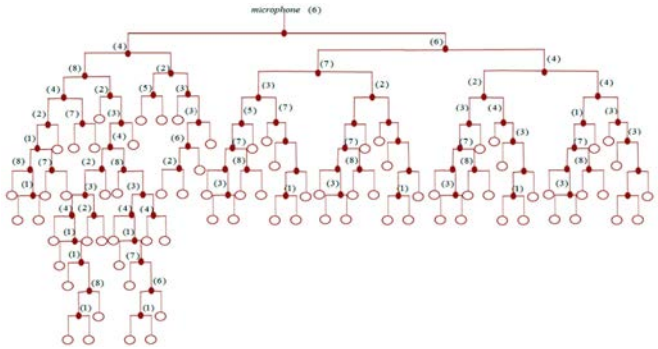


Fig. 13 *A simplified induction tree for the frequency f [Hz]- the number of examples forming the tree graph- 4, tree trimming- 40%*

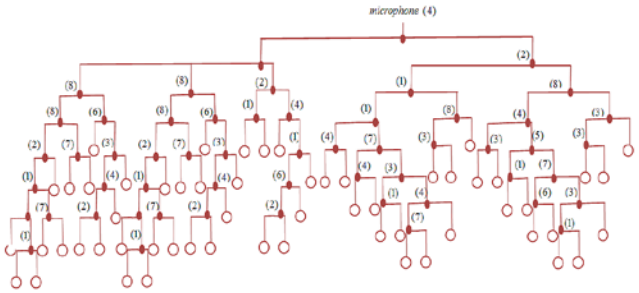


Fig. 14 *A simplified induction tree for the discharge pressure p_t [Mpa]- the number of examples forming the tree graph-4, tree trimming-25%*

The induction tree determines the degree of importance of the attribute from the most important one placed in the root, through classification of any example. The most important acoustic signal generated by the value of the discharge pressure is present in the microphone 4- in accordance with the tree from Figure 14 whilst the most important acoustic signal influenced by the change of frequency is generated on the microphone 6- in accordance with the tree from Figure 13. In accordance with the tree from Figure 12, the most important signal influencing the value of the acoustic pressure is the signal registered on the microphone 7.

6. Conclusions

In a decision tree, nodes store tests checking values of example attributes and leaves store categories assigned to them. For each of possible test results, there is one branch coming from a node to a subtree. In this way, it is possible to represent any attributes of the hypothesis admissible for a given set. All operations were made in the real time during normal exploitation of the gear pump. On the basis of the results received from the inference mechanism, resulting from the correlation between acoustic signals measured in a continuous manner and model signals placed in the data base, there would be identification of the influence of particular signals from microphones on the chosen parameters of the gear pump after tooth undercutting

7. Bibliography

[1] Barelli L., Bidini G., Buratti C., Mariani R.: *Diagnosis of internal combustion engine through vibration and acoustic pressure non-intrusive measurements*, Applied Thermal Engineering 29, 1707–1713, 2009.

[2] Carlucci A.P., Chiara F.F., Laforgia D.: *Analysis of the relation between injection parameter variation and block vibration of an internal combustion diesel engine*, Journal of Sound and Vibration, 295, 141–164, 2006

[3] Collective work, Techbook - OBD II & Electronic Engine Management Systems, Haynes, 2005.

[4] Deptuła A.: *Application of multi-valued weighting logical functions in the analysis of a degree of importance of construction parameters on the example of hydraulic valves*, International Journal of Applied Mechanics and Engineering, vol.19, No.3, University Press Zielona Góra, pp. 539-548, ISSN 1425-16554, 2014.

[5] Deptuła A., Osiński P., Radziwanowska U.: *Decision support system for identifying technical condition of combustion engine*, Archives of Acoustics, Vol. 41, No 3, 2016 [in print]

[6] Deptuła A., Partyka M. A.: *Decision optimization of machine sets with taking into consideration logical tree minimization of design guidelines*. International Journal of Applied Mechanics and Engineering, vol.19, No.3, University Press Zielona Góra, pp. 549-561 ISSN 1425-16554, 2014.

[7] Kirpluk M.: *Fundamentals of acoustics (in Polish)*, Wyd. NTL-M, Warszawa, 2012.

[8] Learner, in IEEE Transactions on Evolutionary Computation, vol. 9, no.1, Feb. 2005, pp. 31–43.

[9] Luft S.: *Basics of Engines Construction (in Polish)*, Wyd. WKŁ, Warszawa, 2010.

[10] Osiński P., Deptuła A. Partyka M. A. : *Discrete optimization of a gear pump after tooth root undercutting by means of multi-valued logic trees*, Archives of Civil and Mechanical Engineering, vol. 13, nr 4, pp. 422-431, 2013.

[11] Osiński P., Kollek W.: *Assessment of energetistic measuring techniques and their application to diagnosis of acoustic condition of hydraulic machinery and equipment*, Archives of Civil and Mechanical Engineering. 2013.

[12] Wu J.D., Chen J.Ch.: *Continuous wavelet transform technique for fault signal diagnosis of internal combustion engines*, NDT&E International 39, 304–311, 2006

[13] Wu J.D., Kuo J.M.: *An automotive generator fault diagnosis system using discrete wavelet transform and artificial neural network*, Expert Systems with Applications, No. 36, pp. 9776-9783, 2009.

[14] Wu J.D., Kuo J.M.: *An expert system for fault diagnosis in internal combustion engines using wavelet packet transform and neural network*, Expert Systems with Applications, No. 36, pp.4278-4286, 2009.

[15] Quinlan J. R.: *Induction of Decision Trees*, Machine Learning, 1, pp. 81-10, 1986

[16] Xuo L., Jelinek F.: *Probabilistic classification of HMM states for large vocabulary*, [in:] Proceedings of ICASSP, 2044–2047, Phoenix, USA, 1999.

ON A PHYSICO-MATHEMATICAL MODEL FOR CONTROLLED FORMATION OF PERIODIC NANOSTRUCTURES AT SOLID SURFACES IRRADIATED BY FEMTOSECOND LASER PULSES

Prof. Dr.Sc.Math. Guseynov Sh.E.[1, 2], B.Sc.Phys. Žaimis U.[1]
Faculty of Science and Engineering, University of Liepaja, Liepaja, Latvia [1]
"Entelgine" Research & Advisory Co., Ltd., Riga, Latvia [2]

sh.e.guseinov@inbox.lv, uldiss.z@inbox.lv

Abstract: *In this paper, we propose a physico- mathematical 3D model to study some of the basic features of the interaction of radiation with solid materials (metals, semiconductors , insulators) under the action of femtosecond laser pulses. The constructed model is a parametric model that, in particular, takes into account the dependence of the physical and chemical characteristics of the periodic nano-surface structures controlled laser irradiation parameters the polarization, angle of incidence, the energy density, wavelength, etc. The developed model is meant for the excitation of periodic nano-surface structures by electric waves which are in the process of irradiation and periodically amplified and attenuated, i.e. it holds periodic interference.*

Keywords: PERIODIC NANOSTRUCTURE, LASER PULSE, MATHEMATICAL MODEL, STABLE SOLUTION

1. Introduction

The synthesis of periodic nanostructures on various solid surfaces together with femtosecond laser impulses is one of the most perspective methods in the field of laser ablation on the metal surfaces, metal-like materials and dielectrics. In particular, the use of femtosecond lasers has several advantages. First of all, the effect of these impulses on the target leads to ultra-fast heating, which then reaches a very high quality of material processing. Second of all, the next two very crucial aspects provide unique conditions for the ablation of material together with the femtosecond laser impulses (see, for instance, [1]-[3]). Now it is vital to observe that the amount of time it takes after the laser impulse from the heated zone is negligible so that the laser energy is absorbed in the targeted and localized area that can be controlled.

Currently the laser synthesis of periodic nano-surface structures is successfully applied in increasing the ultra-thin materials that are often used in the microelectronics and aerospace materials, for colour coding, for local chemical modification of surfaces, to excite Raman light scattering, and to improve the strength of ultra-thin materials (see, for instance, [4], [5] and the corresponding references therein). Nevertheless, there are no adequate complex physical and mathematical models that are based on rigorous theoretical calculations; no strictly mathematically based concept can make accurate predictions in the evolution of both the geometry and characteristics of the synthesized periodic nano-surface structures on surfaces of various metals and metal-like materials under the influence of femtosecond laser impulses with different physical and technological conditions.

For an accurate description of the mechanism of synthesis of periodic nanostructures on the surface of semiconductors by the femtosecond laser impulses, there appears different approaches that mostly use the same method of studying the analysis of various surface instabilities. Notice that such analysis is not able to fully identify the particular nano-surface periodic structures (see, for instance, [6], [7]), as the absorption of the femtosecond pulse geometry of the surface of the material hardly changes. Thus, this is considered as a problem of the non-uniform distribution of the laser energy on the treated nano-surfaces; optical properties are instantly changed in the course of photoexcitation and the melting of the electronic subsystem.

Simultaneously, the developed methods for solving this problem apply only to a perfectly flat or rough surface with very low relief modulation amplitude ([9], [8]). In particular, when the ratio between the relief modulation and the laser wavelength is negligible, and in both cases, the following restrictions apply: the number of laser impulses must not exceed 10 and the periodic values of the nano-surface structures should be in the range 1÷1.1 (see, for instance, [9], [10]).

The authors of this work have built from scratch 1D-3D mathematical models for the study of some of the main features of the interaction of radiation with solid materials (taking as an example copper) under the action of femtosecond laser pulses. The models follow the parametric model, which incorporates the dependence of physical and chemical characteristics of the periodic nano-surface structures (periodic nanoscale particles) from the controlled parameters of laser ablation: from polarization, the angle of incidence, the energy density, of the wave length, etc. All the new models are expressed in the form of linear and non-linear non-stationary partial differential equations with linear and nonlinear boundary conditions of mixed type (the Neumann-type and Newton-Robin type).

Furthermore, the authors of this paper developed an analytical and numerical algorithm for finding stable solutions in 1D approximation for constructed 3D model. However, due to restrictions on the presented volume of this work, we will skip the output constructed 1D-3D physical and mathematical models and give only the setting of the "ready-made" 3D model. Therefore, we will present the developed analytical and numerical algorithm.

2. Mathematical Models

3D model for temperature distribution and electric field in metallic materials

The proposed 3D mathematical model consists of determining the temperature distribution $T = T(x,t)$ and the electric field $\vec{E} = \vec{E}(x,t)$ in the region $\overline{D} \overset{def}{\equiv} \left\{ x = (x_1, x_2, x_3) \in \mathbb{R}^3 : x_i \in [0, L_i],\ i = \overline{1,3} \right\}$ during any moment of time $t \in [0, t_{\max}]$ with the following equations as well as the initial and boundary conditions:

- dual-temperature heating dynamics for electron $\left(T^e(x,t)\right)$ and lattice $\left(T^\ell(x,t)\right)$ subsystem of metal materials (taking as an example copper) with femtosecond laser pulse:

$$\left[c_V \cdot \frac{\partial T}{\partial t} \right]^{e,\ell} + \tau \cdot \left[\frac{\partial^2 T}{\partial t^2} \right]^{e,\ell} = div\left(\chi_V^e \left(x,t;T^e,T^\ell \right) \cdot \nabla T^e \right) + \quad (1)$$
$$+ F\left(x,t;T^s \right),\ (x,t) \in D \times [0, t_{\max}];$$

- electric field distribution on the periodically structured surface of the metallic material:

$$\frac{4\cdot\pi\cdot\sigma\cdot\mu}{c^2}\cdot\frac{\partial\vec{E}}{\partial t}+\frac{\varepsilon\cdot\mu}{c^2}\cdot\frac{\partial^2\vec{E}}{\partial t^2}=\Delta_{x_j,x_k}E_{x_i}-\sigma\cdot\left|\vec{E}\right|^2-$$

$$-\frac{\partial}{\partial x_i}\left(\frac{\partial E_{x_j}}{\partial x_j}-\frac{\partial E_{x_k}}{\partial x_k}\right),(x,t)\in D\times[0,t_{\max}], \tag{2}$$

$$\forall(i,j,k)=\overline{1,3}: j\neq k\neq i;$$

- the following initial conditions:

$$T^e(x,t)\big|_{t=0+0}=T_s^e(x), x\in\overline{D}, \tag{3}$$

$$\left.\frac{\partial T^e(x,t)}{\partial t}\right|_{t=0+0}=0, x\in\overline{D}, \tag{4}$$

$$T^\ell(x,t)\big|_{t=0+0}=T_s^\ell(x), x\in\overline{D}, \tag{5}$$

$$\left.\frac{\partial T^\ell(x,t)}{\partial t}\right|_{t=0+0}=0, x\in\overline{D}, \tag{6}$$

$$\vec{E}(x,t)\big|_{t=0+0}=\vec{E}_0(x), x\in\overline{D}; \tag{7}$$

$$\left.\frac{\partial\vec{E}(x,t)}{\partial t}\right|_{t=0+0}=0, x\in\overline{D}; \tag{8}$$

- and the following boundary conditions:

$$\left.\left\{T^e(x,t)-k_1\cdot\frac{\partial T^e(x,t)}{\partial x_i}\right\}\right|_{x_i=0+0}=T_{0,i}^e\left(x/\{x_i\},t\right), \tag{9}$$

$$x\in\overline{D},\ t\in[0,t_{\max}],\forall i=\overline{1,3};$$

$$\left.\left\{T^\ell(x,t)-k_2\cdot\frac{\partial T^\ell(x,t)}{\partial x_i}\right\}\right|_{x_i=0+0}=T_{0,i}^\ell\left(x/\{x_i\},t\right), \tag{10}$$

$$x\in\overline{D},\ t\in[0,t_{\max}],\forall i=\overline{1,3};$$

$$\left.\frac{\partial T^e(x,t)}{\partial x_i}\right|_{x_i=L_i-0}=T_{L,i}^e\left(x/\{x_i\},t\right), \tag{11}$$

$$x\in\overline{D},\ t\in[0,t_{\max}],\forall i=\overline{1,3};$$

$$\left.\frac{\partial T^\ell(x,t)}{\partial x_i}\right|_{x_i=L_i-0}=T_{L,i}^\ell\left(x/\{x_i\},t\right), \tag{12}$$

$$x\in\overline{D},\ t\in[0,t_{\max}],\forall i=\overline{1,3};$$

$$\vec{E}(x,t)\big|_{x_i=0+0}=\vec{E}_{0,i}\left(x/\{x_i\},t\right), \tag{13}$$

$$x\in\overline{D},\ t\in[0,t_{\max}],\forall i=\overline{1,3};$$

$$\vec{E}(x,t)\big|_{x_i=L_i-0}=\vec{E}_{L,i}\left(x/\{x_i\},t\right), \tag{14}$$

$$x\in\overline{D},\ t\in[0,t_{\max}],\forall i=\overline{1,3}.$$

Furthermore, we assume compliance with the relevant consistency conditions of the initial and boundary conditions.

In the formulated problem (1)-(14) the following definitions and designations occur:

- $[A]^{e,\ell}\overset{def}{\equiv}A^e-A^\ell$;
- $divA\overset{def}{\equiv}\sum_{i=1}^{3}\frac{\partial A_{x_i}}{\partial x_i}$;
- $\nabla A\overset{def}{\equiv}\left(\frac{\partial A}{\partial x_1},\frac{\partial A}{\partial x_2},\frac{\partial A}{\partial x_3}\right)^T$;
- D denotes the interior field $\overline{D}$, i.e. $D\overset{def}{\equiv}\mathrm{int}\left(\overline{D}\right)=\left\{x=(x_1,x_2,x_3)\in\mathbb{R}^3:\ x_i\in(0,L_i),\ i=\overline{1,3}\right\}$;
- c_V^e and c_V^ℓ are respectively the electron gas and heat capacities per unit volume V;
- $\tau\ \square\ 1$ and $k_i\ (i=1,2)$ are positive constants;
- the function $\chi_V^e\left(x,t;T^e,T^\ell\right)$ describes the electron thermal conductivity, which plays a pivotal role in the metals, semimetals, as well as certain semiconductors and superconductors. The electron thermal conductivity provides information on the carrier scattering mechanism, on the peculiarities of the band structure of the material, as well as information about the magnitude and temperature dependence of the bandgap (energy gap) of the material. It is important to note that the electron conductivity at low temperatures is determined by the scattering of electrons by impurities and defects and also increases with temperature. However, at high temperatures the process is determined by scattering on phonons and decreases with increasing temperature and therefore, at a certain temperature the electron thermal conductivity reaches a maximum, higher than that of a perfect crystal. The conductors in electron thermal conductivity are related to the conductivity of the Wiedemann-Franz Law; in superconductors electrons are combined into Cooper pairs, not involving in the transfer of heat. Furthermore, when the temperature falls below the transition temperature to the superconducting state, the electron thermal conductivity is determined by the normal (unpaired) electrons and decreases exponentially as it approaches zero. In bipolar semiconductors and semimetals, there is an additional mechanism called a bipolar component, namely, electron-hole pairs generated at the hot end of the target and diffusing towards the temperature gradient and recombining at the cold end to produce heat;
- the function $F\left(x,t;T^s\right)$, calculated by the Beer-Lambert-Bouguer Law:

$$F\left(x,t;T^s\right)\overset{def}{\equiv}\left(1-\Phi\left(T^s\right)\right)\cdot I\cdot e^{-\sum_{i=1}^{3}\beta_i\cdot x_i}\times \tag{15}$$

$$\times e^{-\delta\left(t-t^{\text{laser pulse}}\right)\cdot\int_D\gamma(x,t)dV_x},\ \forall t^{\text{laser pulse}}\in\left[0,t_{\max}^{\text{laser pulse}}\right]$$

describes the attenuation/absorption of laser radiation on the feeding surface of the target "flow" of free electrons due to the inverse scattering brake; in Equation (15) the function Φ, depending on the temperature T^s, the surface of the metal material at the initial moment of time, is the reflectance of the target material; I denotes the intensity of the incident laser beam on the target; $\beta_i\ \left(i=\overline{1,3}\right)$ is the absorption coefficient of the target material in the direction of the coordinate axis $\overline{OX}_i$; $\delta(\cdot)$ is the Dirac Delta Function; the function $\gamma(x,t)$ is the coefficient absorption in the resulting plasma laser flare; $t_{\max}^{\text{laser pulse}}\ \square\ t_{\max}$ denotes the end of the laser radiation;

- the scalar function $E_{x_i}(x,t)$ is the i-th $\left(i=\overline{1,3}\right)$ component (corresponding axis $\overrightarrow{OX_i}$) of the electric vector field $\vec{E}(x,t)$;
- ε and μ mean respectively dielectric and magnetic permeability of the metal material (in our situation copper);
- σ is a specific conductivity of the material;
- c is the speed of light. Here it should be noted that for the simulation of the femtosecond laser radiation, the nested (embedded) laser energy distribution may exclude relief modulation over time $t_{\max}^{\text{laser pulse}}$, however, it is crucial to consider that in the photoexcitation process, the copper surface for heating ultrafast electronic subsystem of the material to the temperature T^e of the order of several electron volts, can significantly affect the optical properties of copper. It is easy to show at a specific wavelength (for example, $\lambda = 700$ nm) the femtosecond laser pulse by calculating the dependence $\mathrm{Re}(\varepsilon)$ and $\mathrm{Im}(\varepsilon)$ to T^e; consequently from the Drude Model considering the contribution of the lattice ε^{ℓ} we can apply the following formula to determine the dielectric constant ε:

$$\varepsilon = \varepsilon^{\ell} - \frac{\omega_{\text{plasma}} \cdot t^2_{\text{electron collision}}}{\left(\omega \cdot t_{\text{electron collision}}\right)^2 + 1} \cdot \frac{i \cdot \omega \cdot t_{\text{electron collision}} + 1}{i \cdot \omega \cdot t_{\text{electron collision}}}, \qquad (16)$$

where ω is the frequency of the femtosecond laser pulses;

$$\omega_{\text{plasma}} = \sqrt{\frac{\rho_{\text{electron density}} \cdot e^2}{\varepsilon_0 \cdot m_{\text{effective mass}}}} \qquad (17)$$

has a plasma frequency when the effective mass of the electron $m_{\text{effective mass}} \approx \frac{3}{2} \cdot m$ and the electron density $\rho_{\text{electron density}}$ for copper;

- $t_{\text{electron collision}}$ is a collision of electrons within the random phase approximation (see, for instance, [11]), and it is determined by the following formula:

$$t_{\text{electron collision}} = t_{\text{electron collision}}\left(T^e\right) \approx \frac{1}{K_{\text{electron-electron scattering}}} \times \times \frac{1 + e^{-\frac{\hbar \cdot \omega}{T^e}}}{\left(\pi \cdot T^e\right)^2 + \left(\hbar \cdot \omega\right)^2}, \qquad (18)$$

with respect to $K_{\text{electron-electron scattering}}$, which for the investigation of the material (in our situation copper) can be determined by tabular dependence approximation $\varepsilon(\omega)$ at $T^e = 0$.

Thus, under certain assumptions the foregoing non-linear 3D model (1)-(18) describes the evolution of the temperature field and the electric field distribution on the surface of metals (taking as an example copper) under the action (irradiation) of femtosecond laser pulses. Since dielectrics with a forbidden gap in the beginning of laser radiation's exposure there is no absorption of the radiation pulse due to reverse brake dissipation; hence, most dielectrics with relative moderate intensities of laser radiation can be considered as transparent. It is important to observe that the mechanism of interaction of femtosecond laser pulses with insulators is significantly different from the above-described mechanism for metals.

When the threshold of intensity, depending on the characteristics of the particular dielectric surface structure, begins to break down, the changing of the reflectance and absorbance of the surface is followed by the melting and ablation of the dielectrics (with a further increase in the intensity of radiation).

Following the outline of monograph [1] below, the main process leading to the synthesis of nano-sized particles is the influence of femtosecond laser pulses in the dielectric materials. At the initial stage of the action of a femtosecond laser pulse on a dielectric surface (we neglect the presence of impurities and defects in the original) the multiphoton absorption mechanism forms a free primeval / seeding electrons, and these electrons efficiently absorb laser energy by dissipating the reverse braking process, with energy E^e beginning to increase rapidly and reaching the critical value, while developing process of ionization by electron impact (the so-called avalanche / cumulative ionization). For laser pulse durations of the order of hundreds of femtoseconds with a capacity in the range of $10^{10} \div 10^{14}$ W/cm^2, the tunnel ionization mechanism can be neglected. Then the dynamics of the electron density in the conduction band can be described by the following simplified equations:

$$\begin{cases} \dfrac{\partial \rho^e}{\partial t} = \left(\vartheta^{\text{m.i.}}\right)^n \cdot I^n(t) + \vartheta^{\text{c.i.}} \cdot I(t) \cdot \rho^h; \\ \dfrac{\partial \rho^h}{\partial t} = \left(\vartheta^{\text{m.i.}}\right)^n \cdot I^n(t) + \vartheta^{\text{c.i.}} \cdot I(t) \cdot \rho^h, \end{cases} \qquad (19)$$

where the superscripts e and h refer, respectively, to the electrons and the holes; $\vartheta^{\text{m.i.}}$ and $\vartheta^{\text{c.i.}}$ mean respectively multiphoton ionization rates (multiphoton ionization) and avalanche ionization (cumulative ionization); $I(t)$ indicates the intensity of the radiation incident on the target; and n is the number of photons required for the excitation of electrons at the transition from the valence band to the conduction band.

The appearance of a large number of electrons in the conduction band of the dielectric leads to metallization of the dielectric surface layer. Therefore, it increases the absorption and reflection coefficients. However, unlike the metals, the density of electrons in the conduction band of dielectrics depends strongly on the time and distance target depth. Furthermore, it is possible to describe the electron- lattice relaxation dielectric process, by analogy with the description of metals. In addition, at the end of femtosecond laser pulses, with the passage of time, there are processes of recombination of electrons and three-body recombination (Auger recombination / three-body recombination), from which there is a gradual return of the target dielectric properties. Typically, after the irradiation in the process of recombination of electrons are formed various defective state whose lifetime depending on the type of the dielectric ranges from microseconds to days. Repeated action of femtosecond laser pulses lead to a more efficient heating by priority field defects with larger absorption cross section compared with the electrons of the valence band.

1D model for metallic materials

In conclusion, this paper presents the basic equations in 1D approximation describing the mechanism of action of femtosecond laser pulses in the dielectric materials based on photoemission and electric fields.

- The first equation is a modification (towards complexity – a detailed description) of the simple equations (19):

$$\frac{\partial \rho^e}{\partial t} = \theta \cdot \frac{\partial^2 \rho^e}{\partial x^2} + \mu \cdot E \cdot \frac{\partial \rho^e}{\partial x} + \frac{\mu}{\varepsilon \cdot \varepsilon_0} \cdot \rho^e \cdot [\rho]^{e,h} + + \left(\vartheta^{m.i.} + V^{c.i.}\right) \cdot \frac{\rho^{n.a.}}{\rho^{n.a.} + \rho^h} - \vartheta^{e.r.} - F^{ph.e.}; \qquad (20)$$

- The Poisson's equation:

$$\frac{\partial \vec{E}}{\partial x} = -\frac{|e|}{\varepsilon \cdot \varepsilon_0} \cdot [\rho]^{e,h}; \qquad (21)$$

- The following is a formula for calculating the intensity of femtosecond laser radiation onto a target Gaussian time profile:

$$I(t)=\sqrt{\frac{\ln 2}{\pi}}\cdot\left(1-\Phi(t)\right)\cdot\frac{2\cdot f}{t_I}\cdot e^{-4\cdot\ln 2\cdot\left(\frac{t}{t_I}\right)^2}; \quad (22)$$

- The radiation intensity equation inside the dielectric depending on the time and distance of the target depth considering the multi-photon absorption and absorption by free electrons:

$$\frac{\partial I(x,t)}{\partial x}+a(x,t)\cdot I(x,t)=-\vartheta^{m.i.}\cdot\frac{\rho^{n.a.}\cdot m\cdot\hbar\cdot\mu}{\rho^{n.a.}+\rho^{h}}; \quad (23)$$

- The following formula calculates the absorption coefficient of a free electron:

$$a(x,t)=\frac{4\cdot\pi\cdot k(x,t)}{\lambda}; \quad (24)$$

- The Fresnel's formula for the estimation of the reflection coefficient:

$$\Phi(t)=\frac{\left(\sqrt{\frac{\mathrm{Re}(\varepsilon)+\sqrt{\left(\mathrm{Re}(\varepsilon)\right)^2+\left(\mathrm{Im}(\varepsilon)\right)^2}}{2}}-1\right)^2+k^2}{\left(\sqrt{\frac{\mathrm{Re}(\varepsilon)+\sqrt{\left(\mathrm{Re}(\varepsilon)\right)^2+\left(\mathrm{Im}(\varepsilon)\right)^2}}{2}}+1\right)^2+k^2}; \quad (25)$$

- The Einstein's formula for the diffusion coefficient:

$$\theta=\frac{k\cdot T^{e}\cdot\mu}{|e|}; \quad (26)$$

- Formula estimation for the photoemission:

$$F^{ph.e.}=\frac{\left(\vartheta^{m.i.}\right)^n\cdot I^n+\vartheta^{c.i.}\cdot\rho^{e}\cdot I}{2}\cdot\frac{\rho^{n.a.}\cdot e^{-\frac{x}{\xi}}}{\rho^{n.a.}+\rho^{h}}. \quad (27)$$

In the equations (20)-(27) there are the following designations (the designations that occurred earlier below are not listed):

- $V^{m.i.}=\vartheta^{m.i.}\cdot I\cdot\rho^{e}$ the acceleration/development of cumulative ionization;
- $\vartheta^{e.r.}=\frac{\rho^{e}}{\tau_r}$ the recombination velocity electron capture of the coupled state;
- $\rho^{n.a.}$ the neutral atoms;
- $\xi\approx 1\text{nm}$ the characteristic depth of the target, which photoemission depth (maximum photoemission takes place on the surface of the dielectric material) decreases exponentially.

3. Conclusions

In the present paper, 3D model (1)-(18) as well as 1D model (only main equations without any initial or boundary conditions) (20)-(27) are proposed. The model (1)-(18) describes evolution of temperature field (scalar quantity) and electric field (vector quantity) in the case when femtosecond laser pulses act on the metallic materials; the model (20)-(27) contains the basic equations describing the simplified mechanism of action of femtosecond laser pulses on the dielectric materials.

In the future, the authors of this paper intend to: firstly, to develop an algorithm for finding a stable solution of the constructed 3D model (1)-(18); secondly, to complicate the model (1)-(18) by adding other equations and conditions (which were not considered in this model) that can be occurred in the mechanism of femtosecond laser pulses action on the metallic materials; thirdly, to analytically solve the proposed 1D model and to carry out the deeply analyse of the obtained results.

4. Acknowledgements

For the first author the present article was executed within the framework of the State Research Programme *"Next generation Information and Communication Technologies (NexIT)"*, Project No. 4.

References

[1] Bäuerle D. Laser processing and Chemistry. – Berlin, Heidelberg: Springer-Verlag, 2000, 649 p.

[2] Korte F., S. Nolte, B.N. Chichkov, T. Bauer, G. Kamlage, T. Wagner, C. Fallnich, H. Welling. Far-field and near-field material processing with femtosecond laser pulses. – Journal of Applied Physics A, Volume 69, Issue 1 Supplemen, 1999, pp. 7-11.

[3] Wellershoff S.-S., J. Hohlfeld, J. Güdde, E. Matthias. The role of electron-phonon coupling in femtosecond laser damage of metals. – Journal of Applied Physics A, Volume 69, Issue 1 Supplemen, 1999, pp. 99-107.

[4] Dusser B., Z. Sagan, H. Soder, N. Faure, J.P. Colombier, M. Jourlin, E. Audouard. Controlled nanostructrures formation by ultra-fast laser pulses for color marking. – Journal of Optics Express, Volume 18, Issue 3, 2010, pp. 2913-2924.

[5] Ionin A.A., Y.M. Klimachev, A.Y. Kozlov, S.I. Kudryashov, A.E.Ligachev, S.V.Makarov, L.V.Seleznev, D.V. Sinitsyn, A.A. Rudenko, R.A. Khmelnitsky. Direct femtosecond laser fabrication of antireflective layer on GaAs surface. – Journal of Applied Physics B, Volume 111, Issue 3, 2013, pp. 419-423.

[6] Reif J., O. Varlamova, S. Uhlig, S. Varlamov, M. Bestehorn. On the physics of self-organized nanostructure formation upon femtosecond laser ablation. – Journal of Applied Physics A, Volume 117, Issue 1, 2014, pp. 179-184.

[7] Gurevich E.L. Self-organized nanopatterns in thin layers of superheated liquid metals. – Journal of Physical Review E, Volume 83, Issue 3, 2011, pp. 031604_1-031604_5.

[8] Sipe J.E., J.F. Young, J.S. Preston, H.M. van Driel. Laser-induced periodic surface structure. I: Theory. – Journal of Physical Review B, Volume 27, Number 2, 1983, pp. 1141-1154.

[9] Bonse J., A. Rosenfeld, J. Krüger. On the role of surface plasmon polaritons in the formation of laser-induced periodic surface structures upon irradiation of silicon by femtosecond-laser pulses. – Journal of Applied Physics, Volume 106, Issue 10, 2009, pp. 104910_1-104910_5

[10] Ionin A.A., S.I. Kudryashov, S.V. Makarov, L.V. Seleznev, D.V. Sinitsyn, E.V. Golosov, O.A. Golosova, Yu.R. Kolobov, A.E. Ligachev. Femtosecond laser color marking of metal and semiconductor surfaces. – Journal of Applied Physics A, Volume 107, Issue 2, 2012, pp. 301-305.

[11] Groeneveld R.H.M., R. Sprik, A. Lagendijk. Femtosecond spectroscopy of electron-electron and electron-phonon energy relaxation in Ag and Au. – Journal of Physical Review B, Volume 51, Number 17, 1995, pp. 11433-11445.

ALTERNATIVE FUELS FOR DIESEL ENGINES AND THEIR IMPACT ON ENGINE EMISSIONS. A LITERATURE REVIEW

Zbarcea O. PhD student, Prof. Scarpete D.
"Dunarea de Jos" University of Galati, Romania

dan.scarpete@ugal.ro

Abstract: *Today, there is a significant interest in alternative energy sources for vehicles, as a result of continuous concern for the environmental impact and for consumption of the primary energy sources, which are limited. Diesel engines present particularly significant emission like nitrogen oxides, particulate matter, hydrocarbons and black smoke. This paper present a literature review on some alternative fuels for diesel engines, as pure plant oil, biodiesel and compressed natural gas, and their impact on diesel engine emissions.*

Keywords: DIESEL ENGINE, PURE PLANT OIL, BIODIESEL, CNG, EMISSIONS

1. Introduction

Compression ignition (CI) engines are the most popular prime-movers for transportation sector as well as for stationary applications [1]. Global increasing demands for energy, declining fossil fuel reserves, environmental concerns, and rising prices have resulted in a growing interest in the development of alternative renewable energy source [2].

Petroleum reserves are rapidly and continuously depleting at an alarming pace and there is an urgent need to find alternative energy resources to control both, the global warming and the air pollution, which is primarily attributed to combustion of fossil fuels [1].

In order to meet the energy requirements, there has been growing interest in alternative fuels like vegetable oils, biodiesels, biogas, LPG, CNG to provide a suitable diesel oil substitute for internal combustion engine [3].

Biodiesel production is not something new, because the concept of using vegetable oil as fuel dates back to 1895. Rudolf Diesel developed the first diesel engine which has run with vegetable oil in1900. The first engine has run using groundnut oil as fuel [4].

The promotion of biofuels as energy for transportation in the industrialized countries is mainly driven by the perspective of oil depletion, the concerns about energy security and global warming. However due to sustainability constraints, biofuels will replace only 10 to 15% of fossil liquid fuels in the transport sector [5].

Fossil fuels are expected to continue supplying much of the energy used worldwide. Although liquid fuels remain the largest source of energy, their share of world marketed energy consumption is projected to fall from 35% in 2007 to 30% in 2035 (Fig. 1). The decline is due to projected high world oil prices that lead energy users to switch away from liquid fuels when possible [6].

Altough diesel engines are more efficient than gasoline engines of the same power, and this results in lower fuel consumption and thus in lower carbon dioxide emissions [7], the problem associated with the emissions of smoke, PM, sulfur oxide (SO_x), PAHs, and odor from the exhaust of diesel engines has been widely been a concern in many countries [8].

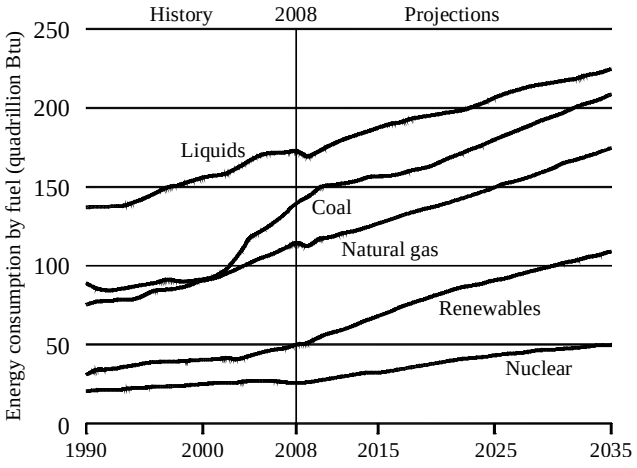


Fig. 1 *World energy consumption by fuel, from 1990 to 2035 [6].*

Diesel engine exhaust is a complex mixture of carbon dioxide, oxygen, nitrogen, nitrogen compounds, carbon monoxide, water vapor, sulfur compounds and numerous low and high molecular weight hydrocarbons, and particulate matter [9].

Exhaust gas emissions of IC engines have been considered a very serious issue regarding air quality and the environment [10] and, therefore, developing and seeking alternative diesel fuels, without modifying engines, has become an important issue [8].

To this context, this paper presents a review of some alternative fuel, like pure plant oil, biodiesel and compressed natural gas, and their impact on diesel engine emissions.

2. Pure plant oil as fuel for diesel engine

As an alternative fuel for compression ignition engines, plant oils are in principle renewable and carbon neutral. However, their use raises technical, economic and environmental issues. A comprehensive and up-to-date technical review of using both edible and non-edible plant oils (either pure or as blends with fossil diesel) in CI engines, based on comparisons with standard diesel fuel, has been carried out [4].

Pure plant oil (PPO), also referred as PVO (Pure Vegetable Oil) or SVO (Straight Vegetable Oil), is the use of plant and vegetable oils without any modification to their chemical structure as a fuel to be combusted inside a diesel engine. This method should not be confused with biodiesel, which is a fuel derived from pure plant oils through a transesterification process that splits fatty acids from glycerin to reduce the viscosity of the pure plant oil similar to that of mineral diesel [11].

Vegetable oils represent a ready, renewable and clean energy source that has shown promise as a substitute to petroleum diesel fuel for diesel engines. There are different ways of utilizing vegetable oils as a substitute for petroleum diesel: (i) crude or refined neat oil; (ii) mixture of oil with diesel fuel with appropriate dilutions; and (iii) alkyl ester products from the transesterification process [12].

Since the most of European biodiesel is made from vegetable oil, this has led to a rapid increase in demand, with a significant impact on European vegetable oil markets [13].

Because the population is constantly growing and also food need is increasing, it is important to focus our attention on non-edible crops. Non-edible oils are not suitable for human food due to the presence of some toxic components in the oil [14].

As indicated by Table 1, numerous plant oils have been tried in diesel engines at some time or other. Relatively few, however, have been systematically evaluated and used [4].

Table 1: *Potential edible and non-edible plant oils for use in CI engines [4].*

Edible oil	Non-edible oil
Sunflower oil, Rapessed oil, Rice oil, Soybean oil, Coconut oil, Corn oil, Palm oil, Olive oil, Pistachia Ol, Sesame seed oil, Peanut oil, Poppy oil, Safflower oil	Jatropha oil, Karanji or Pongamia oil, Neem oil, Jojoba oil, Cottonseed oil, Deccan hemp oil, Kusum oil, Orange oil, Rubber seed oil

Advantages of non-edible crops are ready availability, renewability, higher heat content, lower sulfur content, lower aromatic content and biodegradability, adaptability of cultivating non-edible oil feedstock in marginal land and non-agricultural areas with low fertility and moisture demand, eliminate competition for food and feed [14].

There are 350 species of oil-producing plants and thousands of sub-species [15]. Table 2 gives the average annual oil yield for the common oil plants cultivated in Europe.

Table 2: *Oil producing crops in European Union [adapted from 13]*

Oil producing crops in European Union	kg oil/ hectare
Corn	145
Oat	183
Cotton	273
Hemp	305
Linseed	402
Pumpkin seed	449
Sunflower	800
Rapessed	1000
Olive tree	1019

Diesel engines are designed to burn diesel fuel, which has a lower viscosity than vegetable oil. Therefore the direct usage of pure plant oil in the engine leads to poor fuel atomisation and incomplete combustion, which can rapidly damage the engine. Pure vegetable oil thickness is the central problem for their use since it is 11–17 times thicker than conventional fuel [11].

In the process of converting an engine, adaptations may need to be made to the fuel lines, combustion chamber and fuel injectors. The engine modifications necessary to run a diesel engine with vegetable oils can be divided into two categories: one tank systems and two tank systems. The best way is to fit a professional kit to the diesel engine which includes replacement injectors and glow plugs optimised for vegetable oil, as well as fuel heating [16,8].

The major components of a professional kit are: electrical switching unit (switching to the gas, rinse/ventilation) and an integrated heater (Diesel-Therm), control electronics (diesel - quick rinse, warning when off on vegetable oil), heat exchanger for water / oil circuit, fuel lines, fuel filter, cockpit panel for plant oil / diesel with LED's all operating conditions signal and audible warning when off mode in vegetable oil, complete manufactured cable set with relay sockets, plugs and fuses, various small material (hose clamps), detailed installation manual [17].

With two-tank PPO kits (Fig. 2), one tank holds the vegetable oil and the other petro-diesel (or biodiesel). The engine is started on the petro-diesel tank and runs on petro-diesel for the first few minutes while the vegetable oil is heated to lower the viscosity [11].

Items “O” and “N” represent the two tanks, which are installed inside a vehicle. Heating systems include “M” which is a heater located inside in the vegetable oil tank and “E” which is normally a

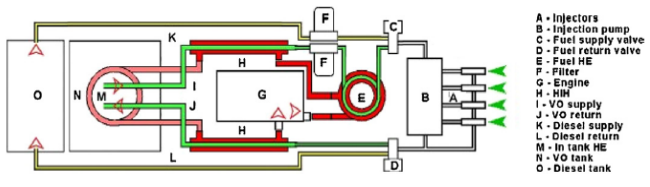


Fig. 2 *Illustration of a two tank system, which allows a vehicle to run on PPO [11].*

special type of heat exchanger. The operation of this system is that upon shut down of the engine the mineral diesel or biodiesel from the smaller tank “O” is feed into the engine until all the vegetable oil is purged out [11].

Literature on using vegetable oils as fuel for diesel engine shows that exhaust gas temperature and smoke intensity may either increase or decrease in comparison to fossil diesel.

Wang et al. [18] carried out a series of experimental tests to evaluate the performance and gaseous emission characteristics of a diesel engine when fuelled with vegetable oil and its blends of 25%, 50%, and 75% of vegetable oil with ordinary diesel fuel separately. The engine works at a fixed speed of 1500 rpm, but at different loads respectively, i.e. 0%, 25%, 50%, 75% and 100% of engine full loads. The experimental results show that power output and fuel consumption are comparable to diesel when fueled with vegetable oil and its blends. The emission of nitrogen oxides (NO_x) from vegetable oil and its blends are lower than that of pure diesel fuel. This emission character found in the tests to some extent is of significance for the practical application of vegetable oil to replace ordinary diesel fuel.

A technical review and life-cycle analysis [4] revealed that when the engine runs on plant oil, emissions of CO and HC may either increase or decrease (Fig. 3). At low load operation using plant oil, CO emission is almost the same as for fossil diesel. Whereas at higher loads, the mixture becomes richer thus more CO is produced due to the lower oxygen content of plant oil. Emissions of NO_x tend to increase with the nitrogen content of the oil. Most literature reports a decrease in NO_x emission with plant oil (or blends) compared to fossil diesel (Fig. 3).

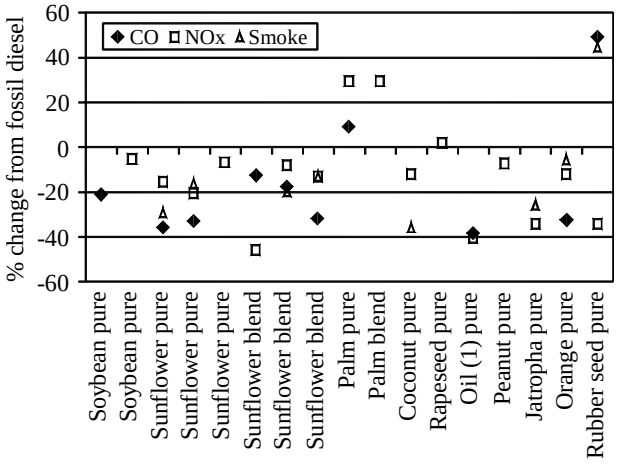


Fig. 3 *CO, NO_x and smoke emission of CI engines running on plant oil (or blends with fossil diesel) as compared to fossil diesel (Oil (1): unknown) [4].*

One can observe that the CO emitted by all biodiesel blends of various origins is lower than that by the corresponding neat Diesel fuel case, with the reduction being higher the higher the percentage of the biodiesel in the blend [19].

Emissions of NO_x tend to increase with the nitrogen content of the oil. The NO_x emissions were slightly reduced with the use of biodiesel or vegetable oil blends of various origins with respect to that of the neat Diesel fuel, with this reduction being higher the higher the percentage of biodiesel or vegetable oil in the blend [4,19].

The smoke density was significantly reduced with the use of biodiesel blends of various origins with respect to that of the neat Diesel fuel, with this reduction being higher the higher the percentage of biodiesel in the blend. On the contrary, it was increased with the use of vegetable oil blends of various origins, with this increase being higher the higher the percentage of vegetable oil in the blend [19].

In other experiment [20], Rakopoulos et al. have evaluated the use of sunflower, cottonseed, corn and olive straight vegetable oils of Greek origin, in blends with diesel fuel at proportions of 10 vol.% and 20 vol.%, in a six-cylinder, turbocharged and after-cooled, heavy duty, direct injection, Mercedes-Benz diesel engine.

Fig. 4 shows, for the speed of 1500 rpm, the emitted nitrogen oxides (NO_x) for the neat diesel fuel, and the 10% and 20% blends of the four vegetable oils with diesel fuel, at the three loads. One can observe that the NO_x emitted by all vegetable oil blends are equal or slightly higher than the ones for the corresponding diesel fuel case, with this increase being higher the higher the percentage of the vegetable oil in the blend [20].

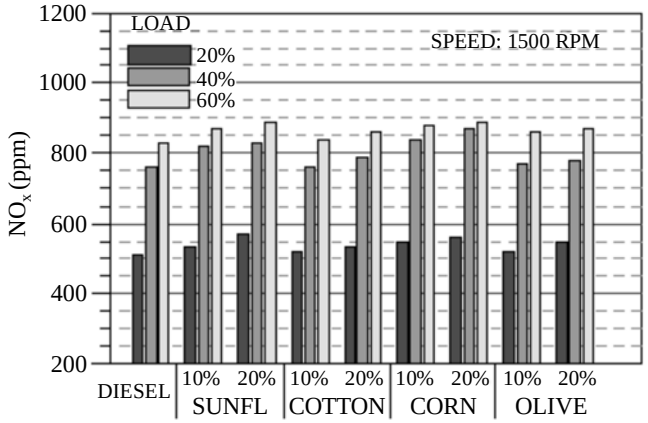


Fig. 4 *Emissions of nitrogen oxides (NO_x) for neat diesel fuel, and the 10% and 20% blends of the four vegetable oil with diesel fuel [20].*

For the same experiment [20], it can be observed that the soot emitted by all vegetable oil blends is lower than the ones for the corresponding neat diesel fuel case, with this reduction being higher the higher the percentage of the vegetable oil in the blend. This is attributed to the combustion being mixing controlled for these vegetable oil blends, as it is also the case for the neat diesel fuel case, which is however now assisted by the presence of the fuel bound oxygen even in locally rich zones [20].

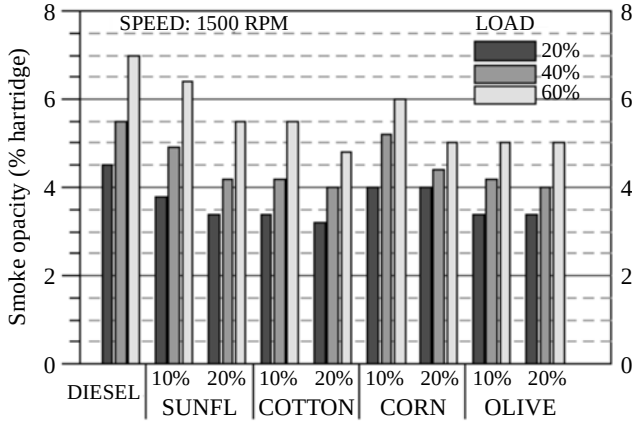


Fig. 5 *Emissions of smoke for neat diesel fuel, and the 10% and 20% blends of the four vegetable oil with diesel fuel [20].*

3. Biodiesel

Crude vegetable oils are inferior as fuel in terms of viscosity, heating value, freezing point, etc. [21]. In order to reduce viscosity, vegetable oils are converted into esters by transesterification

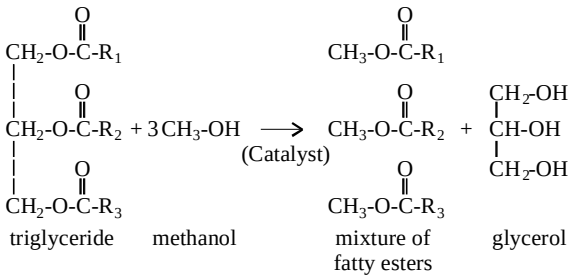


Fig. 6 *Transesterification reaction [22].*

reaction [1]. The result of transesterification reaction (Fig. 6) is biodiesel, as a fuel comprised of mono-alkyl esters of long chain fatty acids derived esters from vegetable oils or animal fats, designated B100 [23].

Because the biodiesel viscosity is almost twice higher than the diesel fuel viscosity (according to Standard EN 14214:2003, the biodiesel viscosity at 40°C is 3.5-5.0 mm^2/s [24]), biodiesel is currently used in blends with diesel fuel.

Biodiesel can be produced from various vegetable oils, waste cooking oils or animal fats. The fuel properties of biodiesel may be changed when different feedstocks are used [25]. However, biodiesel production is highly dependent on many local variables such as feedstock and land availability, costs associated with feedstock procurement, government subsidies and tax reductions as well as interactions with the food industry [26].

The main stages of the fuel systems for biodiesel from vegetable oil and waste cooking oil are shown in Figure 7.

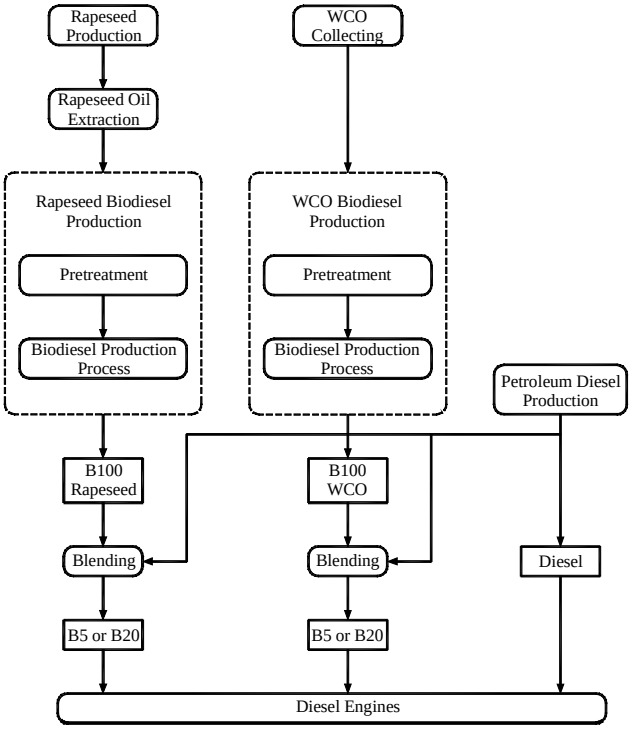


Fig. 7 *Fuel systems for biodiesel from vegetable oil (rapeseed oil) and waste cooking oil (WCO) (adapted from [26]).*

A survey on 27 literatures [27], to study the effect of pure biodiesel on engine power, showed that 70.4% of them agreed that, with biodiesel (especially with pure biodiesel), engine power will

Table 3: *Statistics of effects of pure biodiesel on engine performances (adapted from [27])*

	Total number of references	Increase	%	Similar	%	Decrease	%
		Number		Number		Number	
Power performance	27	2	7.4	6	22.2	19	70.4
Economy performance	62	54	87.1	2	3.2	6	9.7

drop due to the loss of heating value of biodiesel (Table 3). However, the results reported show some fluctuation. Some authors found that the power loss was lower than expected (the loss of heating value of biodiesel compared to diesel) because of power recovery.

Due to the increasing interest in the use of biodiesel, the Environmental Protection Agency (USA) has conducted a comprehensive analysis of the emission impacts of biodiesel using publicly available data [28]. This investigation made use of statistical regression analysis to correlate the concentration of biodiesel in conventional diesel fuel with changes in regulated and unregulated pollutants. Since the majority of available data was collected on heavy-duty highway engines, this data formed the basis of the analysis. The average effects are shown in Figure 8. One may observe that due to higher content of oxygen in biodiesel, CO, PM and HC emission are reduced, but the NO_x emission is higher than that of diesel fossil fuel.

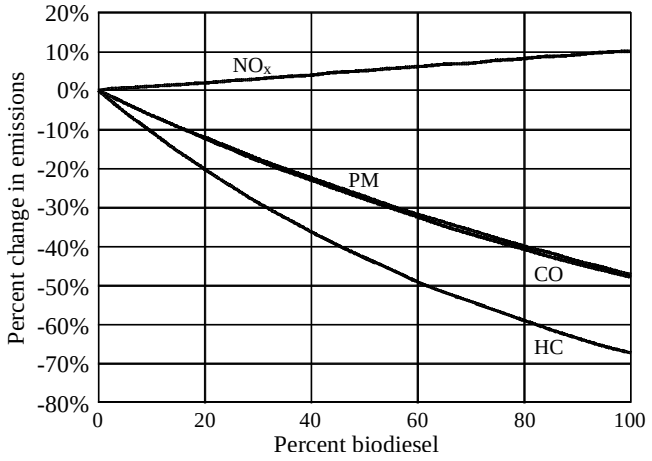


Fig. 8 *Average emission impacts of biodiesel for heavy-duty highway engines [28].*

The results of an experimental investigation [29], using two different samples of B10 blend of eucalyptus biodiesel, showed that smoke opacity improves for both samples, smoke is found to be 64.5% and 62.5% cleaner than that of diesel. Out of all blends B10 was found to be a suitable alternative to conventional diesel fuel to control air pollution without much significant effect on engine performance.

As for the vegetable oils as alternative fuel for diesel engines, the literature on biodiesel emission is not uniform.

In this respect, some available results of Light-Duty diesel vehicle test data for some rapeseed biodiesel blends (a minimum of 20 measurements of a particular blend were required to assess the significance of the effect) allow one to explore the differences in the effects on emissions of the different biodiesel feedstocks [30]. The emission data are discussed as follows:

- HC lower for B20 and B100, but no correlation between biodiesel content in the blend and level of HC emission;
- NO_x higher than for diesel fuel for all blends, the higher content of biodiesel, the higher NO_x emission;
- CO emission is random, lower for B20, but higher for B30;
- Particulate matter (PM) emission is not significant versus diesel fuel. However, a very slight increase of PM for biodiesel blends is observed.

The heterogeneous and uncorrelated data from [27] could be due to the use of biodiesel and biodiesel blends on diesel engines tuned only for pure diesel fuel or for B5-B7 blends. Using higher percentage biodiesel blends, or even B100 fuel, on existing unmodified engines, could cause an inappropriate response of the engine in respect of torque (power) and emission.

4. CNG as fuel for diesel engine

International communities are seeking reliable and alternative fuel sources and technologies to reduce environmental stresses, air pollution, increase fuel availability, decrease the use of and dependence on foreign oil, and optimize the performance of existing fuel supply infrastructures [31].

Natural gas (NG) is one of the most important energy carriers today because it is available in large quantities and its reserves are of the same magnitude as the crude oil reserves [32]. The use of natural gas as a fuel has garnered considerable interest since the beginning of the 1990s.

Italy was the first country in which the use of natural gas as fuel for the propulsion of road vehicles was successful [33]. In the last decade the number of NG vehicles has risen to over a million in several countries around the globe. One reason for this evolution is economic: in many countries NG is considerably less expensive than conventional fuels such as gasoline and diesel. The other advantage is the fact that natural gas burns in a cleaner, less polluting way. Natural gas sources are spread throughout the world, which reduces the risk of an energy crisis [32].

CNG/NG, is a mixture of hydrocarbons in gaseous form, consists of approximately 80-90% of methane along with some percentage of ethane, propane, nitrogen [34]. A gaseous form of natural gas, clearly has some substantial benefits compare to petrol and diesel.

According to [32], the main constituent of NG is methane (80–98%, depending on the extraction source). Other (about 2%), butane and pentane (less than constituents are ethane (1–8%), propane 1%). NG also contains nitrogen and carbon dioxide (0.2–1.5%) and small quantities of sulfur compounds (hydrogen sulphide and mercaptans). Of all hydrocarbon compounds used as motor fuels, methane has the highest knock resistance [32]. Its octane number is ca. 130. NG is non-toxic, odourless and non-corrosive. It is lighter than air and is slightly soluble in water.

Amrouche et al. [35] have found that CNG:

- Is composed of 85 to 99% methane;
- Has the highest energy/carbon ratio of any fossil fuel, and has a high octane (110/130) (against 95 and 98 for gasoline and 92/96 for the diesel). His feature helps the increase of the compression ratio engines and thus the efficiency;
- Is safely: It is lighter than the air, in the case of gas leak, it goes to the atmosphere;
- Auto-ignite above 540°C (450°C for LPG, 220°C for unleaded gasoline and 225°C for diesel).
- Doesn't freeze until below -165°C, which makes it insensitive with the climatic conditions.

One of the reasons to use NG as an alternative fuel was the ecological consideration [32], NG having the potential to mitigate CO_2 emissions due to its lower carbon content [36].

Natural gas is used as a fuel in two forms [32]:

1. In its gaseous form (at ambient temperature and under a high pressure of 20 MPa) it is called compressed natural gas (CNG).
2. In its liquid form (cooled to a temperature of -161°C at atmospheric pressure) it is called liquefied natural gas (LNG).

In the case of using CNG, vehicle engines should be modified (dedicated/retrofitted) at the same time with changing fuels [36]. Dedicated vehicles are preferable but there are a few light-duty CNG vehicles available. For applying to a specific type of vehicle, retrofitting is an option. However, the efficiency of retrofitted vehicles is questionable on reduction of CO_2 emissions [36].

In order to ensure smooth transportation life cycle and sustainability, it is important to synchronize CNG fuel supply, CNG refueling stations and CNG fuel vehicles [31]. Recent studies show that the proper implementation with reasonable ratio of refueling stations to alternative fuel vehicle is of great importance [31].

Many investigations were carried out in order to use of CNG as an alternative fuel according to their fuel usage and they are [34]:

- Dual fuel: like the CNG buses the mixture of CNG and diesel introduced in the engine. As natural gas will not ignite under combustion chamber alone so diesel is required.
- Bi-fuel: like cars and light motor vehicle, convention petrol engine where the fuel system has been modified to operate either petrol gas.
- Mono-fuel: this is specialized engine type which has been designed and optimized to operate only on natural gas.

The natural gas vehicle is currently one of least polluting vehicles available on the market [35]. In fact, compared to others vehicles powered with petroleum products, the CNG vehicles have shown a very strong reduction of the polluting emissions (-100 % of lead, the Non-Methane Hydrocarbons are reduced by approximately 50%, - (50-87%) of NO_x, - (20-30%) of CO_2, - (70-95%) of CO. And the combustion of natural gas produces almost no fine particulate matter). Natural gas vehicles have significantly low noise levels and engine vibration, it reduce noise about -5 to -8 decibels by vehicle [35].

Introducing vehicles that run on CNG can significantly reduce black carbon emissions from on-road vehicles [37].

The use of natural gas as a vehicle fuel is claimed to provide several benefits to engine components and effectively reduce maintenance requirements [34]. It does not mix with or dilute the lubricating oil and will not cause deposits in combustion chambers and on spark plugs to the extent that the use of petrol does, thereby generally extending the piston ring and spark plug life. In diesel dual-fuel operation evidence of reduced engine wear is reported, leading to expected longer engine life [34].

Development of the CNG dual-fuel turbocharged CI engine was described in reference [32]. NG was introduced into the engine cylinder in the gaseous state through a honeycomb mixer. The pilot ignition fuel was diesel fuel. The following results on emissions were obtained (Fig. 9):

- An increase in pilot diesel fuel extends the lean burning limit and decreases HC and CO emissions (while NO_x emissions increase), which is generally higher than for diesel fuelling.
- Smoke emission is considerably reduced for dual fuelling.
- NO_x emission is also reduced.

5. Conclusions

To meet the energy requirements and environmental concerns, there has been growing interest in alternative fuels like vegetable oils, biodiesel and CNG to provide a suitable diesel oil substitute for internal combustion engine.

As an alternative fuel for compression ignition engines, plant oils are in principle renewable and carbon neutral, but their use raises technical, economic and environmental issues.

There are different ways of utilizing vegetable oils as a substitute for petroleum diesel: (i) crude or refined neat oil; (ii) mixture of oil with diesel fuel with appropriate dilutions; and (iii) alkyl ester products from the transesterification process.

Since diesel engines are designed to burn diesel fuel, which has a lower viscosity than vegetable oil, using only vegetable oil as fuel needs to fit a professional kit to the diesel engine, which includes replacement injectors and glow plugs optimised for vegetable oil, as well as fuel heating.

Literature on using vegetable oils as fuel for diesel engine shows that CO emission is decreasing, while emissions of NO_x tend to increase.

To reduce the viscosity of vegetable oils, vegetable oils are converted into esters by transesterification reaction. Because the biodiesel viscosity is almost twice higher than the diesel fuel viscosity, biodiesel is currently used in blends with diesel fuel.

Using pure biodiesel, engine power drops due to the loss of heating value of biodiesel. In some cases, the power loss was lower than expected because of power recovery.

Due to higher content of oxygen in biodiesel, CO, PM and HC emission are reduced, but the NO_x emission is higher than that of diesel fossil fuel.

One of the reasons to use natural gas as an alternative fuel was the ecological consideration, NG having the potential to mitigate CO_2 emissions due to its lower carbon content.

In the case of using CNG, vehicle engines should be modified at the same time with changing fuels. Dual fuel, bi-fuel or mono-fuel fuel systems have been designed and optimized to allow diesel and spark ignition engines to operate only on natural gas.

Compared to others vehicles powered with petroleum products, the CNG vehicles have shown a very strong reduction of the polluting emissions.

The use of natural gas as a vehicle fuel is claimed to provide several benefits to engine components and effectively reduce maintenance requirements .

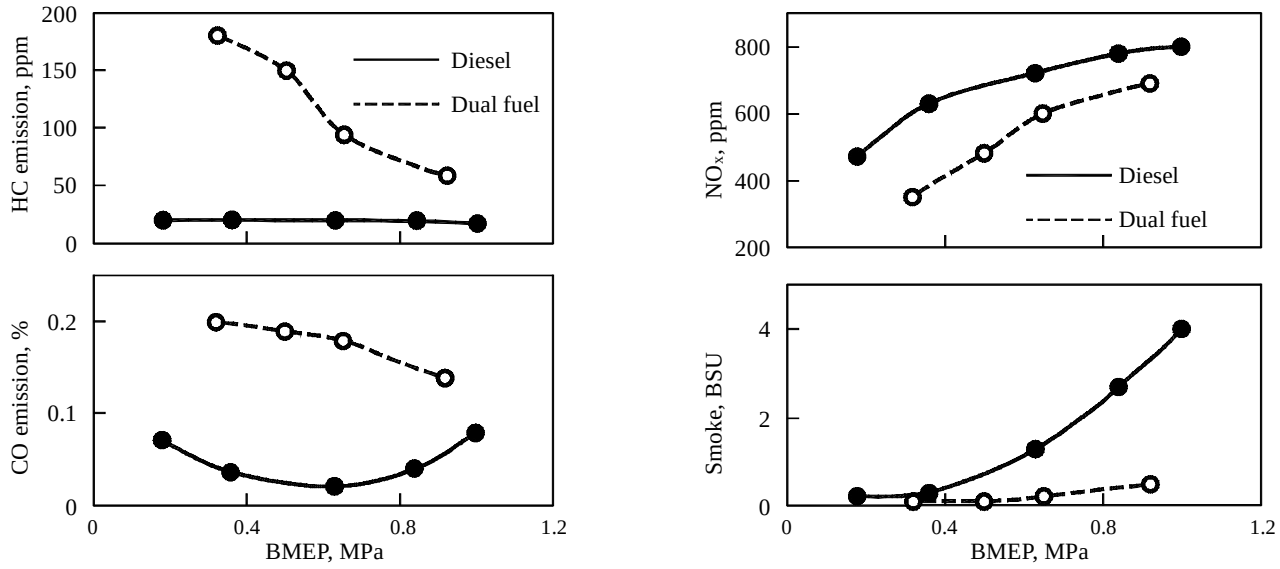


Fig. 9 *HC, CO, NO_x and smoke emissions versus b.m.e.p. for dual and diesel fuelling of a turbocharged engine at n=1600 r/min [32].*

6. References

[1] Agarwal, A. K. et al. Particulate emissions from biodiesel fuelled CI engines. Energy Conversion and Management 94 (2015) 311–330.

[2] Atadashi, I. M. Crude biodiesel refining using membrane ultra-filtration process: An environmentally benign process. Egyptian Journal of Petroleum (2015) 24, 383–396.

[3] De, B., R. S. Panua. An experimental study on performance and emission characteristics of vegetable oil blends with diesel in a direct injection variable compression ignition engine. Procedia Engineering 90 (2014) 431–438

[4] Hossain, A. K., P.A. Davies. Plant oils as fuels for compression ignition engines: A technical review and life-cycle analysis. Renewable Energy 35 (2010) 1–135.

[5] Palit, S., A. K. Chowdhuri, B. K. Mandal. Environmental impact of using biodiesel as fuel in transportation: a review. Int. J. Global Warming, Vol. 3, No. 3, 2011.

[6] Promoting Green Energy for Better Tomorrow. Pakistan Renewable Energy Society. http://www.pres.org.pk/category/energy/

[7] Alfieri, E. Emissions-Controlled Diesel Engine. A dissertation submitted to the Swiss Federal Institute of Technology Zurich for the degree of Doctor of Sciences. 2009. http://e-collection.library.ethz.ch/eserv/eth:41539/eth-41539-02.pdf

[8] Lin, Y.-C. et al. Approach for Energy Saving and Pollution Reducing by Fueling Diesel Engines with Emulsified Biosolution/ Biodiesel/Diesel Blends. https://www.researchgate.net/publication/5309993_Approach_for_Energy_Saving_and_Pollution_Reducing_by_Fueling_Diesel_Engines_with_Emulsified_BiosolutionBiodieselDiesel_Blends

[9] McClellan, R. O., T. W. Hesterberg, J.C. Wall. Evaluation of carcinogenic hazard of diesel engine exhaust needs to consider revolutionary changes in diesel technology. Regulatory Toxicology and Pharmacology 63 (2012) 225–258.

[10] Sane, H. et al. Emission reduction of IC engines by using water-in-diesel emulsion and catalytic converter. IJRET: International Journal of Research in Engineering and Technology, Volume: 03 Issue: 08 | Aug-2014, pp. 378-383.

[11] Russo, D. et al. State of the art of biofuels from Pure Plant Oil. Renewable and Sustainable Energy Reviews 16 (2012) 4056–4070.

[12] Z. Franco, Q. D. Nguyen. Flow properties of vegetable oil–diesel fuel blends. Fuel 90 (2011) 838–843.

[14] Atabani, A. E. et al. Non-edible vegetable oils: A critical evaluation of oil extraction, fatty acid compositions, biodiesel production, characteristics, engine performance and emissions production. Renewable and Sustainable Energy Reviews 18 (2013) 211–245.

[13] Vegetable oil markets and the EU biofuel mandate. The International Council on Clean Transportation, February 2013, http://www.theicct.org/sites/default/files/publications/ICCT_vegoil_and_EU_biofuel_mandate_20130211.pdf

[15] Joshua and Kaia Tickell, From the Fryer to the Fuel Tank. The complete guide to using vegetable oilas an alternative fuel. Second Edition. GreenTeach Publishing, USA. 1999, ISBN 0-9664616-1-4.

[16] Pure plant oil as fuel. Technical aspects and legislative context. https://ec.europa.eu/energy/intelligent/projects/sites/iee-projects/files/projects/documents/agriforenergy_2_pvo_handbook_en.pdf

[17] Conversion from Diesel Engines to run with Pure Plant vegetable Oil. http://heipro.com/

[18] Wang, Y. D. et al. An experimental investigation of the performance and gaseous exhaust emissions of a diesel engine using blends of a vegetable oil. Applied Thermal Engineering 26 (2006) 1684–1691.

[19] Rakopoulos, C. D. et al. Comparative performance and emissions study of a direct injection Diesel engine using blends of Diesel fuel with vegetable oils or biodiesels of various origins, Energy Conversion and Management 47 (2006) 3272–3287.

[20] Rakopoulos, C. D. et al. Comparative environmental behavior of bus engine operating on blends of diesel fuel with four straight vegetable oils of Greek origin: Sunflower, cottonseed, corn and olive, Fuel 90 (2011) 3439–3446.

[21] Arbab, M. I. et al. Fuel properties, engine performance and emission characteristic of common biodiesels as a renewable and sustainable source of fuel. Renewable and Sustainable Energy Reviews 22 (2013) 133–147.

[22] Van Gerpen, J. et al. Biodiesel Production Technology. NREL/SR-510-36244, Contract No. DE-AC36-99-GO10337, 2004.

[23] ASTM D 6751 – 02 Standard Specification for Biodiesel Fuel (B 100) Blend Stock for Distillate Fuels, http://www.biofuels.coop/pdfs/12_astm.pdf

[24] EN 14214:2003 (E) Automotive Fuels - Fatty Acid Methyl Esters for Diesel Engines - Requirements and Test Methods

[25] Ozsezen, A. N., M. Canakci. Determination of performance and combustion characteristics of a diesel engine fueled with canola and waste palm oil methyl esters. Energy Conversion and Management 52 (2011) 108–116.

[26] Ozata, I. et al. Comparative Life Cycle Assessment Approach for Sustainable Transport Fuel Production from Waste Cooking Oil and Rapeseed. January 2009, http://www.researchgate.net/publication/228406700

[27] Xue, J., T. E. Grift, A. C. Hansen. Effect of biodiesel on engine performances and emissions. Renewable and Sustainable Energy Reviews 15 (2011) 1098–1116.

[28] A Comprehensive Analysis of Biodiesel Impacts on Exhaust Emissions, Draft Technical Report EPA420-P-02-001, October 2002.

[29] Verma, P., M. P. Sharma, G. Dwivedi. Potential use of eucalyptus biodiesel in compressed ignition engine. Egyptian Journal of Petroleum (2015) xxx, xxx–xxx, in press.

[30] Anderson, L. G. Effects of Biodiesel Fuels Use on Vehicle Emissions. Journal of Sustainable Energy & Environment 3 (2012) 35-47.

[31] Gabbar, H. A., R. Bedard, N. Ayoub. Integrated modeling for optimized regional transportation with compressed natural gas fuel. Alexandria Engineering Journal (2016) 55, 533–545.

[32] Kowalewicz, A., M. Wojtyniak. Alternative fuels and their application to combustion engines, Proceedings of the Institution of Mechanical Engineers, Part D: Journal of Automobile Engineering 2005 Vol. 219: 103–125.

[33] Berghmans, J., M. Vanierschot. Safety aspects of CNG cars. Procedia Engineering 84 (2014) 33–46.

[34] Saraswat, M. et al. Assessment of different alternative fuels for internal combustion engine: A review. International Journal of Engineering Research & Management Technology, May- 2015 Volume 2, Issue-3, ISSN: 2348–4039.

[35] Amrouche, F. et al. Compressed Natural Gas: The new alternative fuel for the Algerian transportation sector. Procedia Engineering 33 (2012) 102–110.

[36] Gojash, O., A. Fukuda, T. Fukuda. Estimation of CO_2 emissions reduction using alternative energy – Potential Application of Clean Developed Mechanism (CDM) in the Transport Sector to Developing Countries. IATSS Research Vol. 31 No.1, 2007, pp. 32–40.

[37] Kholod, N., M. Evans. Reducing black carbon emissions from diesel vehicles in Russia: An assessment and policy recommendations. Environmental Science & Policy 56 (2016) 1–8.

DEVELOPMENT OF GEOMETRY OF CARVIDE MULTIFACE PLATES FOR SUPERFINISH PROCESSING

РАЗРАБОТКА ГЕОМЕТРИИ МНОГОГРАННЫХ ТВЕРДОСПЛАВНЫХ ДЛЯ СУПЕРФИНИШНОЙ ОБРАБОТКИ

Rechenko D., Popov A., Titov Yu., Gritsenko B.
Omsk State Technical University - Omsk, Russia

Protective coatings are widely used for carbide tools stabilization and functionality. Surface hardening of carbide tools by coatings which are based on titanium nitride is allowed to stabilize them for 3-5 times. But they are not available in cases of affinity of chemical elements with composition of worked stock. Multilayered coating provides sufficient toughness of the coating and high durability by the front coating allows to process different constructional materials efficiently [1].

Superfinish and finish edge cutting machining can be only with usage of high-quality tools but with an ideal wedge which has edge less than 1 μm affects to have optimum shapes during the work. At start time of shake-down period this edge assumes the rounding and its dimensions are depended on cut depth, approach, tooling and worked material which assign intensity of production process.

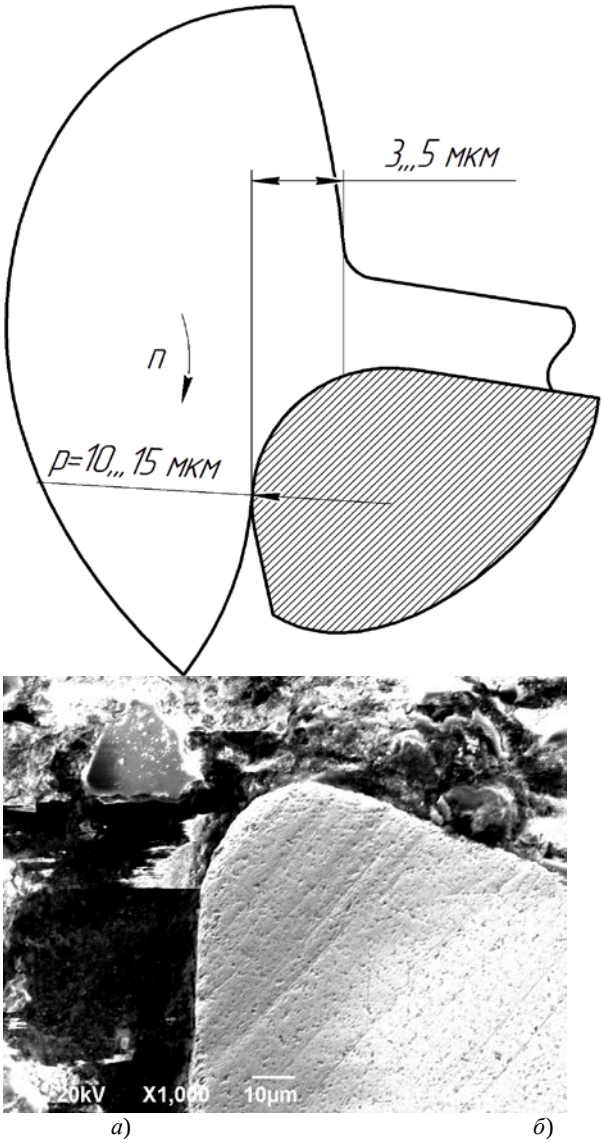
Generally accepted finish machining is characterized by the production mode: approach S = 0,1…0,3 mm/turn and cut depth is a_p = 0,5…2,0 mm. Superfinish - S = 0,05…0,15 mm/turn and a_c = 0,25…2,0 mm. Even with the lowest process rates, edge (conditional inscribed radius of rounding edge) of standard metal-cutting tool (ρ = 15…25 μm) is enough for stable operation. With process rates: approach S < 0,05 mm/turn and cut depth is a_p < 0,1 mm, for example, S = 0,01 mm/turn and a_c = 0,010 mm, the edge of modern tool does not provide the stable operation (Fig. 1)

Cutting process will be accompanied with deformation and hardening of surface layer of the work piece. It is necessary to provide the correspondent edge and the application of a harden negative chamfer is allowed to stabilize the tool for the normal operation of the cutting tool. In Figure 2 there is a dependence of kinematic chip thickness on lead angle φ *and* approach *S.* It is seen from the dependence that with the decreasing of lead angle φ *and* approach *S* kinematic chip thickness h_m decreases.

The creation of edge (with short conventional inscribed radius) strictly defined form of the cutting edge of the tool increases the quality of finish, but the carbides do not bear the load increasing and fail rather quickly and in the result the quality of processing coating decreases and tools can be failed. Solving of this issue is to apply a hardening coating but nowadays a lot of traditional coatings are developed but not all of them are suitable. With the covering of the coat the circle radius and as consequence the processing accuracy and quality decreases. Moreover they are quite fragile. With the cutting edge of 1 μm the coating thickness must have commensurable dimensions (traditional coatings have optimal thickness 5 μm).

Consequently, the coatings which can bear a high load and provide a long-term usage of tools at shallow thicknesses are necessary. At inserted carbide cutting with the coatings should not be seizure with the work materials. The last one is essential at hard-to-cut materials processing on basis of titanium, nickel, aluminium and etc. Coatings must possess a small friction ratio combined with the work material, possess damping properties and not be subjected to brittle failure.

For the purpose of finding out of influence of the light coatings on the tool cutting characteristics the study of tool with coating operation Al-Si-N and into the part of coatings are additionally implemented ions Mo has been made.



а) *б*)

Figure 1 – Edge of modern metal-cutting tool: *a*) cutting pattern; *b*) picture of the edge in cross-section

From the tests of cutting edge tool made by the authors it is stated that negative chamfer must have an angle γ = -5°…-15° and width chamfer is fixed by the forming width of cutting which depends on depth of cut and approach. The realization of superfinish processing with the light feed and depth of cutting is possible only with high edge of the tool. From the tests it is stated that the stable cutting is observed in the ratio of layer cut thickness and the edge.

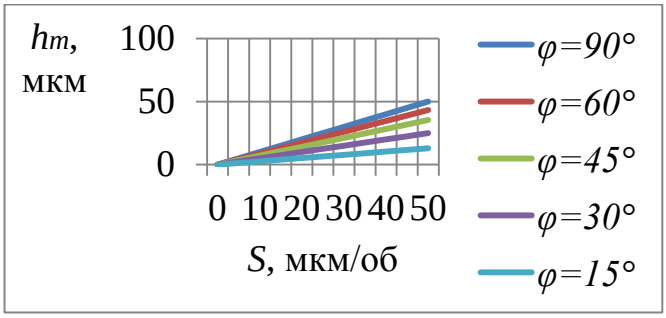


Figure 2 *– Graph of kinematic chip thickness from lead angle φ and approach S*

In operation research of the edge's keenness influence on the cutting process in processing heat-resistant alloy was carried out. The high-quality edge was obtained through the high-speed sharpening (grinding speed is 350...400 m/s).

On the basis of research results of the stable cutting were obtained. Figure 3 shows recommended ratio of layer cut thickness and the edge's keenness.

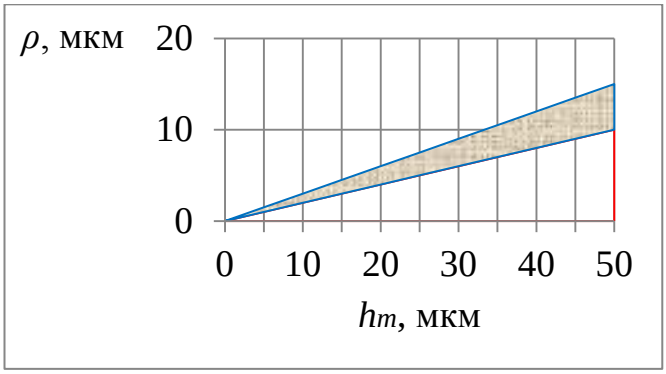


Figure 3 *– Graph of recommended edge ρ from kinematic chip thickness h_m in the area of the stable cutting*

The graph makes possible to identify required edge's keenness of carbide tool in the ratio $5 < R_{c.a.} \leq 10$, where $R_{c.a.}$ is the ratio of the cutting ability, which has a dependence, defined as $R_{c.a.} = h_m / \rho$. That is the ratio of the cutting ability depends on kinematic chip thickness h_m and edge's keenness ρ. From the above ratio of the cutting ability it's possibly to define the area of stable cutting.

Analysis of industrial experience and literary data allowed to define that the usage of negative chamfer increases durability and can have different dimensions and shape. Negative chamfer serves as strengthening edge's element.

For comparison of the cutting process the analysis of existing microgeometry carbide tools was conducted. The analysis showed that sharpening of high-quality carbide tool with the formation of negative chamfer and additional chamfers (Fig. 4,*a* – 4,*d*) changes the mechanism of their wear and increases the life.

There are several types of chamfers [2]. The size of the negative chamfer along the contour and on front surface depending on specifications should be 30…50% of the kinematic chip thickness h_m.

For approvement of the influence of the chamfer on the cutting process of hardmachining materials geometry with negative chamfer $f = 3…5$ μm and an angle $\gamma = -10°$ (Fig. 4, a) and geometry of edge tool free from edge's defects with the sharpness $\rho = 1…2$ μm, while all plates were covered by *Al-Si-N*.

a) Negative chamfer
$f = (0{,}3…0{,}5) \cdot h_m$
$\gamma = -5°…-15°$

b) Double negative chamfer
$f = (0{,}3…0{,}5) \cdot h_m$
$f_2 = 0{,}5 \cdot f$
$\gamma = -5°…-15°$
$\gamma_1 = -10°…-20°$

c) Rounding negative chamfer
$f = (0{,}3…0{,}5) \cdot h_m$
$R = (2…3) \cdot h_m$

d) Negative chamfer with rounding
$f = (0{,}3…0{,}5) \cdot h_m$
$\gamma = -5°…-15°$
$R = (1…2) \cdot h_m$

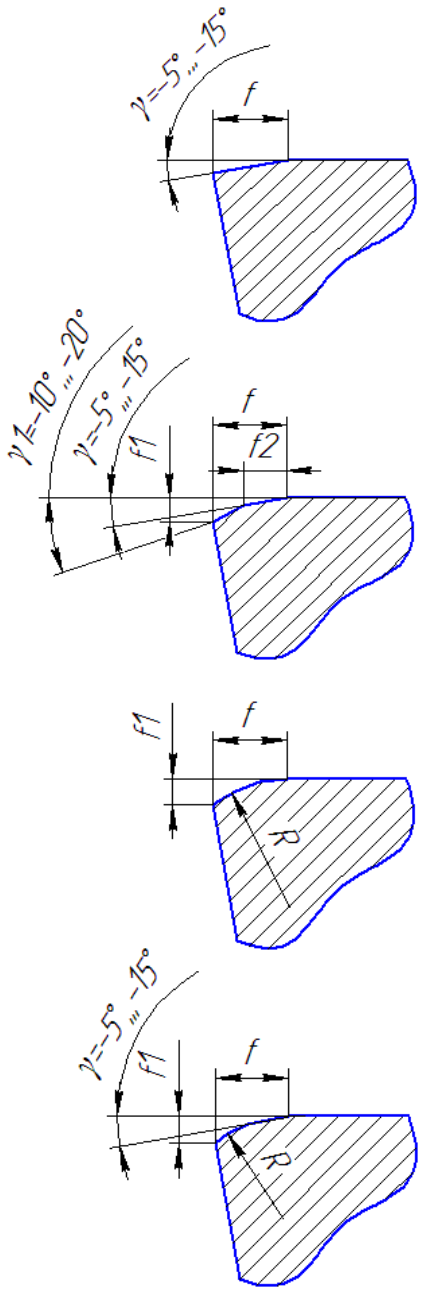
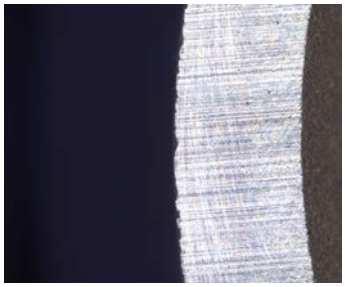
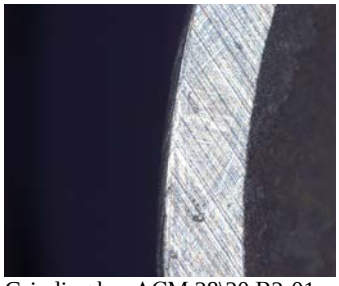


Figure 4 *– Types of negative chamfers*

Tests of different bars were conducted for comparison of influence of abrasive material on production of the chamfer. Meanwhile chamfer on the edge was produced experimentally with the use of different abrasive materials (Fig. 5).



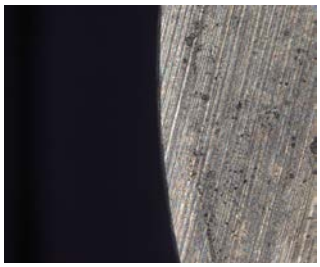
Grinding bar 47 F2500 (main fraction 8,4 μm) Norton (Brazil)
a)



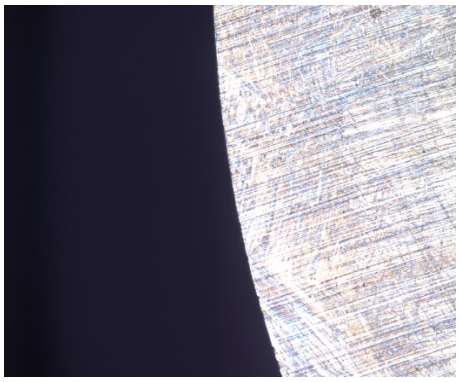
Grinding bar ACM 28\20 B2-01 (main fraction 23 μm) (Russia)
b)



Grinding bar on volcanite bundle Э5 32ГТ (corresponds to the mark of abrasive material 14A) (main fraction 348 μm) Luga (Russia)
c)



Grinding bar ACH 7/5 4 B2-01 (main fraction 5,5 μm) Inrost (Инрост) (Russia)
d)



Grinding bar with suspension of submicropowder Masaper prep polishing suspension 0,05 μm (USA)
e)

Figure 5 *– Edge of carbide tool, produced after blunting by different abrasive materials*

Analysis of the results showed that the best result was obtained using the grinding bar ACH 7/5 4 B2-01 (main fraction 5, 5 μm) Inrost (Инрост) (Russia) (Fig. 5,*d*), chamfer in the range 3...5 μm. Usage other abrasive materials doesn't allow to get a stable result. Grinding bar 47 F2500 (main fraction 8, 4 μm) Norton (Brazil) (Fig. 5,*a*) makes defects on the edge in form of microchips. Grinding bars ACM 28/20 B2-01 (main fraction 23 μm) (Russia) (Fig. 5,*b*) and on volcanite bundle Э5 32ГТ (corresponds to the mark of abrasive material 14A) (main fraction 348 μm) Luga (Russia) (Fig. 5,*c*) make obstructions on the edge, and grinding bar with suspension of submicropowder Masaper prep polishing suspension 0,05 μm (USA) (Fig. 5,*e*) allows to make a chamfer and to produce any processing at all. In the last case the result can be supposedly explained by the fact that abrasive material has a low hardness and it can't make processing.

Selected the best in terms of cutting geometries of the tool were covered with *Al-Si-N*. Except various geometries coating *Al-Si-N* was used in the work, the thickness of which amounted to 2,3 μm on the front side. The coating was formed with much worse adhesion with a thickness 0,26 μm at the back side because of the spraying (Fig. 6).

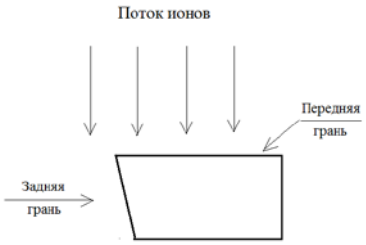


Figure 6 *– The scheme of coating*

Small thickness and actually one-sided covering of coatings preserve edge's keenness. Because of the significant difference in coating hardness and base the back side will wear more quickly, which would lead to the realization of the self-sharpening condition and longer tool operation.

Coatings, that is ~2...2,5 μm thick, were settled on the vacuum unit УВН-05МД «КВАНТ» in argon-nitrogen gas mixture at a total pressure 0,3 Pa and the ratio of partial pressures *Ar*: *N* = 3 : 1 by the method of the bipolar impulsive magnetron sputtering of mosaic target based on aluminum with silicon inserts. The discharge power of the magnetron was 1,2 kW; frequency of current impulse was 50 kHz. Heating sublayers and maintaining their constant temperature in the settling process of coatings were carried out by molybdenum resistive heater power of 10 kW. The chemical composition of coatings *Al-Si-N* included: *Al* – 34 at.%, *Si* – 13 at.%, *N* – 53 at.%. Figure 7 shows a sketch of carbide plates which used in the work. Also in the same way plates implanted with molybdenum *Mo* in the coating *Al-Si-N* were tested.

Figure 8 presents edges of carbide sharp plates with the chamfer which covered with hardening coating *Al-Si-N* and coating implanted with molybdenum *Mo*.

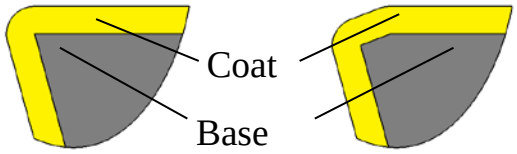
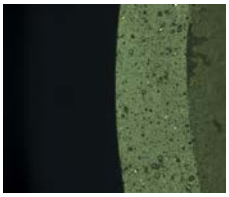
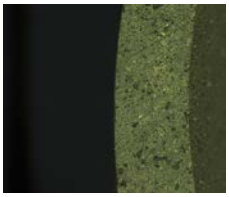


Figure 7 *– Sketch of carbide plates with the coat*

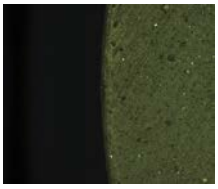
Durability tests of carbide plates were carried out in turning steel XH77TIOP on a lathe machine *Okuma ES-L8II*. Cutting fluid *BlasoCut* 2000 was used. Processing condition in turning: cutting speed *V = 40 m/min*, longitudinal feed *S = 0,05 mm/Rev* and depth of cutting on the diameter t_d = 15 μm.



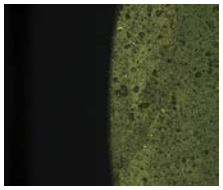
Sharp edge, coat *Al-Si-N*



Sharp edge, coat *Al-Si-N + Mo*



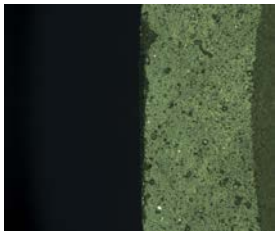
With the chamfer, coat *Al-Si-N*



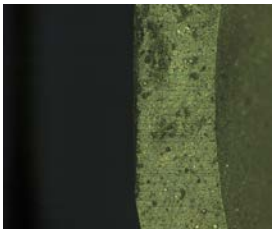
With the chamfer, coat *Al-Si-N + Mo*

Figure 8 *– Edges of carbide sharp plates and with the chamfer*

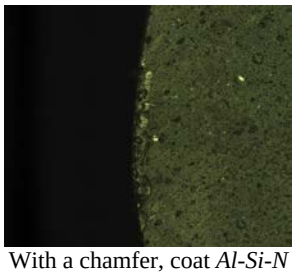
The results of tests showed that plates had different wear (Fig. 9).



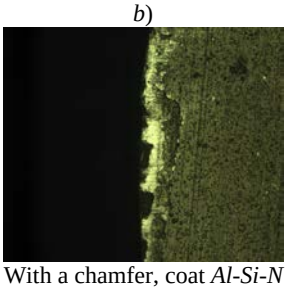
Sharp edge, coat *Al-Si-N*
a)



Sharp edge, coat *Al-Si-N + Mo*
b)



With a chamfer, coat *Al-Si-N*
c)



With a chamfer, coat *Al-Si-N + Mo*
d)

Figure 9 *– Edges of carbide sharp plates and with the chamfer*

Sharp edge plate (Fig. 9,*a*) has strongly pronounced blaze and classic wear on the back surface. Sharp edge plate with the coat and implanted molybdenum *Mo* (Fig. 9,*b*) has classic wear on the back surface. Plate with the chamfer and coat *Al-Si-N* (Рис. 9,*c*) has residual trace of excrescence (stagnant zone), while preserved coat, and the plate with the chamfer and implanted molybdenum *Mo* (Рис. 9,*d*) has strongly pronounced wear on the front surface with flaking coat and residual trace of excrescence. At the same time this plate has chipping on the edge. The best result for durability and quality of processing was showed by the plate with negative chamfer and coat.

Tool durability was assessed by quality parameters of details' processing. Change of roughness was assessed visually, and was measured by profilometer *MarSurf PS*1. Results for durability compared to the original plate are shown in Table 1.

Table 1 – *Durability carbide sharp plates and with a chamfer*

Plate	Durability T, min	Passed way L, m	Treated area S, cm^2
Sharp edge, coat *Al-Si-N*	42,4	1696	847,8
Sharp edge, coat *Al-Si-N + Mo*	59,5	2379	1189,7
With a chamfer, coat *Al-Si-N*	169,6	6782	3391,2
With a chamfer, coat *Al-Si-N + Mo*	43,5	1741	870,4
Original	31,3	1252	626,1

Conclusion: In processing of heat-resistant alloy ХН77ТЮР the best result for durability and quality of processing was given by carbide plate, which has the edge ρ = 1…2 μm free from edge's defects, original geometry with negative chamfer f = 3…5 μm, and an angle γ = -10°, with coat *Al-Si-N*.

References

1. Kornievich M. Cutting theory: textbook / Kornievich M., Feldstein E., Yashcheritsyn P. – Minsk: Novoe znanie, 2007. – 512 p.
2. Catalogue Sandvik Coromant.

SYNCHRONIZATION T-CHAOTIC SYSTEM

Assist.Prof. Sahab A.R. PhD.[1], M.Sc. Abazari M.[1]
Faculty of Engineering - Lahijan Branch Islamic Azad University, Iran [1]

sahab@liau.ac.ir

Abstract: *In this paper, we study on chaos, one of the most important phenomenons based on complex nonlinear dynamics. We will focus on T-system chaos and in continue, using three synchronization methods, Brain Emotional Learning Based Intelligent Controller (BELBIC), Generalized Backstepping Method (GBM) and adaptive method, the chaotic system will be synchronized. To prove usability of the controllers, the results will be compared with the results obtained by Active Control and Backstepping Controllers. According to the results, proposed controllers synchronize chaotic systems with higher speed, lower setting time, lower overshoot and smaller control signal versus active control and backstepping controllers.*

Keywords: CHAOS, BELBIC, GENERALIZWD BACKSTEPPIG METHOD, ACTIVE CONTROL

1. Introduction

Chaos is an important phenomenon, happens vastly in both natural and man-made systems. Lorenz [1] faced to the first chaotic attractor in 1963. In continue, a lot of researches were achieved on chaotic systems [2-11]. A new 3D chaotic system (T-system) from the Lorenz system was derived in [12,13]. Over the last two decades, chaos control and synchronization have been absorbed increasingly attentions due to their wide applications in many fields [14–25]. Active control [28], backstepping [28] and adaptive control [28] are three different methods for synchronization of T system. Active control [28] and backstepping [28] methods are selected when system parameters are known, and adaptive control [28] method is applied when system parameters are unknown. GBM [26,27], a new method to optimize backstepping method, controls chaos in nonlinear systems better than backstepping design.

A kind of BELBIC model was introduced to control nonlinear systems [29] and aerospace launch vehicle control [30]. Another model of BELBIC was proposed for control and tracking of vehicles [31] and Intelligent autopilot control design [32]. This paper proposes new controllers to control and Synchronize T chaotic system according to three models, BELBIC [29,30], GBM [26,27] and adaptive method, and Simulation results shows that mentioned controllers synchronize this chaotic system more better and faster than active control and backstepping controllers.

2. Generalized Backstepping Method (GBM)

GBM [26-27] will be applied to a certain class of autonomous nonlinear systems which are expressed as

$$\begin{aligned} \dot{X} &= F(X)+G(X)\eta \\ \dot{\eta} &= f_0(X,\eta)+g_0(X,\eta)u \end{aligned} \tag{2}$$

In which $\eta \in \Re$ and $X=[x_1,x_2,\ldots,x_n]\in \Re^n$. In order to obtain an approach to control these systems, we may need to explain a new theorem as follow.

Theorem. Suppose (2) is available, then $\varphi_i(X)$ for the i_{th} state could be determined i a manner which by inserting the i_{th} term for η, $V(X)$ would be a positive definite (3) with negative definite derivative.

$$V(X)=\frac{1}{2}\sum_{i=1}^{n} x_i^2 \tag{3}$$

Therefore, the control signal and also the general control Lyapunov function of this system can be obtained by (4) and (5).

$$\begin{aligned} u=\frac{1}{g_0(X,\eta)}\Bigg\{&\sum_{i=1}^{n}\sum_{j=1}^{n}\frac{\partial\varphi_i}{\partial x_j}[f_i(X)+g_i(X)\eta]-\sum_{i=1}^{n}x_i g_i(X) \\ &-\sum_{i=1}^{n}k_i[\eta-\varphi_i(X)]-f_0(X,\eta)\Bigg\};\ k_i>0 \quad ; \quad i=0,1,2,\ldots,n \end{aligned} \tag{4}$$

$$V_t(X,\eta)=\frac{1}{2}\sum_{i=1}^{n}x_i^2+\frac{1}{2}\sum_{i=1}^{n}[\eta-\varphi_i(X)]^2 \tag{5}$$

3. Genetic Algorithm

The genetic algorithms are used to search the optimal parameter k (k_j; $j=1,2$ is positive constant) in order to guarantee the stability of systems by ensuring negativity of the Lyapunov function and having a suitable time response [33-34]. The fitness function used is

$$f=\frac{1}{n}\sum_{i=1}^{n}e_i^2 \tag{6}$$

Table 1: *Genetic Algorithm Parameters*

Parameters	Values
Size population	100
Maximum of generation	300
Prob.crossover	75
Prob.mutation	0.001
k_j search interval de	[0.1 10]

4. T-Chaotic System

State space of T system is expressed as

$$\begin{aligned} \dot{x} &= a(y-x) \\ \dot{y} &= (c-a)x-axz \\ \dot{z} &= -bz+xy \end{aligned} \tag{7}$$

Where $a=2.1, b=0.6, c=30$ are system constants. *Fig.1* displays state trajectory of (7) and its xyz phase portrait diagram is displayed in *Fig.2* in $t=250\,Sec$ with initial conditions $(0.1,-0.3,0.2)$.

5. Synchronization T-System using GBM

For synchronization, we consider master system as (8):

$$\begin{aligned} \dot{x}_1 &= a(y_1-x_1) \\ \dot{y}_1 &= (c-a)x_1-ax_1z_1 \\ \dot{z}_1 &= -bz_1+x_1y_1 \end{aligned} \tag{8}$$

And slave system by adding control inputs u_1, u_2 as (9).

$$\begin{aligned} \dot{x}_2 &= a(y_2-x_2) \\ \dot{y}_2 &= (c-a)x_2-ax_2z_2+u_1 \\ \dot{z}_2 &= -bz_2+x_2y_2+u_2 \end{aligned} \tag{9}$$

We define error between (8) and (9) as

$$\begin{aligned} e_x &= x_2-x_1 \\ e_y &= y_2-y_1 \\ e_z &= z_2-z_1 \end{aligned} \tag{10}$$

Now, by putting (10) in (8) and (9)

$$\begin{aligned} \dot{e}_x &= a(e_y-e_x) \\ \dot{e}_y &= (c-a)e_x-a(x_2z_2-x_1z_1)+u_1 \\ \dot{e}_z &= -be_z+x_2y_2-x_1y_1+u_2 \end{aligned} \tag{11}$$

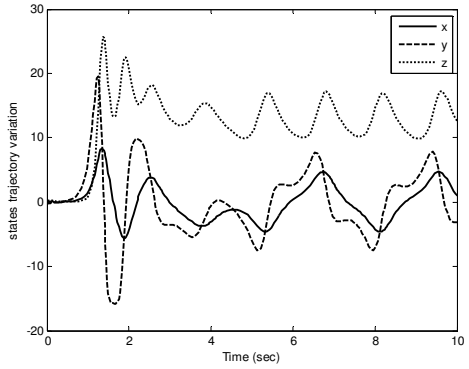


Fig. 1 *State trajectory of (7)*

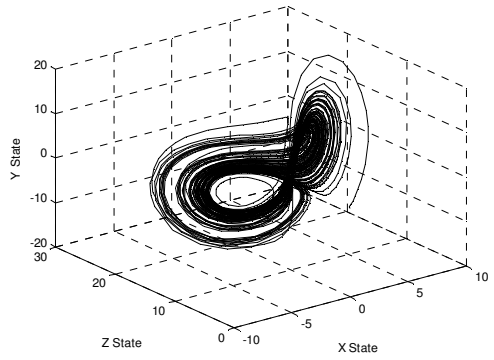


Fig. 2 *xyz phase-page diagram of (7) in* $t = 250\,Sec$

Now, based on GBM method, we consider virtual control signals as

$$\varphi_{11} = \varphi_{12} = \varphi_{21} = \varphi_{22} = 0 \tag{12}$$

Finally, according to (3), control signals for synchronization between these systems are obtained by

$$\begin{aligned} u_1 &= -[ce_x + k_{11}e_y + k_{12}e_z - a(x_2z_2 - x_1z_1)] \\ u_2 &= -[k_{21}e_y + (k_{22} - b)e_z + x_2y_2 - x_1y_1] \end{aligned} \tag{13}$$

According to (4), Lyapunov function is expressed as

$$\begin{aligned} V = \frac{1}{2}[&e_x^2 + e_y^2 + e_z^2 + (e_y - \varphi_{11})^2 + (e_y - \varphi_{12})^2 \\ &+ (e_z - \varphi_{21})^2 + (e_z - \varphi_{22})^2] \end{aligned} \tag{14}$$

Now, using genetic algorithm and according to fitness function in (6), optimize GBM controller in (13). For this purpose, we consider gains $k_{11}, k_{12}, k_{21}, k_{22}$ as genetic algorithm inputs. After optimization, the best values for these gains are obtained as

$$k_{11} = 8.7165, k_{12} = 1.9697, k_{21} = 2.127, k_{22} = 7.0108 \tag{15}$$

For master and slave systems, assume initial condition

$$\begin{aligned} (x_1(0), y_1(0), z_1(0)) &= (0.1, -0.3, 0.2) \\ (x_2(0), y_2(0), z_2(0)) &= (2.4, -3.3, 14.5) \end{aligned} \tag{16}$$

After applying GBM controller, we compare obtained results with the results of active control and backstepping controllers [28]. The states e_x, e_y, e_z are depicted in *Fig.3-5* respectively. Control signals for synchronization of these chaotic systems using GBM and Backstepping controllers has been dispalyed in *Fig.6-7* and three control signals using Active control [28] are shown in *Fig.8.*

According to GBM method, a controller was designed for synchronization. Designed controller has gains with positive values. GBM controller possesses different behaviors for each value of these gains which probably conducts system to inconstancy.

In order to find the best values for this controller, genetic algorithm was utilized. Genetic algorithm minimizes fitness function. Also this function is considered based on Total Square Error. Comparing GBM controller with Active control [28] and backstepping [28] controller, we could prove its better usefulness and effectiveness.

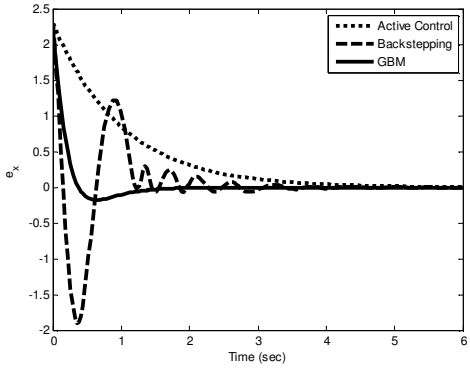


Fig. 3 *Trajectory of error* e_x

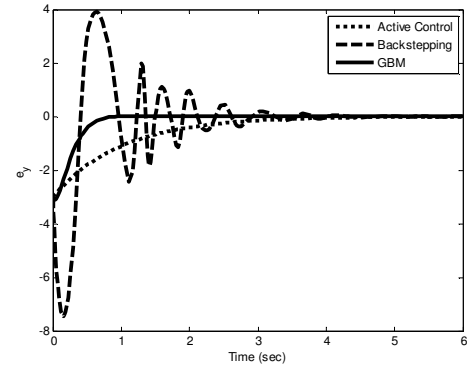


Fig. 4 *Trajectory of error* e_y

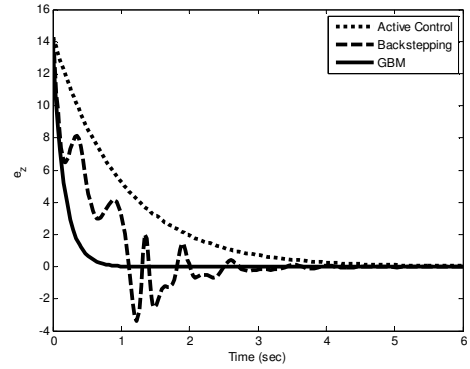


Fig. 5 *Trajectory of error* e_z

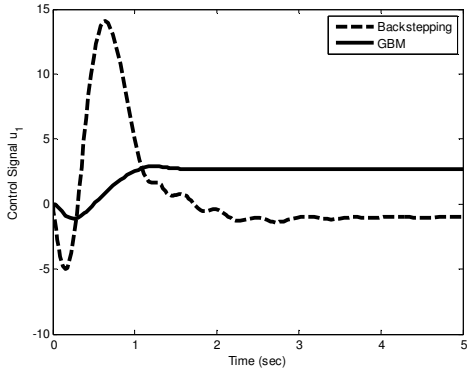


Fig. 6 *Control signal* u_1 *for synchronization using GBM and BM [28]*

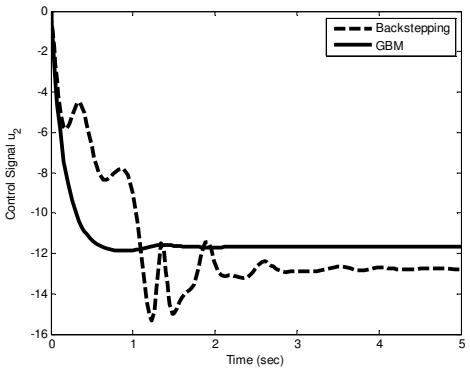


Fig. 7 *Control signal* u_1 *for synchronization using GBM and BM [28]*

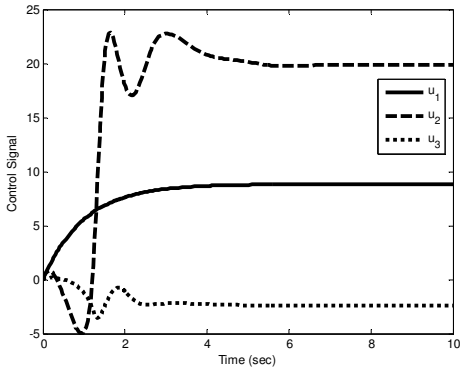


Fig. 8 *Control signals for synchronization using active control*

6. Synchronization T-System using Adaptive GBM

The parameters a,b,c in (11) are unknown and a_1,b_1,c_1 are respectively estimated values of them which are updated by

$$\begin{aligned} \dot{a}_1 &= -e_x^2 - e_y(x_2z_2 - x_1z_1) \\ \dot{b}_1 &= -e_z^2 \\ \dot{c}_1 &= e_1e_2 \end{aligned} \tag{17}$$

Now by using GBM , we consider virtual control signals as

$$\varphi_{11} = \varphi_{12} = \varphi_{21} = \varphi_{22} = 0 \tag{18}$$

Finally, according to (3), control signals are

$$\begin{aligned} u_1 &= -[c_1e_x + k_{11}e_y + k_{12}e_z - a_1(x_2z_2 - x_1z_1)] \\ u_2 &= -[k_{21}e_y + (k_{22} - b_1)e_z + x_2y_2 - x_1y_1] \end{aligned} \tag{19}$$

Now, using genetic algorithm and according to fitness function in (6), we optimize adaptive GBM controller in (19). For this purpose, we consider gains $k_{11},k_{12},k_{21},k_{22}$ as genetic algorithm inputs. After optimization, the best values for these gains are obtained as:

$$k_{11} = 9.8584, k_{12} = 1.6731, k_{21} = 7.9422, k_{22} = 8.8094 \tag{20}$$

We assume initial conditions as (16).

7. Brain Emotional Learning Based Intelligent Controller (BELBIC)

According to this method, learning is based on emotional factors such as excitement and anxiety [31-32]. In this paper, the factors that designer has sensitivity on them, are considered as stimuluses which make system disturbed and control system should decrease system anxiety versus them. BELBIC possesses some sensor inputs selected by designer. BELBIC has two states for each sensor input; amygdala and orbitofrontal output as

$$\begin{aligned} A_i &= s_iv_i \\ O_i &= s_iw_i \end{aligned} \tag{21}$$

Where s_i is i^{th} sensor input. v,w are two states depended to sensor input and calculated as follow

$$\begin{aligned} \Delta v_i &= \alpha s_i \max\left(0, rew - \sum A_i\right) \\ \Delta w_i &= \beta s_i - \left(rew - \sum A_i - \sum O_i\right) - \max(s_i) \end{aligned} \tag{22}$$

Where α,β are learning parameters. rew is reward signal selected as a linear function of system error. Control signal u is obtained as

$$u = \sum A_i - \sum O_i \tag{23}$$

8. Synchronization T-System using BELBIC

To synchronize, we consider master system as (24) and slave system by adding three control inputs as (25).

$$\begin{cases} \dot{x}_1 = a(y_1 - x_1) \\ \dot{y}_1 = (c - a)x_1 - ax_1z_1 \\ \dot{z}_1 = -bz_1 + x_1y_1 \end{cases} \tag{24}$$

$$\begin{cases} \dot{x}_2 = a(y_2 - x_2) + u_1 \\ \dot{y}_2 = (c - a)x_2 - ax_2z_2 + u_2 \\ \dot{z}_2 = -bz_2 + x_2y_2 + u_3 \end{cases} \tag{25}$$

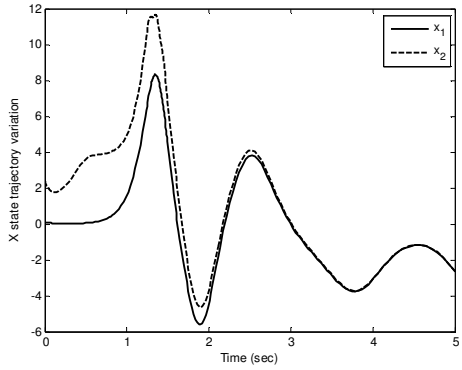


Fig. 9 *Trajectory of state* x

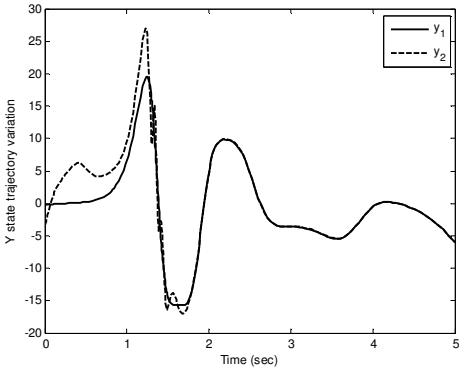


Fig. 10 *Trajectory of state* y

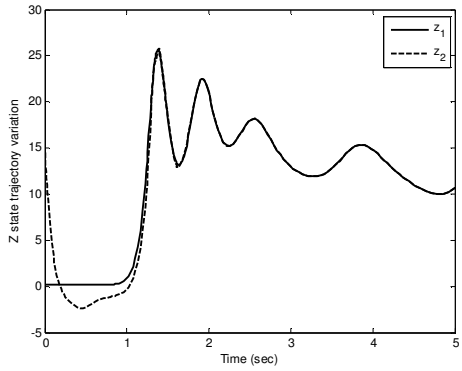


Fig. 11 *Trajectory of state* z

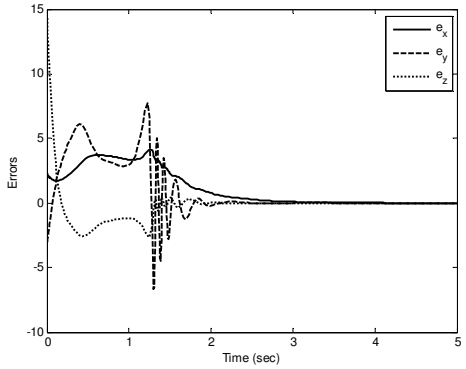


Fig. 12 *Error trajectory between slave and master systems*

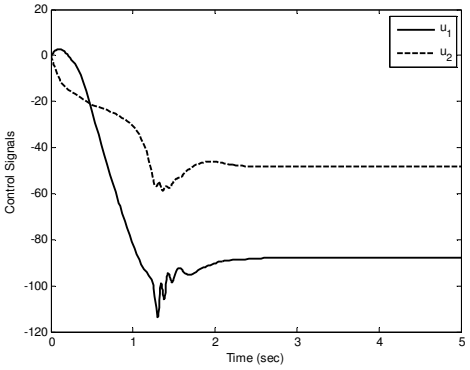


Fig. 13 *Control signals for synchronization*

We define error between (24) and (25) as

$$\begin{cases} e_x = x_2 - x_1 \\ e_y = y_2 - y_1 \\ e_z = z_2 - z_1 \end{cases} \tag{26}$$

Now, Sensor input for BELBIC and reward signal for each control signals u_1, u_2, u_3 are selected as (27-28) and parameters α, β are equal to 1 and 3 respectively and initial conditions as (16).

$$s_i = [e_1; e_2; e_3] \tag{27}$$

$$rew_i = [4e_1 + 4; 4e_2 + 4; 2e_3 + 7] \tag{28}$$

After using BELBIC, we compare the results with the results obtained by Active control and Backstepping [28] controllers. *Fig.14-16* display error changes between master and slave systems using BELBIC, backstepping [28] and active control [28]. Control signals of BELBIC, backstepping [28] and active control [28] for synchronization are indicated in *Fig.17-19* respectively.

9. Conclusions

In this paper, T-chaotic system was studied. Then we addressed the synchronization problem and proposed three methods for it; BELBIC, GBM and adaptive method. By comparing these methods versus active control and BM, we could prove their better usefulness. The results obtained from simulations demonstrated that BELBIC, GBM and adaptive methods synchronize system with higher speed, lower settelling time, lower overshoot and lower control cost against active control and BM.

References

1. Lorenz, Deterministic non-periodic flows, J Atmos Sci, **20**, 130–141, (1963).

2. C. Sparrow, The Lorenz equations: bifurcations, chaos and strange attractors, *New York: Springer-Verlag*; (1982).

3. G. Chen and X. Dong, From chaos to order: methodologies, perspectives and applications. Singapore: World Scientific; (1998).

4. OE. Rossler, An equation for continuous chaos, Phys Lett. A, **57**, 397–398, (1976).

5. G. Chen and T. Ueta, Yet another chaotic attractor, Int J Bifurcat Chaos, **9**, 1465–1466, (1999).

6. J. Lü and G. Chen, A new chaotic attractor coined, Int J Bifurcat Chaos, **12**, 659–661, (2002).

7. C. Liu, T. Liu, L. Liu and K. Liu, A new chaotic attractor. Chaos Solitons and Fractals, **22**, 1031–1038, (2004).

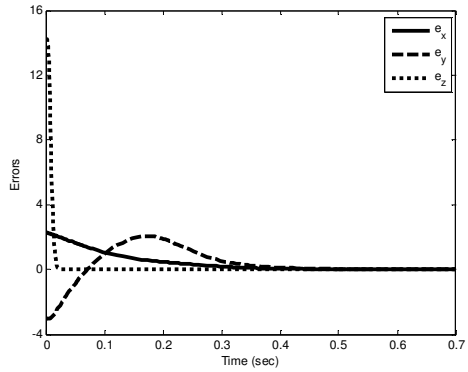


Fig. 14 *Error changes between master and slave systems using BELBIC*

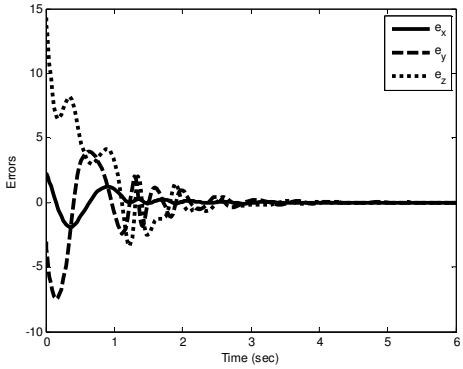


Fig. 15 *Error changes using BM [28]*

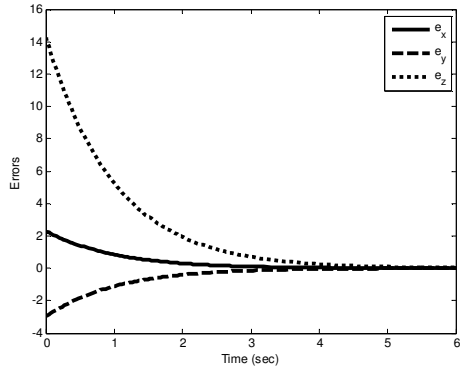


Fig. 16 *Error changes using active control [28]*

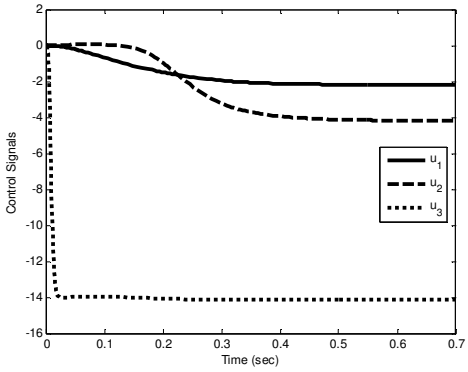


Fig. 17 *Control signals for synchronization using BELBIC*

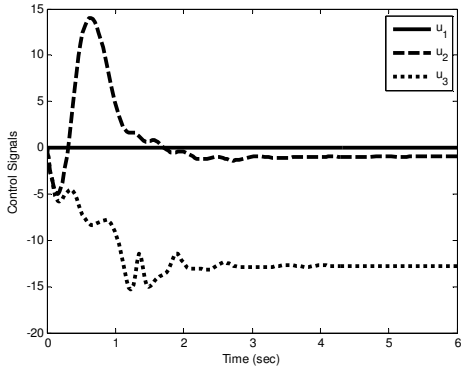


Fig. 18 *Control signals for synchronization using backstepping [28]*

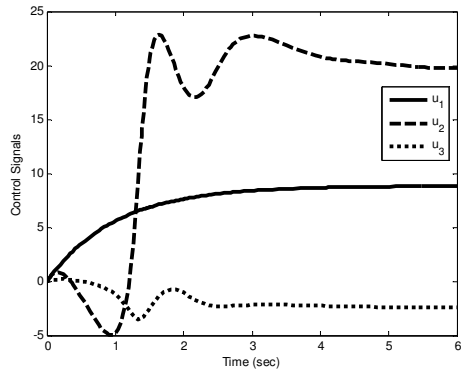


Fig. 19 *Control signals for synchronization using active control [28]*

8. G. Qi, G. Chen, et al. Analysis of a new chaotic system, Physica A, **352**, 295–308, (2005).

9. L. Liu, Y. Su, et al. A modified Lorenz system, Int J Nonlinear Sci, **7**, 187–191, (2006).

10. G. Qi, G. Chen and Y. Zhang, On a new asymmetric chaotic system. Chaos, Solitons and Fractals, **37**, 409–423, (2008).

11. G. Qi, Chen G., et al. A four-wing chaotic attractor generated from a new 3-D quadratic autonomous system. Chaos, Solitons and Fractals, 38:705–21(2008).

12. G. Tigan, Analysis of a dynamical system derived from the Lorenz system. Sci Bull Politehnica Univ. Timisoara, **50**, 61–72, (2005).

13. G. Tigan and O. Dumitru, Analysis of a 3D chaotic system, Chaos, Solitons and Fractals, **36**, 1315–1319, (2008).

14. LM. Pecora and TL., Carroll Synchronization in chaotic systems, Phys Rev Lett, **64**, 821–824, (1990).

15. TL. Carroll and LM. Pecora, Synchronizing chaotic circuits, IEEE Trans Circ Syst. I, **38**, 453–456, (1991).

16. Cuomo and AV.Oppenheim, Circuit implementation of synchronized chaos with applications to communications, Phys Rev Lett, **71**, 65–68, (1993).

17. G. Perez and H. Cedeira, Extracting messages masked by chaos, Phys Rev Lett, **74**, 1970–1973, (1995).

18. T. Liao and N. Huang, An observer-based approach for chaotic synchronization with applications to secure communications, IEEE Trans Circ Syst I, **46**, 1144–1150, (1999).

19. S. Boccaletti, J. Kurths, et al, The synchronization of chaotic systems, Phys Rep, **366**, 1–101, (2002).

20. F. Wang and C. Liu, A new criterion for chaos and hyperchaos synchronization using linear feedback control, Phys Lett A, **360**, 274–278, (2006).

21. MT. Yassen, Adaptive control and synchronization of a modified Chua's circuit system, Appl Math Comput, **135**, 113–128, (2003).

22. C. Wang and S. Ge, Adaptive synchronization of uncertain chaotic systems via backstepping design, Chaos, Solitons and Fractals, **12**, 1199–1206, (2001).

23. Y. Yu, S. Zhang, Adaptive backstepping control of the uncertain Lü system, Chin Phys, **11**, 1249–1253, (2002).

24. F. Wang and C. Liu, Synchronization of unified chaotic system based on passive control, Physica D, **225**, 55–60, (2007).

25. J. Yan, M. Hung, et al. Robust synchronization of chaotic systems via adaptive sliding mode control, Phys Lett A, **356**, 220–225, (2006).

26. A.R. Sahab, and M. Haddad Zarif, Chaos Control in Nonlinear Systems Using the Generalized Backstopping Method, American J. of Engineering and Applied Sciences, **1** (4): 378-383, (2008).

27. Ali Reza Sahab and Mohammad Haddad Zarif, Improve Backstepping Method to GBM, World Applied Sciences Journal **6** (10): 1399-1403, (2009).

28. Yue Wu, Xiaobing Zhou, Jia Chen, Bei Hui, Chaos synchronization of a new 3D chaotic system, Chaos, Solitons and Fractals, **42**, 1812–1819, (2009).

29. Ali Reza Mehrabian and Caro Lucas, Emotional Learning based Intelligent Robust Adaptive Controller for Stable Uncertain Nonlinear Systems, International Journal of Computational Intelligence, **2** (4), (2005).

30. Ali Reza Mehrabian, Caro Lucas, Jafar Roshanian, Aerospace launch vehicle control: an intelligent adaptive approach, Aerospace Science and Technology, **10**, 149–155, (2006).

31. Saeed Jafarzadeh, Rooholah Mirheidari, Mohammad Reza Jahed Motlagh, Mojtaba Barkhordari, Designing PID and BELBIC Controllers in Path Tracking Problem, Int. J. of Computers, Communications & Control, *Proceedings of ICCCC*, 343-348,(2008).

32. Saeed Jafarzadeh, Rooholah Mirheidari, Mohammad Reza Jahed Motlagh, Mojtaba Barkhordari, Intelligent Autopilot Control Design for a 2-DOF Helicopter Model, Int. J. of Computers, Communications & Control, *Proceedings of ICCCC*, 337-342, (2008).

33. Z. Michalewicz, Genetic Algorithm+Data Structures=Evolution Programs, 2nd Edition, Springler Verlag (1994).

34. Ali Reza Sahab, Masoud Taleb Ziabari, Seyed Amin Sadjadi Alamdari, Chaos Control via Optimal Generalized Backstepping Method, International Review of Electrical Engineering (I.R.E.E.), **5**(5), 2129-2140, (2010).

DEVELOPMENT, MANUFACTURING AND INTRODUCTION OF NEW CONSTRUCTIVE SOLUTION OF TRANSMISSION MECHANISM

РАЗРАБОТКА, ИЗГОТОВЛЕНИЕ И ВНЕДРЕНИЕ НОВОГО КОНСТРУКТИВНОГО РЕШЕНИЯ ПЕРЕДАТОЧНОГО МЕХАНИЗМА.

Conf. dr. eng., Prof. Abdullayev A.[1], Conf. dr. eng., Prof. Najafov A.[1], dr.eng, Ahmedov B.[1],
dr.eng Gasimov R.[1], dr.eng. Mirzoyev H.[1]
[1]Department of Machine Parts – Azerbaijan Technical University, Baku, Azerbaijan, email: ali.najafov@rohe.az

Abstract: *It was developed, studied, manufactured and tested new designs of multistage gearboxes on the two shafts with cylindrical gears, providing virtually unlimited value ratios. This reduces metal consumption, improved reliability and efficiency by the eliminating in the mechanical system of the intermediate shafts and their support units, to provide a set of agreed most effective technical solutions and create new machines and units at the level of the best world samples*
KEYWORDS*: TRANSMISSION MECHANISM, PACKET GEAR, SCHAFT SPEED*

1. Introduction.

Gear reducers are widely used in machines and units in almost all branches of modern engineering.

The use of low-power and high speed electric motor drives, allowing to reduce energy consumption as a whole, and by the extreme operating conditions of machines and units depends on the number of stages and gear ratio value of gear reducers.

Therefore it is very important to finding the most efficient kinematic scheme of multi-gear reducers, taking into account not only the external (consumer) characteristics, but also its cost [1-3].

The department "Machine parts" of Azerbaijan Technical University developed, studied, manufactured and tested new designs of multistage gearboxes on the two shafts with cylindrical gears, providing virtually unlimited value ratios, which originality was confirmed by the Eurasian patent. This reduces metal consumption, improved reliability and efficiency by the eliminating in the mechanical system of the intermediate shafts and their support units, to provide a set of agreed most effective technical solutions and create new machines and units at the level of the best world samples [4-7]

To confirm the theoretical assumptions were made laboratory working model of a new constructive solution to single-threaded five-step gearbox with a total transmission ratio $U_{\Sigma}=243$ (Fig. 1)

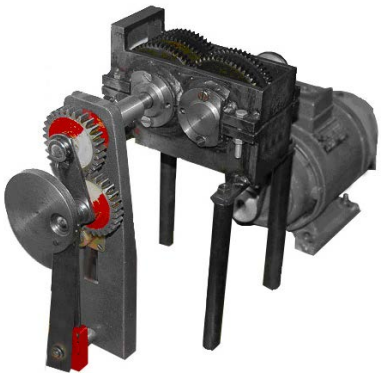


Fig. 1. *Laboratory sample of the new constructive solutions of three-stage cylindrical gear reducer with a gear ratio $U_{\Sigma}=243$*

A distinctive feature of the proposed gear is that all the intermediate shafts are eliminated in this mechanical system, in all stages drive and driven gears are the same size, that it provides increased reliability and manufacturability. The structure of the gear working as a coaxial transmission mechanisms includes, freely rotated on the driving and driven shafts, one three and two double corona gears, mounted in the form of a "packet". The rotation direction of three and double corona gears wherein respectively coincide with the rotation direction of the driving and driven shafts. Due to the specific useful direction of the friction force of lubricating fluids on the cylindrical and side surfaces of the structural pars of “packet” gear its efficiency is increased up to 8%, and thus achieved a reduction of electricity consumption.

The proposed transmission gears in the future called "packet reducers" that has been recognized in several international conferences [8, 9].

Further, according to initial data of the drive rod pumps and based on normative requirements for water wells depth of 40 m and an oil well to a depth of 1,500 m (for sucker-rod pump SKD3-1,5-710) have been designed, manufactured and successfully industrially tested two double-flow three-stage cylindrical gear reducers on two shafts, with the transmission ratio $U_{\Sigma}=64$ (Fig. 2, 3).



Fig. 2. *Mechanical drive rod pumps for water wells depth of 40 meters with a new constructive solution double-flow three-stage cylindrical gear reducer with a gear ratio $U_{\Sigma}=64$.*



Fig.3. *Mechanical drive rod pumps for oil well depth of 720 meters in relation to the SKD 3-1,5-710 with the new double-flow constructive three-stage cylindrical gear reducer $U_{\Sigma}=64$.*

2. Methods

For the using in mechanical drives of machines and units of relatively high-speed and low power consumption electric motors significant practical importance has the evaluation of critical rotational speed of the drive shaft of the new constructive solutions of three-stage double-flow "packet gear".

We consider the drive shaft gear batch on two bearings with a rotating speed $n_1^{"}$. The drive shaft is represented as a stage rotor with a fixed gear and symmetrically arranged double corona gears rotating around its geometric axis and downloaded randomly distributed masses and moments of inertia [10].

Approaching of the shaft rotation frequency to the critical can be dangerous, so the rotation frequency from $0,7n_{kr}$ to $1,3n_{kr}$ not recommended for the operating modes of packet gear. In this connection, in all cases it is desirable to provide an operation of packet gear with a rigid drive shaft and $n<0,7n_{kr}$.

To check the reliability of the basic scientific statements made numerical experiment – calculation of the drive shaft of two-stage double-flow packet gear for the sucker-rod pumps SKR3 and SKDR with the following input data:

- Nominal torque at the output shaft T^{*}=7100Nm;
- Actual gear ratio of the reducer $u_{\Sigma}=64$, the gear ratio of one stage of package reducer $i_n=4$;
- Output shaft diameter $d^{'}$=90 mm;
- Based on design reasons the diameter of input shaft on its mid taken d_1=0,5$d^{'}$=45 mm; thereafter d_2=40 mm; d_3=40 mm; d_4=35 mm;
- Diameter of the initial circle of gear d_{w1}= 117 mm;
-Coefficient characterizing the ratio of the width of the respective stages of the output shaft ν=0,5;
- Torsion stress of the output shaft $[\tau]_k$=40 Mpa.

The first approximation for the critical speed of the drive shaft is determined according to the formula

$$n_{kp}=C\left(\frac{y_{(0)}}{K_{y(0)}}\right)^{\frac{1}{2}}\Bigg|_{x=\frac{1}{2}}=9{,}55\left(\frac{1}{367{,}2773}\right)^{\frac{1}{2}}10^4=4983{,}18,\quad rpm$$

Recommended rotation frequency of the drive shaft of packet reducer

$$n<0,7n_{kr}=3488{,}23\ rpm$$

Where

$$y(0)=-\frac{1}{L}\int_0^L\int_0^{x_1}\frac{M(x_2)}{EJ(x_2)}dx_2dx_1-\frac{x}{L}\int_0^L\int_0^{x_1}\frac{M(x_2)}{EJ(x_2)}dx_2dx_1$$

$$K_y=\left|\int_0^L\int_0^{x_1}\frac{A_y(x_2)}{EJ(x_2)}dx_2dx_1-\frac{x}{L}\int_0^L\int_0^{x_1}\frac{A_y(x_2)}{EJ(x_2)}dx_2dx_1\right|$$

M(x)- discrete mass, *EJ(x)*- stiffness of the shaft section in bending.

3. Conclusion and results

1. Compared with the existing multi-stage cylindrical gears classical performance in the proposed new designs of multi-stage packet gearboxes operational and technological parameters (reliability level increased up to 8%, efficiency - up to 9%, metal content reduced up to 30%) are improved.

2. A new analytical expression to determine of critical rotational speed of the drive shaft of the new constructive solutions of three-stage double-flow "packet gear" have been improved, which has undoubted practical value by the using of low-power motor with high rotational speed of the drive shaft *n*=3000 rpm.

3. Kinematic and design features of packet gear boxes allow to obtain the minimum value of the output shaft speed (n=1 rev/day), which enabled their widespread use in the mechanical drives of monitoring systems and radars.

References

1. Bolotin V.V. Recourse of machines and structures. – M, Engineering, 1990, 446 p.
2. Adonin A.N. Oil extraction with sucker rod pumps.- M., Nedra, 1979, 213 p.
3. Molchanov G.V., Molchanova A.G. Machines and equipment for oil and gas extraction. - M, Nedra, 1984, 464 p.
4. Abdullayev A.I., Najafov A.M., Qasimov R.M. «Mechanical drive of sucker rod pumps». Patent of Eurasian Patent Organization № 012103, F04B 47/02, Moscow, 2009.
5. Abdullayev A.I., Najafov A.M. «Three-stage double – flow gear reducer». Patent of Eurasian Patent Organization № 07053, F04B 47/02, Moscow, 2012.
6. Abdullayev A.I., Najafov A.M. «Qualitative assessment of technical level of packet gears» // Journal of Engineering, Moscow, №12, 2008, pp. 6-9.
7. A.M. Najafov, A.I. Abdullayev. "Optimizing Modular Gears in the Mechanical Drive of Beam Pumps". / Russian Engineering Research, New-York, USA, 2009, Vol. 29, №1, pp.7-9, ISSN 1068-798 X.
8. Abdullayev A.I., Davidov G.Sh., Najafov A.M., Hamidov N.R. Establishment and evaluation of technical level of packet gear. Сбор. докл. Межд. Конгр. «Mechanics and tribology of traffic systems 2003», Rostov on Don, 2003, pp. 14-17.
9. A.M. Najafov, A.I. Abdullayev. "The new constructive decision of a mechanical drive of sucker-rod pumps". / Int. Symp. on Engineering & Architectural Sciences of Balkan, Caucasus & Turkish Republic, 22.-24.10.2009, Isparta/Turkey, Vol.2, pp.88-93.
10. Birger I.A., Shorr B.F., Iosilevitch G.B. Calculation of the strength of machine parts. – M, Engineering, 1990, 446 p.

INCREASING THE RESISTANCE OF PRECISION INSTRUMENT-MAKING ELEMENTS FROM OPTICAL GLASS TO EXTERNAL THERMO-INFLUENCES BY PRELIMINARY ELECTRON-BEAM PROCESSING OF SURFACES

ПОВЫШЕНИЕ СТОЙКОСТИ ЭЛЕМЕНТОВ ТОЧНОГО ПРИБОРОСТРОЕНИЯ ИЗ ОПТИЧЕСКИХ СТЕКОЛ К ВНЕШНИМ ТЕРМОВОЗДЕЙСТВИЯМ ПУТЕМ ПРЕДВАРИТЕЛЬНОЙ ЭЛЕКТРОННО-ЛУЧЕВОЙ ОБРАБОТКИ ИХ ПОВЕРХНОСТЕЙ

Associate Professor Ph.D. Yatsenko I.[1], Professor dr. eng. Antonyuk V.[2], senior researcher dr. eng. Kyrychenko O.[3], Professor dr. eng. Vashchenko V.[4], senior lecturer Tsybulin V.[4]
Department of Electrotechnical Systems[1], Department of Physics[4] - Cherkassy State Technological University, Ukraine
Faculty of instrument-making[2], National Technical University of Ukraine "Kiev Polytechnic Institute", Ukraine
Department of organization of technogenic-prevention work and health safety[3] - Cherkassy Institute of Fire Safety named after Heroes of Chornobyl of National University of Civil Protection of Ukraine, Ukraine

Abstract: *The results of experimental studies to improve the properties of the surface layers of the elements of optical glass (K8, K108, K208, BK10, TF110) after their processing by mobile electron beam with density of heat exposure $F_n = 7 \cdot 10^6 \ldots 8 \cdot 10^8$ W/m^2 and displacement speed $V = 5 \cdot 10^{-3} \ldots 5 \cdot 10^{-2}$ m / s (a reduction of residual microroughness height at the surface from 4 ... 6 nm (unprocessed elements) to 0.5 ... 1 nm (processed elements), the occurrence of melted layers of thickness up to 250 ... 300 microns with a modified structure, which is close to the quartz glass) are presented. It was found that the improvement of these properties increases the resistance of elements to external-heat: an increase in 1.3 ... 1.7 times of the critical value of external heat fluxes and the time of their exposure, the excess of which leads to the destruction of elements and damage to the test instrument turndown external pressure $10^5 \ldots 10^7$ Pa; increasing the maximum permissible values of thermal stress in the elements from 20 ... 40 MPa to 90...100 MPa heating temperatures 300 ... 1200 K;an increase of the probability of failure-free operation in the 2 ... 2.5 times by increasing the speed of the external heating from 100 K / s to 400 K / s.*

KEY WORDS: *optical glass, electron beam, elements of precision instrument-making*

1. Introduction

Modern devices with elements of optical glass (K8, K108, BK 10 and so on) for measuring and thermal control of different physical nature objects (flat plates and discs as optical integrated circuit substrates, aerophoto lenses and plates of double curvature for space mirrors and aerospace applications, the input protective windows and lenses in sight for observation in the visible and infrared regions of the spectrum, optical fibers on optical monofilaments in laser medical devices for the diagnosis and treatment and so on) in operating conditions are exposed to intense external-heat (higher heating temperature and external pressure, shock thermal and mechanical stress in a shot and the flight, etc.) [1 - 3]. Under these conditions, a change in the properties of the surface layers of the optical elements up to their destruction (cracking and chipping, deep surface melting to form a sagging, undulating surfaces, changing the geometrical shape and others defects) takes place and leads to significant deterioration of the technical-operational characteristics of devices and their failure.

Therefore, the prevention of forced destruction of the optical elements of the instrument gets a significant importance in terms of their operation, taking into account the impact of external-heat.

As shown by experimental studies of various authors [4 - 8], in order to prevent the destruction of optical elements the electron-beam methods of finishing processing their work surfaces have the practical value at the manufacturing stage, and allow to improve the properties of the surface layers of elements and thus make them more resistant to external-heat, improving basic technical and operational characteristics of devices (reliability, service life and so on). However, studies of thermal exposure of the electron beam to change the properties of the surface layers of optical glass elements are currently insufficiently investigated. Therefore, the aim of this work is to prevent the destruction of optical glass elements of instruments for measuring and thermal control objects of different physical nature by improving the properties of the surface layers of the elements and increasing their resistance to external-heat by electron-beam processing.

2. Results and discussion

As a result of experimental studies they established the following optimal ranges of electron beam parameters: $F_n = 7 \cdot 10^6 \ldots 8 \cdot 10^8$ W / m^2, and $V = 5 \cdot 10^{-3} \ldots 5 \cdot 10^{-2}$ m / s, within which there is the most significant improvement of the properties of the surface layers of the optical elements (more than in a few times).

The results of electron microscopic examination of the surface of the optical glass elements made it possible to establish that on their surfaces after machining there are such heterogeneity as scratches, cracks and unevenness, the number of which is markedly reduced after electronic processing. In addition, the surface of elements has unevenness and defects which are a result after mechanical polishing, and which are virtually absent after electron beam processing. On the unprocessed by electron beam surface portion of elements there are characteristic etch pits defect layer, while on the processed part of the surface there are much less or practically absent.

In the study of fracture surfaces (fracturegramm) of optical glass elements before and after electronic processing they revealed that the nature of the fracture is different. It is found that a fine-grained fracture occurs in the processed layer. In he elements that are exposed to the electron beam, there is a fine-grained fracture. The individual small crystals are found on the surface of the parent element. Furthermore, the nature of electron diffraction on the microdiffractureg raphs indicates crystal hexagonal structure of inclusions.

The analysis of transverse sections, chips, fractures of optical glass elements after mechanical polishing and electronic processing shows that: a clear boundary between the processed surface by electron beam and the very foundation of the element material is not observed; there is a significant difference between sides of the element - processed and unprocessed; there is a modification of the surface structure to the depth of 200 ... 220 microns with its most significant change in the sintered layer with the elements of "viscous" destruction.

The results of studies of optical glass elements surfaces by electron microscopy scanning showed that on the surface after

machining, the most characteristic there is a presence of various microroughnesses - small cracks of the depth up to 0.1 ... 0.7 microns, thin scratches up to 2 ... 5 microns, as well as "tubercles" bubbles etc., a size of which 10^{-3}...10^{-2} microns. After electron-beam processing bubble sizes (diameters) on the elements surface are reduced in 2 ... 4 times, therefore " tubercles " and other unevenness of less than 1 ... 2 microns are not observed, that is in result of processing by electron beam the elements surface, as it were "cleaned", small defects are eliminated.

The analysis of electron-microscopic images of the surfaces of optical glass elements, the study of surfaces of the polished sections of chipped elements before and after electron beam processing indicates that in the first case the microroughness height is 30 ... 40 nm, and in the second one it is reduced to the level of 0,5 ... 6 nm.

The study of fracturegramms of optical glass elements surface layers before and after electronic processing showed that the depth of main-heat zone or the thickness of the deposited layer can be up to 250 ... 300 microns, and essentially depends on the magnitude F_n and the moving speed V of the electron flow (Fig. 1, 2). Thus, an increase of F_n from $7 \cdot 10^6$ W/m^2 to $8 \cdot 10^8$ W/m^2, when used in practice the electron flow moving speed $V = 5 \cdot 10^{-3}$ m/s leads to increasing depth of fusion from 50 microns to 230 microns for elements from optical glass K8; from 30 microns to 150 microns for elements from optical glass K108; from 25 microns to 140 microns for elements from optical glass K208; from 30 microns to 180 microns for elements from optical glass BK10; from 40 microns to 170 microns for elements from optical glass TF110. And an increase in the electron beam moving speed from 10^{-3}m/s to 10^{-2} m/s, when used in practice of F_n values already leads to a reduction of the melting depth: from 200 microns to 70 microns for elements from optical glass K8; from 160 microns to 40 microns for elements from optical glass K108; from 130 microns to 30 microns for elements from optical glass K208; from 170 microns to 80 microns for elements from optical glass BK10 and from 160 microns to 40 microns for elements from optical glass TF110.

A detailed study of scans of sections of the surface of optical glass elements after electronic processing indicates a local smoothing of irregularities, a significant dependence of the surface shape of the processing modes. So, with a deep reflow (200 ... 250 microns) it is observed a well-defined wavy surfaces. This modified melted layer has clearly oriented structure on melting depth.

The layers, formed by electron beam on the optical elements surface are modified to different degrees in chemical composition. Thus, the analysis of change in the elemental composition of the surface of elements of optical glass K8, K108, K208, conducted with the help of the wave dispersion spectrometer, showed a decrease of Na and O concentration, an increase of Si concentration and the constant K concentration. At the same time, by X-ray analysis on the example of untreated and treated by electron beam elements of the optical glasses BK10, TF110 it is shown that significant quantitative changes in the chemical composition of its surface are not observed, however, it is possible to make a conclusion as for the improvement of the homogeneity of the distribution of elements in micro-surface layer after electronic processing .

In the result of conducted researches, it was found that after electron beam pre-treatment of the optical elements an increase comes in the critical values of the external heat flows q_n^* and their impact time t^* in 1,5…2 times (Fig. 3).При этом увеличение внешнего давления до 10^7 Па приводит к увеличению значений q_n^* и t^* только в 1,4…1,5 раза. The increase in external pressure up to 10^7 Pa leads to reduction in the values q_n^* and t^* only in 1.4 ... 1.5 times.

In addition, it was also shown that the limit values of thermoelastic stresses $\sigma^*(T)$ at different temperatures for heating the optical elements treated by electron beam in 1.7 ... 2.3 times higher than for untreated elements (Fig. 4).

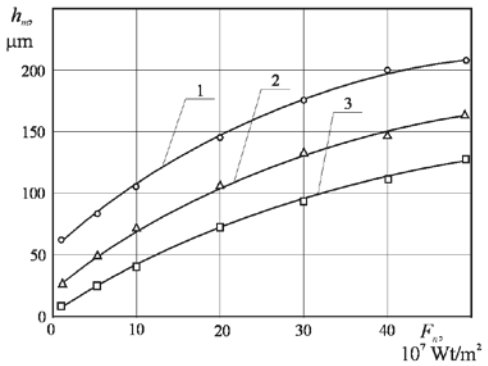


Fig. 1. The dependence of the thickness of melted layers in the elements of optical glass K8 (1), K108 (2) and K208 (3) on the density of the thermal effects of the electron beam ($V = 5 \cdot 10^{-3}$ m / s): Δ, ○, □ - experimental data.

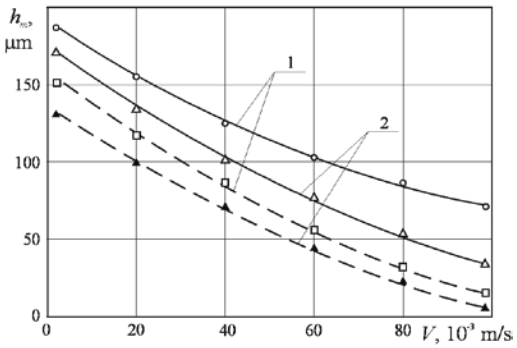


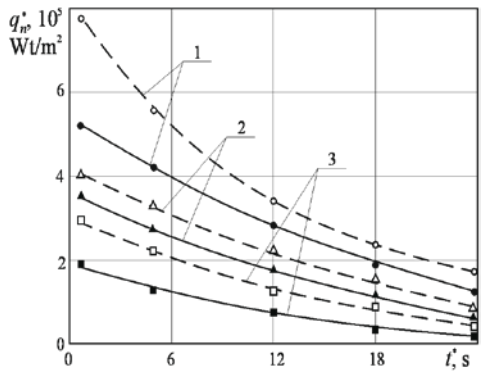
Fig. 2. The dependence of the thickness of melted layers in the elements of the optical glasses BK10 (1) and TF110 (2) on the moving speed of the electron beam: ——— – $F_n = 5 \cdot 10^8$ W / m^2; – – – – – $F_n = 7 \cdot 10^6$ W / m^2; Δ, ○, □, ▲ - experimental data.

The tests of the optical elements under conditions of alternating external heating, which simulates actual operating conditions of the optical devices with the influence of external-heat showed that in the case of an electron beam-treated elements it is observed in 2 ... 2,5 times less of their destruction and failure of devices on their basis than for untreated elements (Table. 1).

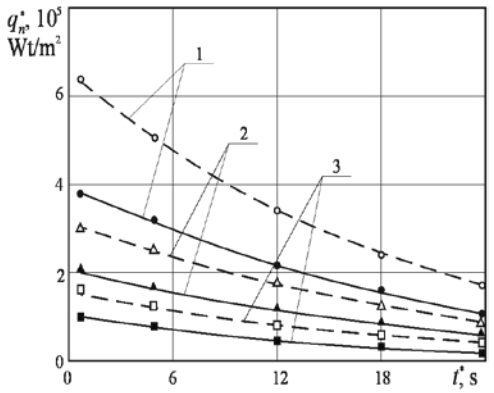
The safety factor as a measure of efficiency of the optical device at a predetermined heating rate $V_н$ (or time t, which is given to the test at a controlled heating temperature) is determined by the following formula [8]:

$$W(V_н) = 1\text{-}N(V_н) / N_0, \qquad (1)$$

where $W(V_н)$ - probability of preservation of working capacity of the device of sighting system under external thermal effects; $N(V_н)$) - the number of devices that fail at a heating rate $V_н$ (the destruction of the optical element is taken as the failure of the device as a whole); N_0 - the total number of devices that are tested.



a)



б)

Fig. 3. The dependence of the critical values of the external heat flows q_n^* from the time of their exposure t^* on the elements of optical glass K8 (1), TF110 (2) and BK10 (3) for a variety of external pressures (the thickness of the element $H = 10^{-2}$ m): a) – $P = 10^5$ Pa; b) – $P = 10^7$Pa; ——— – elements which are not processed by electron beam; – – – – processed items; ●, ○, Δ, ▲, □, ■ - experimental data.

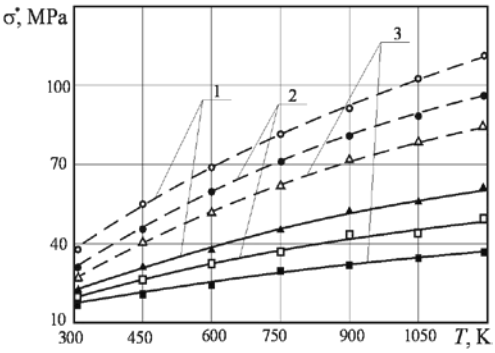


Fig. 4. The dependence of the value of the maximum allowable thermal stresses in the elements of the optical glass K8 (1), TF110 (2) and BK10 (3) on the heating temperature ($P = 10^5$ Pa, element thickness $H = 10^{-2}$ m, $F_n = 1{,}5\cdot10^7$ W/m^2, $V = 5\cdot10^{-3}$ m/s): ——— – elements that are not treated by electron beam; – – – – processed items; Δ, ○, □, ▲, ■, ● - experimental data.

From the formula (1) it follows that with increasing heating rate of the devices of the suggested devices (e.g., from 100 K/s to 400 K/s) leads to decrease in the probability of trouble-free operation under external-heat terms in 4.9 times; while in the case of input windows which are pre-treated by electron beam, the probability of trouble-free operation of devices increases in 2,3 times (Fig. 5).

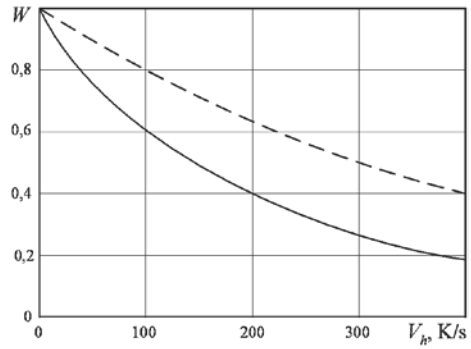


Fig. 5. The dependence of the probability of trouble-free operation of sighting devices complexes under conditions of external-heat from an external heat rate of their input protective windows: ——— – – the input windows that are not processed by electron beam; – – – – the input windows, the outer sides of which are processed by electron beam (beam parameters $F_n = 5\cdot10^8$ W/m^2, $V = 5\cdot10^{-3}$m/s).

Table 1

The influence of electron beam processing of working surfaces of the elements in the form of plates of optical glass K8 on the dependence of the relative amount of their damages (k) from the heating rate *)

Input protective window / External heating rate, K/s	k, %	
	unprocessed by electron beam	processed by electron beam
100…150	40…50	20…30
150…200	50…60	30…40
200…300	60…70	40…50

*) Note. $k = k_p/k_0$, where k_0, k_p - a total number of test elements and the number of exposed to fracture respectively.

It is shown that the use of the results in the design and manufacture of new instruments, as well as the modernization of serial devices to considered optical elements for measuring and thermal control of the objects of different physical nature (optical integrated circuits substrates, aerophoto lenses, laser sights for observation in the visible and infrared regions of the spectrum , laser medical devices etc.) allows to improve basic technical characteristics (the reliability, service life and durability) when used in accordance with the influence of external-heat, for example during storage or transport under the conditions of occurrence of high-temperature fire sites, as well as the design of products with infrared devices in a shot and the flight (external thermal shock effects and others).

3. Conclusions

1. It was found that after the pre-treatment of the working surfaces of the elements of optical glass (K8, K108, K208, BK10, TF110) by mobile electron beam for change ranges of its settings (density of the heat effect $F_n = 7\cdot10^6\ldots8\cdot10^8$ W/m^2 speed of its movement $V = 5\cdot10^{-3}\ldots5\cdot10^{-2}$m/s) the basic properties of the surface layers are improved:

– after electron beam processing the surface of elements are completely cleared of defects, which were obtained by the mechanical polishing (fine cracks sized 0.1 ... 0.7 microns, long thin scratches 2 ...5 microns and other defects in size 10^{-3}...10^{-2} microns); thus there is a smoothing of irregularities, substantial dependence of the surface shape from the processing modes (with deep reflow (up to 200 ... 250 microns) a well-defined wave-like surface is observed, and the modified melted layer has clearly oriented structure for melting depth);

– the electron-beam processing of the elements of optical glass by melting leads not only to homogenization of the surface, but also to oriented restructure near the surface of the silicon-oxygen grid, which is becoming close to the quartz glass structure, which considerably increases the resistance of the elements to external-heat;

– the depth of the main-heat zone or the thickness of the melted layer can reach 250 ... 300 microns and essentially depends on the density of heat exposure of the beam F_n and its moving speed V: for example, increasing F_n from $7\cdot10^6$ W/m^2 to $5\cdot10^8$ W/m^2 and decreasing V from $5\cdot10^{-3}$ м/с до $5\cdot10^{-2}$s leads to an increase in depth of melting from 20…60 microns to 130…220 microns.

2. It was found that improvement of the properties of the surface layers of the optical elements after electron beam processing leads to increase their resistance to external-heat:

– increase in 1.5 ... 2 times the critical values of the external heat flows and times of their effects that lead to destruction of elements; thus increasing the external pressure from 10^5 Pa to 10^7 Pa reduces the critical values of these parameters in 1,3 ... 1,4 times;

– increase in 1.7 ... 2.3 times the value of the maximum permissible thermal stress in the optical elements processed by

electron beam, to change the heating temperature range 300 ... 1200 K.

3. It was found that electron beam pre-treatment of plates of optical glass used in the devices for measuring and thermal control of objects of different physical nature, reduces the amount of damage in the 2 ... 2.5 times and increases the probability of failure-free operation in 1.9 ... 2.3 times under variable external heating conditions.

3. References

1. Vashchenko V. A., Kotelnikov D. I., Lega Y. G., Krasnov D. M., Yatsenko I. V., Kirichenko O. V. Teplovye protsesy pri elektronnoi obrabotke opticheskich materialov i ekspluatatsii izdelii na ich osnove (Thermal processes in the electronic processing of optical materials and use of products based on them) Kiev: Naukova Dumka, 2006, 368 p.
2. Vashchenko V. A., Yatsenko I. V., Lega Y. G., Kirichenko O. V. Osnovy elektronnoi pbrobky vyrobiv z optychnych materialiv (The basics of electronic processing of optical materials) Kiev: Naukova Dumka, 2011, 562 p.
3. Bochok P. M., Budko N. P., Vashchenko V. A., Kanasewich G. V., Kotelnikov, D. I. Spetsialni metodu obrobky optychnogo skla. Navchalnyi posibnyk (Special methods of processing optical glass. Tutorial) Chernihiv: Chernihivskiy derzhavnyi technologichnyi Universitet, 2001, 215 p.
4. Dudko G. V., Kulov, S. K., Rose Y. A., Maksimova N. G. Issledovanie elektronno-luchevych protsessov v sozdanii bazovych technologii ELEFP (Investigation of electron-beam processes in the creation of basic technologies ELEPP) Electronnaya promyshlennost, 1991, Vol. 1, P. 41 – 45.
5. Vashchenko V. A., Kanashewich G. V., Dubrovskaya G. N., Kotelnikov D. I. Modifikatsiya struktury i svoystv zony termovozdeystviya pri obrabotke lentochnym elektronnym luchem opticheskich materialov (Modification of the structure and properties of the zone of heat when handling the tape with electron beam optical materials) Materials of IV All-union conference “Application of electron-ion technology in the national economy”, M.: MEI,1991.
6. Dubrovskaya G. N., Kanasewich G. V., Vashchenko V. A., Kotelnikov D. I., Yatsenko I. V. Poluchenie funktsyonalnych sloev v opticheskom stekle i keramike metodom elektronnoy obrabotki (Obtaining functional layers in the optical glass and ceramics by means of electronic processing). Collection of reports of International scientific-practical Symposium “Functional coatings on glass”, Kharkiv: NTC HFTI “Konstanta”, 2003, P. 135 – 137.
7. Vashchenko V. A., Dubrovskaya G. N., Kanashewich G. V., Pozdeev S. V. Opticheskie svoistva podlozhek OIS iz stekla posle nizkoenergeticheskoi elektronno-luchevoi obrabotki (Optical properties of substrates OIC of glass after low-energy electron-beam processing). Proceedings of the 3rd International Symposium vacuum technology and equipment, Kharkiv, 22 – 24 September 1999, P. 115 – 118.
8. Vashchenko V. A., Kirichenko O. V., Kotelnikov D. I. Optimizatsiya elektronnoi obrabotki izdelii infrakrasnoi techniki (Optimization of electronic processing of products of infrared technology) Elektronnaya obrabotka materialov. Institute of applied physics Academy of Sciences of Moldova, 2004, No. 6, P. 44 – 48.
9. State standard of Ukraine 27.002-89. Nadiinist u technitsi. Osnovni ponyattya. Terminy ta vyznachennya (Reliability in technique. Basic concepts. Terms and definitions).

ON EXPERIENCE OF MODELING OF HYDRODYNAMIC PROBLEM USING COMBINED NEURAL NETWORK AND DYNAMIC MODEL

C.Sc. Doc. Yasinskiy I.
Ivanovo State Power University – Ivanovo, Russia
e-mail: igor2266@yandex.ru

Abstract: *Solution of gas-dynamics problems containing different fine structures (shock waves, boundary layers, traces, jets, etc.) as well as areas within which the flows are described by different models of turbulence by traditional grid methods is quiet difficult. These tasks are encouraged to address, using neural network technology in the analysis and grid-analytical form by stochastic optimization. The proposed method is demonstrated on the problems of mixing jets. Numerical experiments have shown several advantages of this approach: reducing the cost of computer time, good accuracy, the connection of patchy pattern of flow in a single unit.*

Keywords: turbulence model, random search, neural network interpolation, combining simulation and dynamic models, non-grid methods for field tasks.

1. Introduction

The use of neural network technology can provide substantial assistance in solving the problems of continuum mechanics, containing different fine structures: boundary layers, shock waves, traces, separation points, the coverage of different turbulence models [1].

The essence of the proposed computing technology is convenient to demonstrate on the problems of mixing of supersonic streams. Such problems arise, for example, in developing high-power gas lasers stirring [2]. On fig.1, 2 the schemes are shown with the longitudinal and cross-reactive blowing environments and their respective designs. Obviously, the flow patterns are very complex. They include various fine structures of shock waves, boundary layers and their interaction fields. In addition, you can specify the subfields in which various semi-empirical turbulence models are preferred.

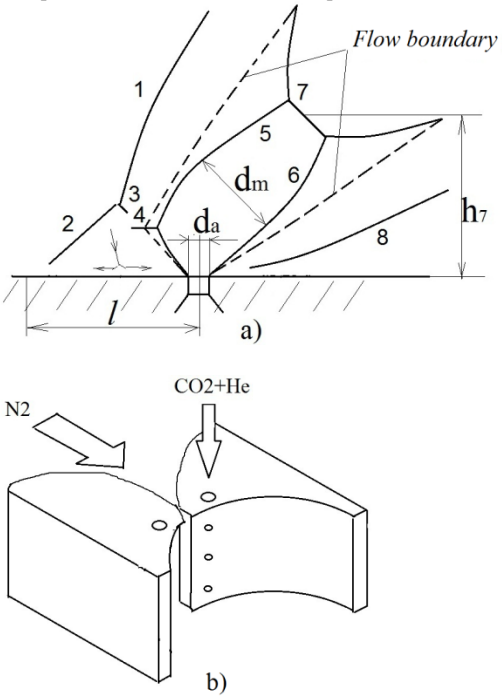


Fig.1. *Cross blowing of the reacting environments: a – scheme; b – constructive solution*
1 – main jump; 2 – skew jump; 3 – closer jump; 4 – jump in place of abrupt break; 5, 6 – barrel jump (inside flow); 7 – central jump (Mah's disk); 8 – jump, formed by the flow, gone around jet, inleaking on the wall; l – length of the separation zone; h_7 – distance to the Mah's disk center; d_m – diameter of the barrel jump; d_a – diameter of the injection hole.

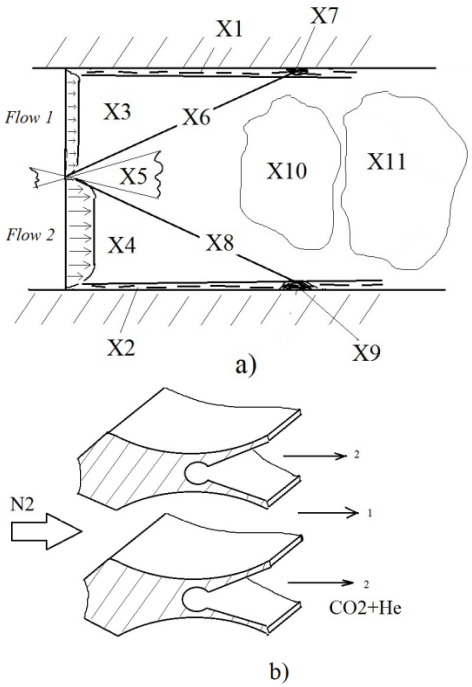


Fig. 2. *Longitudinal blowing of the reacting environments: a – scheme; b – constructive solution*
X1, X2 – turbulent boundary layers; X3,X4 – flows, entering the mixing chamber; X5 – boundary layer between the flows; X6, X8 – shock waves; X7, X9 – fields of the shock-wave interaction with turbulent boundary layers; X10 – field of the K-E turbulence model; X11 – field of A.N. Sekundov's model.

2. Hydrodynamic problem

As is well known, solution of the specified problems by means of purely grid methods is difficult. Indeed, the turbulent viscosity near the solid walls conveniently calculated using formulas of Prandtl and Spalding (1). Hereinafter A. Einstein's record of the field differential equations generally accepted:

1) index after the decimal point indicates the derivative on the corresponding coordinate.

2) the summation is performed according to the twice repeated index, although the sign of the sum is not specified.

(1) $$\nu_t = l^2\sqrt{(u_{1,2})^2 + (u_{2,1})^2}\,,$$

where l – the length of the mixing path

$$l = k \cdot L_{min},$$

k=0,41 – Karman constant, *Lmin* – the shortest distance to the nearest hard surface.

It is also not difficult to find ν_t in the initial sections of flows.

But in the area of the mixing flows we have to use either the K-E model (2):

$$\begin{gathered}\frac{\partial K}{\partial t}+u_iK_{,j}=\left(\frac{\nu}{\sigma_K}K_{,j}\right)_{,j}+S_K,\\ \frac{\partial E}{\partial t}+u_iE_{,j}=\left(\frac{\nu}{\sigma_E}E_{,j}\right)_{,j}+S_E,\\ S_K=\nu_mD-E,\ S_E=(C_1D-C_2E)\cdot E/K,\\ D=(u_{i,j}(u_{i,j}+u_{j,i}))^{1/2},\\ \nu\ =\nu_t+\nu_m,\\ \nu_t=\mathrm{C}_\mu K^2/E\ ,\end{gathered}\tag{2}$$

here ν_m, ν_t, ν - molecular, turbulent and full kinematic viscosity, K, E – kinetic energy of fluctuations and their dissipation rate, σ_K, σ_E, C_1, C_2, C_μ - semi-empirical constants,

either model of G.N. Abramovich and A.N. Sekundov is applied (3):

$$\begin{gathered}\frac{\partial\nu_t}{\partial t}+u_j\nu_{t,j}=\left((\nu_m+\varkappa\nu_t)\nu_{t,j}\right)_{,j}+\nu_t\cdot f\left(\frac{\nu_t}{8\nu_m}\right)\cdot D-\\ -\gamma\cdot L_{min}^{-2}(\nu_m+\beta\nu_t)\cdot\nu_t\\ f(z)=0{,}2\,\frac{z^2+1{,}47z+0{,}2}{z^2-1{,}47z+1}\ ,\end{gathered}\tag{3}$$

$\varkappa,\gamma,\beta$ - empirical constants.

The most difficult area is the interaction of shock waves with turbulent boundary layers. It is proposed to present such a motley picture of flows in one piece with the following neural network technology.

3. Neural network synthesis

Let us select the areas Xs; S = 1,2,…,N, each of which is characterized by its apparent specificity (shock wave, turbulence of a certain type, flow boundary layer, shock wave and boundary layer interaction zone and so on). Each of the mentioned fields Xs is fixed by the plurality of signal points $\overrightarrow{X_{sr}}; r=1,2,\dots,N_s$; N_s - the number of signal points in the field Xs. For each field Xs the potential of Braverman is introduced (4):

$$\varphi_S(\vec{x})=\sum_{r=1}^{Ns}\left\|\vec{x}-\vec{X}_{sr}\right\|^{-m_s}\ ,\tag{4}$$

m_s – positive value. $m_s>1$

If a random point $\vec{x}$ falls in the field Xs or approaches it, then the potential φ_S increases or takes the greatest value. We need to introduce some small constant protection from zero in the denominator in (4). Its neural function is introduced for each area Xs, for example, such (5):

$$g_S(\vec{x})=\frac{1-\exp(-\alpha_s\varphi_s(\vec{x}))}{1+\exp(-\alpha_s\varphi_s(\vec{x}))}\ ,\tag{5}$$

which refers to the number closest to the one in the field Xs and tends to zero outside it.

The transition rapidity of $g_S(\vec{x})$ from one to zero is regulated by constants m_s,α_s .

Now turbulent viscosity can be calculated throughout the study area as (6):

$$\nu_t=\sum_{S=1}^{N}g_S\ \ \cdot\nu_{tS}\ .\tag{6}$$

Neural interpolation will fill ν_t value for those areas for which there is currently no corresponding semi-empirical model. A similar technique can easily be extended to determine the position of the shock waves, satisfying the boundary conditions, etc.

Since the solutions are presented in an analytical form, then there is no need to split the grid steps in the field of sharp transitions. This is achieved by using the properties of neural functions g_S. Let the equations of gas dynamics system be presented (7):

$$F\left(\vec{x},U(\vec{x})\right)=0\ ,\tag{7}$$

F – some linear operators, $U(\vec{x})$ - the required fields, $\vec{x}$ - point of the real space field Ω, where the process is considered.

Equations (7) are joined by the boundary conditions (8):

$$f(U)|_\Gamma=f_\Gamma(x^/)\ ,\tag{8}$$

Γ – boundary of Ω, $x^/\in\Gamma$, f – boundary operators.

We seek a solution in the form of constructions (9):

$$U(\vec{x})=\Phi(\vec{x},A\ )=\sum_{s\in\Omega}\ \ {}^/g_s(\vec{x},\alpha_s,m_s)U_s(\vec{x},\beta\ ),\tag{9}$$

here U_s - special solutions for different subdomains X_s, $A\equiv(\alpha_s,m_s,\beta)$ - free constant, from the selection of which depends the approximation quality. U_s can be both analytical and grid approximations. Желательно при конструировании $\Phi(\vec{x},A\ )$ удовлетворить граничные условия. It is desirable to satisfy the boundary conditions in the design of $\Phi(\vec{x},A\ )$. This can be done by means of already mentioned neural functions g_s. In the region Ω the system of control nodes is selected. Each node represents a basic point, surrounded by a system of additional. It is possible to calculate the values of the fields U_s in each node at random, but specific parameters A and find all the partial derivatives by means of the difference method.

It should be noted that one should not equate such a calculation of derivatives with the traditional grid method. The control nodes may be spaced apart by a substantial distance, and auxiliary points are concentrated near the main central, that provides high accuracy and does not affect the stability of the calculations. The discrepancies *F* for equations are calculated in control nodes for any *A* (10):

$$F_i\left(\vec{x}_j,A\ \right)=F\ \ \left(\vec{x}_j,\Phi(\vec{x}_j,\mathrm{A})\ \right),i=1,2,\dots,N.\tag{10}$$

Of these the proximity measure *Q(A)* of the approximate solution to the exact is constructed. For example, in such form(11):

$$Q(A\ )=\sum_{i=1}^{\bar{N}}\ \ \sum_{j=1}^{M}\ \ \gamma_i\left|F(\vec{x}_j,\mathrm{A})\right|^{p_i}\ ,\tag{11}$$

where $p_i>0$; $\bar{N}$ – the number of discrepancies; γ_i – their weights; *M* – the number of control nodes, their number is considerably smaller than the number of nodes in the grid method.

Do other designs are possible to measure proximity. For optimal values *A* such values of *A** are taken, which deliver a minimum of the objective function *Q(A)*. As a tool of minimization the random search is used in the form, presented in [3]. An important advantage of random search in the ability to get out of local minimum and its insensitivity to non-smooth surface *Q(A)*.

Comment.

To determine the position of the shock waves and the zones of their interaction with turbulent boundary layers is convenient to take the continuity equation in the following form (12):

$$\dot{\rho}+(\rho u_i)_{,i}=\sigma\cdot\rho_{,ii}\ ,\tag{12}$$

here σ - constant, allowing to change the shock wave, increasing its thickness. The resulting field ρ is then approximated by the surface *Y(x)* with the appropriate neuro constructions. During the iterations parameter σ decreases, and the shock wave sharpens. With such an arrangement is possible to model the zone of the shock wave interaction with a turbulent boundary layer. With

neuro approximation the boundary conditions are satisfied automatically. If this fails, then the measure of closeness Q is added by the penalty function.

4. Conclusion

The proposed method of solution of gas- and hydrodynamic problems, the foundation of which was laid in the works of Academician G.I. Petrov and his school, can be extended to a wide range of applications, where traditional grid approaches face major difficulties. Development of the system, consisting of neural network and dynamic model looks promising. Combination of dynamic model and neural network will allow to study physical processes more fully and quickly, to determine the unknown hidden parameters and initial conditions. These capabilities allow to apply the proposed method in many application areas.

5. References

[1] Golovko V.A. Neural networks: training, organization and use of, M., Publishing House of the magazine "Radiotehnica", 2001, 256 p.

[2] Solouhin R.I., Fomin N.A. Gas-dynamic lasers mixing, Publishing House «Nauka I tehnica», Minsk, 1984, 148 p.

[3] Yasinskiy I.F, Yasinskiy F.N. Improved random search// Vestnik IGEU-2004.-№3.-P.47-48.

[4] Kontorovic L.V., Krilov V.I. Approximate methods of higher analysis, State Publishing House of the phys.-math. Lit-re, M.:1962, 708 p.

ENERGY TECHNOLOGY ACTIVATION COMPONENTS FUNCTIONAL MATERIALS BASED ON POLYMERIC MATRIX

ЭНЕРГЕТИЧЕСКИЕ ТЕХНОЛОГИИ АКТИВИЗАЦИИ КОМПОНЕНТОВ ФУНКЦИОНАЛЬНЫХ МАТЕРИАЛОВ НА ОСНОВЕ ПОЛИМЕРНЫХ МАТРИЦ

Sarokin V.[1], Doc. cand. eng. Auchynnikau Y.[2], Doc. cand. eng. Avdeychik S.[3], Prof. dr. eng. Struk V.[4],
Faculty of Innovative Technologies Engineering [1,2,4] – University Grodno, Belarus, E-mail: sorvg@grsu.by
Ltd. "Molder" [3] - Grodno, Belarus, E-mail: info@molder.by

Abstract: *Investigated the mechanisms of interfacial interactions in composite materials based on thermoplastic matrices modified with dispersed particles of silicon and carbon-containing compounds with high energy activity. It was found that the laser treatment of particulate and fibrous particles occurs comprehensive modification of the surface layer, which consists in shaping the development of the morphology of the surface layer and increase its energy. For the modification of thermoplastic matrix including high-viscosity (polyamides, PTFE) prospectively the use of dispersed fragments of carbon fiber (CF) fraction 50-150 microns, subjected to the effects of a short pulse laser, having developed the morphology of the surface layer and the presence of defects through thermal degradation. When using this modifier in an amount of 5-30 wt.% for filling PA6, PA66, PTFE provides increased of parameters deformation and strength characteristics due to the increased mechanical component adhesive interaction at the interface of "matrix-filler". An additional effect is realized in the processing of the surface layer of CF fluoride compounds oligomeric or polymer-oligomeric structure. The modified fluorinated hydrocarbon components fragments CF when laser pulse processing are exposed to the active low molecular weight products ablation, so that the surface layers are formed with a high affinity to the matrix polytetrafluoroethylene. The complex method of modifying CF is effective for highly filled fluoro composites containing 25-35 wt.% of carbon fillers due to the decrease in the probability of formation of cluster structures of the filler particles. Dispersed particles silicate (clay, tripoli, talc) and carbon (graphite, carbon black, shungite) when exposed to laser radiation susceptible to degradation with the formation of nanoscale fragments in a moving layer, thus increasing their activity in the processes of the interfacial interaction in the formation of composites based on oligomeric and polymeric matrices.*

KEYWORDS*: COMPOSITES, MODIFIERS , INTERPHASE INTERACTION, MORPHOLOGY, ENERGY STATES*

1. Introduction

Among the promising areas of materials science is the creation of composites based on thermoplastic matrices modified with nano-sized components of different composition, structure and habit [1-4]. The mechanism of action of modifying nanoparticles is to implement a multi-level approach, which is possible to control the processes of structural organization at the molecular, intermolecular, supramolecular and interfacial levels. Nano sized modifier, depending on their size and energy state (nano particles, nano cluster, micro particle nano dimensional topography) may form intramolecular or intermolecular physical bonds in place of the functional groups, to promote the orientation of macromolecules or their segments to form a quasi-crystalline structures, be the centers of formation of crystalline structures spherulitic type, form interfacial boundary layers increased strength.

To realize the nano particle dispersion state of the effect modifier should be in the nano size range or have developed relief of the surface layer containing nano components of different habit - whisker, plate, spherical [1-4].

An analysis of the literature and our model representations [1, 2] show preference plate nano habit modifiers or fragments thereof on micro particles, as in this case it achieved a significant effect of improving the parameters of strength and tribological characteristics when doping content modifier is (0.1-1.0) wt.%. At the same time, there are different mechanisms of formation of this habit of the particles.

The purpose of this study was to use the features of the morphology of the dispersed particles subjected to different types of energy impact.

2. Research methods

For the research were chosen components used for the production of composite materials based on polymeric and oligomeric matrix – particles carbon containing (graphite, carbon, UFD UFDG, carbon fiber), silicon-containing (clay, talc, mica, flint) and combined (shungite) products. In separate experiments the particles dispersed lamellar thermo polymers - a polyamide 6 (PA6), polytetrafluoroethylene (PTFE), ultra thermodynamic synthesis products (UPTFE).

Activation particles modifier carried the energy, thermal, laser, mechanochemical effect. The assessment was carried out activities in the parameter values of the thermally stimulated current (TSC) in the temperature range (293-523) K.

3. Results and discussion

The activity of the dispersed particles of fillers and modifiers in the process of interaction of the matrix determines the mechanisms and kinetics of formation of the structure of the boundary layer, which is correlated with the parameters of strength, tribological, thermal, adhesive and other service characteristics of composite materials based on high molecular weight matrix (Figure 1).

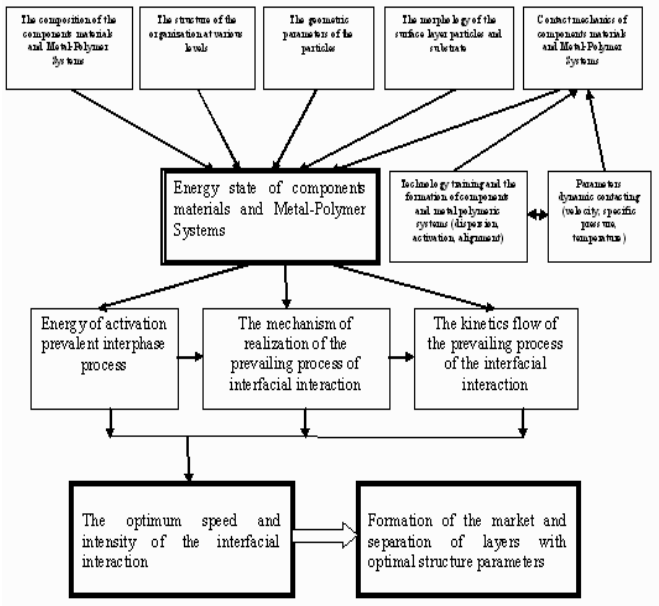


Fig. 1 *The energy factor of materials science and technology of composite materials and Metal-Polymer Systems*

The literature and our research suggests that the optimal modifying action the particles, which realized the effect of nano state, due to the size range or the particle itself or the individual components of its surface layer [1]. Established the basic factors determining the state of nano dispersed particles of condensed matter that allow the selection of the method of its implementation for the particular combination of the components and functionality of the composite (Figure 2).

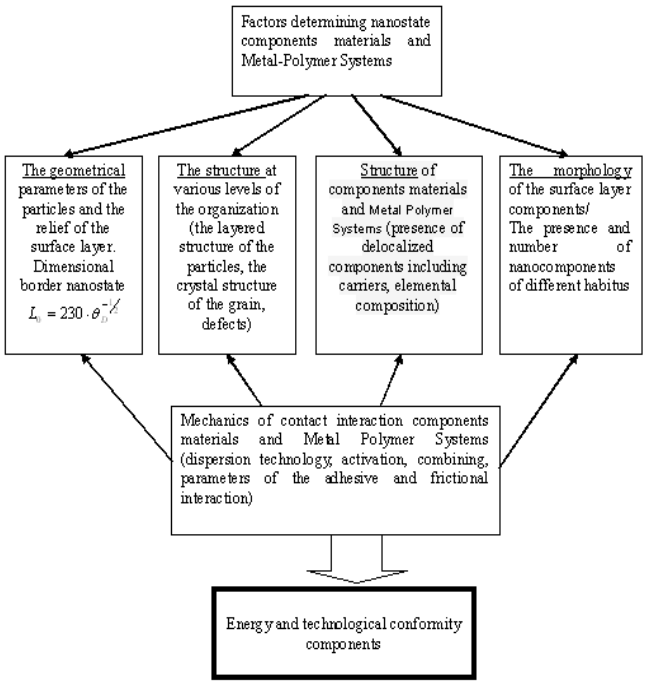


Fig. 2 *Factors nanostate components material systems*

To make informed choices activation technology modifiers dispersed particles of different composition, crystal-chemical structure and nature should be used L_o parameter which determines the maximum size at which manifest the characteristics of nanostate. Parameter L_o is determined from the analytical expression $L_0 = 230 \cdot \theta_D^{-1/2}$, where θ_D – temperature Debye.

The experimental results indicate that the provision of high-activity modifying particles may be in the micron size range with advanced morphology of the surface layer formed nanoscale components whisker, plate and spherical habit. To form such morphology a surface layer of the most promising effect on the dispersed particles of energy flows that cause the process of thermal degradation, pyrolysis, degidroksilatsii, dispersing with formation nanocomponents.

Analysis of the morphology of the surface layer of particles of different composition and structure subjected to thermal, laser and mechanochemical action, indicates the presence of the general laws of manifestation nanostate (Figure 3).

For the carbonaceous particles detonation synthesis products UFDG and colloidal graphite, obtained by flotation, increased sophistication of the surface layer is observed with the formation of nanoscale components. The effect is most pronounced when the modification of the particulate laser semifinished (Figure 3, c, f). Similar processes of dispersion of the surface layer is characterized for particle silicates (mica, clay, talc), and shungite. The particular morphology characteristic of hydrocarbon fragments, in which along with the development surface, observed through the formation of defects (cracks) by laser radiation. The close nature of the morphology of the surface layer characteristic of dispersed particles subjected to mechanical stress during acceleration (2÷20) g.

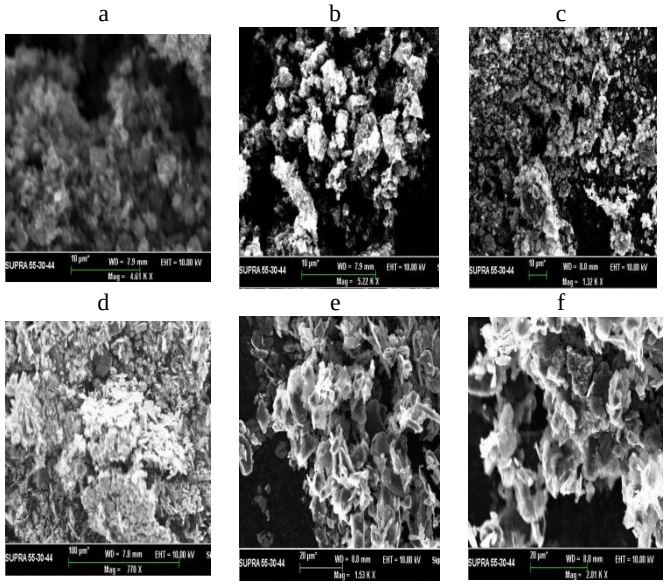


Fig. 3 *A typical morphology of the dispersed particles of the charge detonation synthesis UFDG (a, b, c) and colloidal graphite C-1 (d, e, f) of the original (a, d), thermally treated(b, e) and treated with laser light (c, f). These SEM*

4. Conclusions

Analysis of the energy state of the dispersed particles after different types of activation indicates an increase in the intensity of thermally stimulated currents temperature range (303-523) K. Comparison of the calculated parameter data L_o and results TST – analysis suggests the manifestation of the dispersed particles in the micron range, subjected to various types of activation, the characteristic features nanostate. With the introduction of such particles into the polymer matrix – polyolefins (HDPE, PP), polyamides (PA6, PA6.6), polytetrafluoroethylene (PTFE) in an amount of (0.01 ÷ 1.0) wt.% is observed the effect of increasing strength and wear parameters, indicating that manifestation technically significant effect modification as a result of increased activity.

5. References

1. **Avdeychik, S**. Introduction to the physics of nanocomposite engineering materials /S. Avdeychik, etc.: – Grodno: GGAU, 2009. – 439 p.
2. **Avdeychik, S.** Silicate polymer engineering materials: Physics and chemistry, technology, application / Avdeychik S., Liopo V., Struk V. [and etc.] – Minsk: Technology, 2007. – 431 p.
3. **Gusev, A.** Nanomaterials, nanostructures, nanotechnology – M.:, 2005. – 416 p.
4. **Ajayan, P., Schadler, L., Braun, A.** Nanocomposite science and technology. - Willey - YCY Gmbh JCo Kgal, 2004 - 230 p.